Sensitivity Enhancement and RF Characterization of Rydberg-Atom Microwave Receivers

by

Georgia Sandidge

B.S., Rutgers University, 2021

M.S., University of Colorado at Boulder, 2023

A thesis submitted to the

Faculty of the Graduate School of the

University of Colorado in partial fulfillment

of the requirements for the degree of

Doctor of Philosophy

Department of Electrical, Computer, and Energy Engineering

2026

Committee Members:

Zoya Popović, Chair

Prof. Dejan Filipovic

Prof. Cody Scarborough

Prof. Gabriel Santamaria-Botello

Prof. Dana Anderson

Dr. Suresh Subramanian

Sandidge, Georgia (Ph.D., Electrical Engineering)

Sensitivity Enhancement and RF Characterization of Rydberg-Atom Microwave Receivers

Thesis directed by Prof. Zoya Popović

A Rydberg-atom vapor consists of atoms held at low pressure and excited by an optical field to a nearly ionized state called the Rydberg state. A vacuum cell containing such alkali atoms, typically Rb or Cs, can function as a sensor of radio-frequency (RF) fields through Autler–Townes splitting of a resonant EIT transmission peak. Such sensors have been demonstrated for measuring magnitude in an electrometer configuration, or magnitude and phase in a receiver configuration. These sensors can operate across a range of frequencies with a narrow-band response. Because their response is rooted in atomic structure, they also offer a fundamentally calibrated approach to RF sensing. This makes them attractive for applications requiring traceability, compact sensing elements, or operation in frequency regimes that are challenging for conventional electronics.

The sensitivity of such receivers, though promising, has not yet achieved performance comparable to that of standard RF heterodyne receivers. The goal of this thesis is to compare and demonstrate methods for increasing the sensitivity of Rydberg-atom receivers through resonant RF structures. Specifically, both fixed and tunable sensitivity enhancement over a free-space receiver are demonstrated at 10.22 GHz, reaching a sensitivity of 1.5 $\mu V/m/\sqrt{\text{Hz}}$, corresponding to a noise-equivalent temperature (NET) of 23,000 K. Further, a mm-wave electrometer is demonstrated at 61 GHz and characterized in terms of its dynamic range, agreement with theoretical values, and performance with respect to polarization. The same receiver, with a 61 GHz wave in addition to two lasers (at 780 and 480 nm), is used to create a resonant atomic level at 2 GHz for a low-frequency Rydberg-atom receiver. This receiver was tested for its sensitivity and selectivity in the presence of an interferer. This thesis contributes new knowledge in Rydberg-atom microwave sensors, particularly in the area of RF characterization and the design of RF enhancement circuits.

Dedication

To my dad, for teaching me that creativity and hard work can take you anywhere.

Acknowledgements

First and foremost, I would like to express my deepest gratitude to my advisor, Zoya Popovic, for her unwavering dedication, guidance, and mentorship over the past five years. Her encouragement and steadfast support have profoundly shaped both my development as a researcher and my growth as a person. I truly would not have accomplished what I have without her unwavering belief in me.

To my family, Jim, Shari, Lily, and Kate, thank you for being my foundation. Your steady encouragement and unconditional belief in me carried me through moments of doubt and exhaustion. Knowing that you were always cheering me on allowed me to persevere through even the toughest obstacles.

To my husband, Omaid. You have been my constant, my comfort, and my greatest source of strength. Your love, patience, and endless support made this achievement possible. I appreciate all that you have done in support of my journey.

Lastly, a sincere thank you to the friends and fellow graduate students who have shared this path with me. Thank you for the laughter, the late nights, and the lunch runs. You made the difficult days manageable and the best days unforgettable. You are among the strongest, wisest, and most intelligent people I know, and I am grateful to have journeyed alongside you all these years. I am incredibly proud to call you my friends, and I know the bonds we built during this time will endure far beyond graduate school.

This journey has challenged and shaped me in ways I never anticipated, and I am deeply thankful for everyone who supported me through its many highs and lows. As I step into the next chapter, I do so with gratitude and confidence, knowing I am supported by some of the most incredible people I have ever had the privilege of knowing.

Contents

Chapter

1 Introduction **1**

1.1 Background . . . 3

1.2 Rydberg Atoms . . . 6

1.3 EIT, AC Stark Shifting, and AT Splitting . . . 8

1.4 Previous Rydberg Demonstrations . . . 12

1.5 Thesis Organization . . . 14

2 Figures of Merit for Receivers **17**

2.1 Sensitivity . . . 18

2.2 Comparing to Conventional Receivers . . . 20

2.2.1 Free-Space Method . . . 20

2.2.2 Port-Coupled Method . . . 23

2.3 Rydberg Sensitivity Examples . . . 24

2.4 Size, Power Consumption, and Bandwidth . . . 26

3 X-band and Ku-band Sensitivity Enhancement **29**

3.1 Enhancement Factor (F) . . . 29

3.2 Other Enhancement Methods . . . 30

3.3 Waveguide Resonator . . . 32

3.4 15 GHz Design - RF Characterization . . . 35

3.5 10.22 GHz - RF Characterization . . . 41
3.6 10.22 GHz - Optical Measurements . . . 49

4 Frequency-Tunable X-band Sensitivity-Enhanced Rydberg Receiver 55

4.1 Resonator RF Characterization . . . 55
4.2 Rydberg Receiver Sensitivity Enhancement Measurements . . . 61
4.2.1 Free-Space Recevier at 10.22 GHz . . . 63
4.2.2 Enhanced Receiver at 10.22 GHz . . . 65
4.2.3 Free Space and Enhanced Receiver at 10.77 GHz . . . 67
4.3 Additional Effects on Sensitivity and Resolution . . . 67
4.4 Conclusions . . . 70

5 V-band and S-band Rydberg-atom Sensor Measurements 73

5.1 V-band Set-Up and Measurements . . . 74
5.2 Low Frequency Comparison to Conventional Receivers . . . 79
5.3 S-band Optical Set-Up . . . 82
5.4 Isolation from Interferors - Electrometer . . . 86
5.5 Isolation from Interferors - Receiver . . . 87
5.6 Polarization Impact . . . 92

6 Conclusions and Future Work 94

6.0.1 Thesis Summary . . . 94
6.1 Future Work . . . 94
6.1.1 GaAs Microwave LO for Heterodyne Rydberg-Atom Receiver . . . 94
6.1.2 High Frequency Enhancement . . . 102
6.1.3 Thesis ContributionsConclusions . . . 105

Bibliography **106**

Appendix

A Appendix A **115**

A.0.1 A Study on Vapor Cell Heating 115

Tables

Table

1.1 Noise-equivalent field (NEF) measurements for Rydberg-atom E-field sensors 14

2.1 On-resonant Rydberg receiver sensitivities 25

2.2 Off-resonant Rydberg receiver sensitivities 25

4.1 Summary of on-resonant experimental results. 71

4.2 Comparison of Rydberg-atom receiver enhancement in the microwave domain. 71

5.1 Comparison of Theoretical and Measurement E-field 79

Figures

Figure

1.1 (a) A Rydberg-atom electrometer block diagram, compared to (b) a standard RF/microwave antenna coupled to a detector. (c) A Rydberg-atom receiver block diagram, compared to (d) a standard RF/microwave receiver. 2

1.2 Example antennas: (a) Antenna size versus frequency, from 100 MHz to 1 THz. This assumes that the Rydberg vapor cell is 2 cm long and $\epsilon_{eff} = 2.2$ for a microstrip patch antenna. For comparison, a (b) quarter-wave monopole array [85] that is a minimum of 19 cm tall, (c) half-wave dipole [116] that is 24 cm long, and (d) microstrip patch that is 1.4 cm on the longest side [55]. 4

1.3 State-of-the-art cryogenic amplifiers with minimum noise temperature measurements, as well as predicted bounds [80]. At high frequencies, even at smaller gate lengths and cryogenic temperatures, standard low noise amplifiers are limited in their noise temperature and therefore sensitivity [42] 5

1.4 (a) A sample atomic energy transition scheme in rubidium, showing successive energy levels and the method by which an atom could be excited to each. (b) Autler-Townes (AT) splitting and AC stark shifting. Both traces show the output from the photodetector in the presence of an electric field (solid dark gray trace) versus the Rydberg-state without external field (unfilled light gray trace). 7

1.5 (a) A two-photon excitation scheme, as well as (b) a three-photon Rydberg scheme, with the probe, coupling, and dressing lasers. Additional electronics (not pictured) are necessary to interrogate laser wavelength and lock the lasers to the necessary transition. 10

1.6 (a) A two-photon Rydberg-atom receiver in potassium, using 480 nm and 456 nm lasers [40]. (b) A three-photon receiver in cesium using 636 nm, 895 nm and 2235 nm lasers [83]. (c) A two-photon receiver in rubidium, using 480 nm and 780 nm lasers [104]. 13

2.1 Theoretical limits set by thermal and quantum background noise, plotted alongside the sensitivity of several Rydberg receivers reported in the literature. The data point that intersects the thermal NEF line employs a unique sampling method that is not constrained by typical Rydberg measurement limits. 19

2.2 (a) Sketch of Rydberg atom-based microwave receiver. In the free-space treatment, we do not assume anything about it's performance or set-up. Compared to a conventional receiver topology (b), with an assumption that the LNA has sufficient gain and dominates receiver performance, with a given noise temperature, and a receiving antenna with a particular gain. 22

2.3 (a) Rydberg atom-based microwave receiver. In the port-coupled treatment, we assume the same antenna is connected to (a) as in the conventional case (b). This forumlation is useful for quantifying sensitivity enhancement. 23

2.4 Sensitivity in units μV/m/$\sqrt{\text{Hz}}$ for a variety of Rydberg electrometers and receivers. Both on-resonant and off-resonant configurations trend towards higher sensitivities with time. . . 24

2.5 The sensitivity (expressed as gain over noise equivalent temperature) versus frequency for a variety of Rydberg receivers, in both off and on-resonant configurations. This sensitivity is expressed as a G/T value. In the figure, the red band represents the sensitivity of a sample of conventional, low-noise amplifier-based receivers, assuming each one is connected to dipole with gain 3/2. [9] The NET of the conventional receivers is found from the the LNA, the first of which, in a cascaded system, would dominate the noise temperature. 26

2.6 Rydberg receiver optical components mounted to an optical table, which encompasses an area approximately 75 by 125 cm. This photo does not show the associated electronics for controlling the laser heads, which are on a rack above the table, and also have a footprint of approximately 75 by 125 cm. 27

3.1 Other microwave enhancement methods, including a split ring resonator (a) from [45], close-proximity co-planar waveguide line [74] (b), and parallel plate resonator [3]. 30

3.2 (a) A regular $\lambda/2$ length waveguide. The waveguide is fed through an aperture on one side of the waveguide (y-axis), while there are two optical windows on the x-axis to accommodate the probe and coupling lasers. The electric field is pointed along the z-axis. (b) An improved resonant cavity design, where a smaller, electrically shorter but physically longer section of waveguide is placed between two electrically longer larger sections. 32

3.3 Noise temperature versus frequency for a sampling in low-noise amplifiers, manufactured in different technologies. LNA sensitivity tends to decrease with increasing sensitivity, as shown by the plot. [9]. Furthermore, we can see that the sensitivity of a Rydberg-atom receiver can be enhanced through the use of a half-wavelength long resonator, from the formulation shown in [94]. 34

3.4 (a) 3D view of the field-enhancement 15.096-GHz cavity fed by a WR62 rectangular waveguide. The total volume of the resonator is approximately $20 \times 30 \times 40$ mm. (b) Photograph of one half of the split-block machined structure. In addition to the waveguide sections A and B, additional apertures accommodate the excitation laser beams (shown in blue and red arrows), the filling tube of the vapor cell, and a tuning screw. (c) Photograph of the unfilled fused silica vapor cell. 35

3.5 Dependence of reflection coefficient at the WR62 waveguide feed on tuning screw displacement from -0.271 mm to $+0.229$ mm relative to the position when it is flush with the waveguide wall. The full tuning range is 216 MHz without significant degradation in Q factor. 36

3.6 The magnitude of the electric field in the resonating cavity. Inside the vapor cell, the maximum E-field is $1.18 \cdot 10^5$ V/m for a 1 W input power at the waveguide feed. The electric field is linearly polarized. 37

3.7 Simulated reflection coefficient magnitude and phase vs. frequency for three lengths of a 3-mm tall aperture: nominal length of 5.9 mm $\pm 200\ \mu$m. The mode changes from undercoupled to overcoupled as the aperture increases. 37

3.8 (Top) Magnitude and phase of measured reflection coefficient showing a resonance at 15.5016 GHz. (Bottom) Inset of the resonance shown in the top figure, and theoretical fit (dashed) curves. 38

3.9 Estimated noise temperature of manufactured cavity as a function of the coupling strength, for different NEF_0 values. 40

3.10 The geometry of our resonant cavity. This resonator was machined in two parts, and is therefore composed of two split blocks. Designed for a 10.22 GHz transition, it is fed with a WR90 waveguide. The coupling between this resonator and the waveguide can be modified using a sliding feed, which changes the effective aperture size. The vapor cell sits inside the resonant cavity, where it can be tuned using a frequency tuning piston. 41

3.11 The fields along the z-direction of the resonator, with the same polarization as the linearly polarized laser (y-direction). There is a high degree of uniformity in this waveguide compared to a standard $\lambda/2$ waveguide, varying between $5.8 \times 10^4\,\mathrm{V/m}$ and $6.75 \times 10^4\,\mathrm{V/m}$ with an average value of $6.44 \times 10^4\,\mathrm{V/m}$ for a 1 W input power. 42

3.12 Comparison of the measured and simulated resonator properties. In order to observe resonance, heaters are applied to the cavity with the cell inserted and VNA measurements are performed for several hours while the heat was applied. The measured resonance is at 10.2246 GHz, or within 0.045% of the target frequency. 44

3.13 The effect of heating the resonator over a 30-hour time period. There was some asymmetry in heating the two thermistors as a result of the limits of the control panels. For the time interval of 400 to 1300 minutes, data was not recorded as the experiment was left running overnight. Ultimately, the Q-factor improved from 0 (no resonance) to ≈ 600 over the full time period. 46

3.14 The measured frequency tuning for three configurations of the resonator: with one tuning rod T1, tuning rod T2, and the frequency tuning piston. All frequencies between the all-removed and all-inserted configurations are accessible. 47

3.15 Measurements of resonator reflection coefficient magnitude and phase based on three sliding feed positions, and the frequency tuners at maximal insertion. The first measurement corresponds to the apertures completely aligned, and therefore maximal transmission. The second and third plots are with the feed slid one and two millimeters, respectively. 48

3.16 The experimental set-up used for measuring the sensitivity of the Rydberg receiver with cavity enhancement. From this topology, the AT splitting is measured, and then used to calculate the minimum detectable field at the input of the resonator. The coupler is a 20 dB coupler. 49

3.17 Intermediate frequency power as a function of signal power at the plane of the cavity port. Measurements are recorded with 1 Hz resolution bandwidth on the spectrum analyzer. The two values should be directly correlated, as maintained in this measurement for a majority of the data collection interval. 51

3.18 Intra-cavity electric field measured via AT splitting as a function of the square root of the power at the input port of the resonator. 52

3.19 The realizable NEF (and equivalent NET) for a given NEF_0 and resonant cavity coupling coefficient. At higher NEF_0 thresholds, a resonant cavity provides the most enhacement when critically coupled. With a lower sensitivity free-space noise equivalent field, an overcoupled cavity gives the best sensitivity. 53

4.1 (a) A full render in Ansys HFSS of the resonator. The center section contains the vapor cell, while the sliding waveguide components on either side can be displaced to tune the resonant frequency. (b) A cut-away of the resonator, so that the interior can be seen. (c) The resonant cavity in aluminum after CNC machining. For fabrication purposes, it is split into seven pieces and assembled with screws. 56

4.2 (a) Simulated magnitude of the z-directed electric field vector component at 10.22 GHz, plotted across the interaction length x of the vapor cell. (b) the magnitude of the electric field in the z-direction on a cross-section along the x direction. The values are normalized to a 1 W incident power at the waveguide port. 57

4.3 Measured reflection coefficient as a function of plunger displacement, which modifies the cavity length from 8 to 2 mm. The desired 10.22 GHz transition occurs when the cavity is $d = 7$ mm long (plunger displaced 1 mm.) 59

4.4 Resonator reflection coefficient magnitude and phase, indicating tuning to all three coupling regimes: over-, under-, and critically coupled, which are (a), (b), and (c) respectively. 59

4.5 Simulated and measured resonant frequency for the $59D_{5/2}$ (10.22 GHz) Rydberg transition. Both values were calculated using a plunger depression of 1 mm and critical coupling. The small artifact measured on the blue trace is a result of the placement of the vapor cell within the resonator. 60

4.6 (a) The optical scheme used for the Rydberg receiver. Off table, the photodetector connects to a spectrum analyzer for readout of the splitting response. Additionally, the laser head current, temperature, and scan amplitude are controlled by external modules. (b) The test set-up, as arranged in the lab. In experiment, a singular horn delivers the RF and LO fields, to simplify the number of devices used. 62

4.7 The output power (received at the spectrum analyzer) as a function of the electric field. Plot (a) is for the small Precision Glassblowing vapor cell while plot (b) is for the larger ThorLabs vapor cell. The electric field is gradually decreased to find the noise floor of the system, such that it can be fit with a line to determine the minimum field that can be resolved by the receiver. 64

4.8 (a) The port-coupled resonator as positioned in the Rydberg receiver. Foam is placed on the metallic optical table to minimize environmental noise effects. (b) The power received at the spectrum analyzer as a function of the electric field inside the vapor cell for the 10.22 GHz measurement configuration. 66

4.9 (a) Horn antenna and vapor cell. The "center" sample occurs in the middle of the central cylinder on the cell, line B. The "front" occurs on the side of the glass closest to the horn, line A. The "back" occurs on the side of the glass farthest from the horn, line C. The photo is a representation of the set-up and does not indicate the actual distance between horn and cell. (b)-(d) 10.8 GHz free-space AT splitting at different locations in the Thorlabs cell for equal incident field. 68

4.10 Field measured with AC Stark shifts. All lines are spaced by 59 MHz highlighting the shared periodicity, with unique offset for each measurement and above and below 10.3 GHz. Inset to (b), $|S11|$ measurement of the Cavity with the cell held in place with packing peanuts. There are two resonance troughs, -48.1 dB at 10.36 GHz and -40.3 dB at 10.31 GHz. 69

5.1 The Rydberg electrometer setup, consisting of a vapor cell, two lasers, and a photodetector (out of view). The incident millimeter-wave field is radiated from a V-band standard gain horn antenna for the experiments discussed in this paper. 74

5.2 (a) Measured AT splitting for a range of incident millimeter-wave electric field magnitudes, obtained by varying the signal generator power. The y-axis is in arbitrary units of transmitted probe laser power. The value of ρ for this energy transition is $628\alpha e$ where α is the Bohr radius and e is the electron charge. (b) The magnitude of AT splitting versus signal generator output power from 0.01 to 0.2 W. We expect the response of the system to be linear. Deviations from this trend are due to peak broadening at high powers and to limitations from the EIT linewidth at lower power levels. 75

5.3 AT splitting versus degree of antenna polarization. At 0 degrees, the electric field from the horn and the lasers are fully co-polarized in the vertical direction. At 90 degrees, the electric field is entirely in the horizontal direction. Though the atoms are still able to resolve the rotated field, there is some degradation in the resolution associated with the polarization mismatch. 78

5.4 The Chu limit as a function of antenna size. For the conventional limit (black line), we assume a VSWR of 2, and a maximum η of 1. For the Rydberg-atom receivers, we assume a vapor cell that is 1 cm long, in a room temperature (290 K) environment. [99] 81

5.5 The excitation scheme for a high frequency to low frequency RF transition. This layout assumes no local oscillator. 82

5.6 The low-frequency Rydberg-atom receiver, mounted to an optical table. The blue and red arrows show the path of the probe and coupling lasers, counterpropogating. The red laser is ultimately read out on a photodetector, indicated by the red arrow. The electric field from the source (gray horn) and the interferer (black horn) are indicated by yellow arrows. A V-band horn antenna (not shown) provides the intermediate microwave transition that couples the initial Rydberg state to the splitting state. 83

5.7 AT splitting for the low-frequency energy transition as a function of the power from the 2.28 GHz source. This progression of powers shows the low frequency energy level splitting from an AT splitting peak generated by the V-band source. Then, with more power, this becomes the dominant peak. The progression in power is (a) at -2 dBm or 0.69 V/m, (b) at 3 dBm or 1.22 V/m, (c) at 12 dBm or 3.46 V/m, and (d) at 17 dBm or 6.16 V/m. 84

5.8 Electrometer measurement of the low-frequency receiver, with (left) and without (right) the presence of an interferor at 8.70 V/m, 100 kHz offset from the low-frequency tone of choice. 87

5.9 Sensitivity of receiver in free space versus with an interfering signal 100 kHz from the main signal, at a power of 20 dBm, approximately co-located with the source. 87

5.10 Degradation in receiver sensitivity as a function of interferer signal power. 89

5.11 Sensitivity of the receiver in the presence of an interfering signal transmitted at 20 dBm while the interferer frequency is swept relative to the desired field. Clear degradation in sensitivity as a function of interferer frequency is observed. 90

5.12 Sensitivity of the receiver in the presence of an interfering signal transmitted at 20 dBm while the interferer frequency is swept relative to the desired field. Clear degradation in sensitivity as a function of interferer frequency is observed. 92

6.1 A cross-section of the resonant cavity holding the vapor cell full of Rubidium atoms. The tail of the fused silica vapor cell is much longer than the width of the waveguide cavity, so an aperture is cut within the cavity to accommodate the tail. The local oscillator (shown in orange) couples into the waveguide by capacitively loading the glass on a side wall of the vapor cell. 95

6.2 A Rydberg receiver, composed of a Rubidium vapor cell embedded in a resonant cavity, excited with two lasers. The oscillator is placed on the exterior of the resonant cavity, and coupled to the vapor cell using a probe. This paper focuses on the design of the LO in GaAs, specifically for a Rubidium receiver using metallic waveguide cavity enhancement for the 11.369 and 15.095 GHz transitions. 96

6.3 (a) MMIC layout using Cadence AWR Microwave Office that shows the two oscillators. The die size is 3.29 mm $\times$ 2 mm. The top circuit is the 11 GHz oscillator, indicated by the longer meandered line on the gate side of the transistor, while the bottom circuit is the 15 GHz oscillator. Both are single-port RF devices, measured using GSG pads on the drain side (left) of the circuit. (b) Photograph of the MMIC with two oscillators having layouts shown above. The RF output (resonant frequency) is measured on the three-pronged GSG probe on the left, while the DC bias is supplied by the DC probes on the left and right of the chip. . 97

6.4 The simulated harmonic content and phase noise for the 11 GHz oscillator with bias conditions $V_{DD} = 4\,\text{V}$ and $V_{GG} = 1\,\text{V}$. The first harmonic has a power of 15.79 dBm, the second harmonic of 7.84 dBm, and third harmonic power of -2.45 dBm. The simulated phase noise is $-104.8\,\text{dBc/Hz}$. 99

6.5 (a) Measured output power as a function of frequency for the 11 GHz oscillator, used to determine the phase noise, which was $-109\,\text{dBc/Hz}$ at 1 MHz offset. This was measured at 11.0949 GHz with bias $V_{DD} = 3.5\,\text{V}$ and $V_{GG} = 0.5\,\text{V}$. (b) Output power for the 15 GHz oscillator, with a phase noise of $-99\,\text{dBc/Hz}$ at 1 MHz offset. This was measured at 14.484 GHz with bias $V_{DD} = 5\,\text{V}$ and $V_{GG} = 0.5\,\text{V}$. 100

6.6 A plot of the oscillation frequency versus change in voltage at 11 GHz. Each point on the plot corresponds to a discrete measurement of a changing drain (blue) or gate (red) voltage. When the gate voltage was swept, the drain was fixed to 4 V. When the drain is swept, the gate is set to 0.2 V. 101

6.7 A plot of the oscillation frequency versus change in voltage at 15 GHz. When the gate voltage is swept, the drain is fixed to 4 V. When the drain is swept, the gate is set to 0.9 V. . . 101

6.8 A Gaussian beam set-up, constructed from two concave parabolic mirrors. The resonator is fed through the center of one mirror, resulting in a beam of minimum beamwidth of ω_0 and a Rayleigh range of z_R. The vapor cell is placed in the center and determines the necessary size of the beam. 102

A.1 Geometry of cross-section of the cavity with the vapor cell inserted (left) and photographs of the cavity and glass vapour cell (right). 115

A.2 Simulated co-polarized component of the electric field vector (out of the page) in the cavity (top), including the glass vapor cell filled with vacuum in the simulations. These full-wave simulations are performed with *Ansys HFSS*. The plot shows the normalized electric field vector component along the vapor cell major axis inserted in the cavity. 117

A.3 Measured shift in resonant frequency as a function of baking time starting with a cell where the Rubidium condensed on the cell glass wall. 118

A.4 Measured and simulated cavity resonance without the vapor cell, showing a 1.13% difference between the two. 118

Chapter 1

Introduction

Quantum radio-frequency sensors, particularly those that use highly excited atoms known as Rydberg atoms, first emerged in 1980 with their implementation in a 100 GHz detector [35]. Since then, Rydberg atom-based quantum sensing of radio-frequency fields from frequencies as low as 770 Hz [53] and as high as 0.55 THz [30], has been applied to receivers [28], power sensors [49], spectrum analyzers [75], pulsed radar [13], and remote sensing [5]. Rydberg atom receivers offer several advantages. They can detect fields over a very wide range of frequencies, because the sensing frequency corresponds directly to one of the numerous atomic energy level transitions in the atom. At the particular carrier frequency, Rydberg receivers exhibit high frequency selectivity due to the narrowband nature of each transition. Importantly for metrology, these transitions correspond to well-known atomic energy levels and are therefore inherently self-calibrating. Measurements made with Rydberg receivers are theoretically quantum limited, with the dominant noise source typically being laser photon shot noise associated with excitation to the Rydberg state. Compared to standard electronic sensors implemented with conductors, the field measurements performed by Rydberg atom receivers show promise to be less invasive.

The Rydberg-atom sensors are operated at room temperature as electrometers or receivers and are presented in this thesis in the context of Fig. 1.1. The electrometer and its standard RF counterpart are shown in Fig. 1.1(a) and (b). The input to both is an RF electric field $\mathbf{E}$, and the output is a DC voltage, proportional to the *magnitude* of the field vector. In the electrometer configuration, there is no local oscillator, so only field magnitude measurements can be done. This is useful for electric-field strength measurements and power calibration, where the objective is to quantify the amplitude of a field rather than recover information

encoded within it. The Rydberg-atom receiver and its standard RF counterpart are shown in Fig. 1.1(c) and (d). The input in both receiver is an RF electric field and the output is a time-varying DC voltage oscillating at the beat frequency between the electric field and a local oscillator. Further filtering, demodulating, or a spectrum analyzer is required to recover information from the DC voltage, but once this is done, receivers can be used for communications and detection of modulated signals.

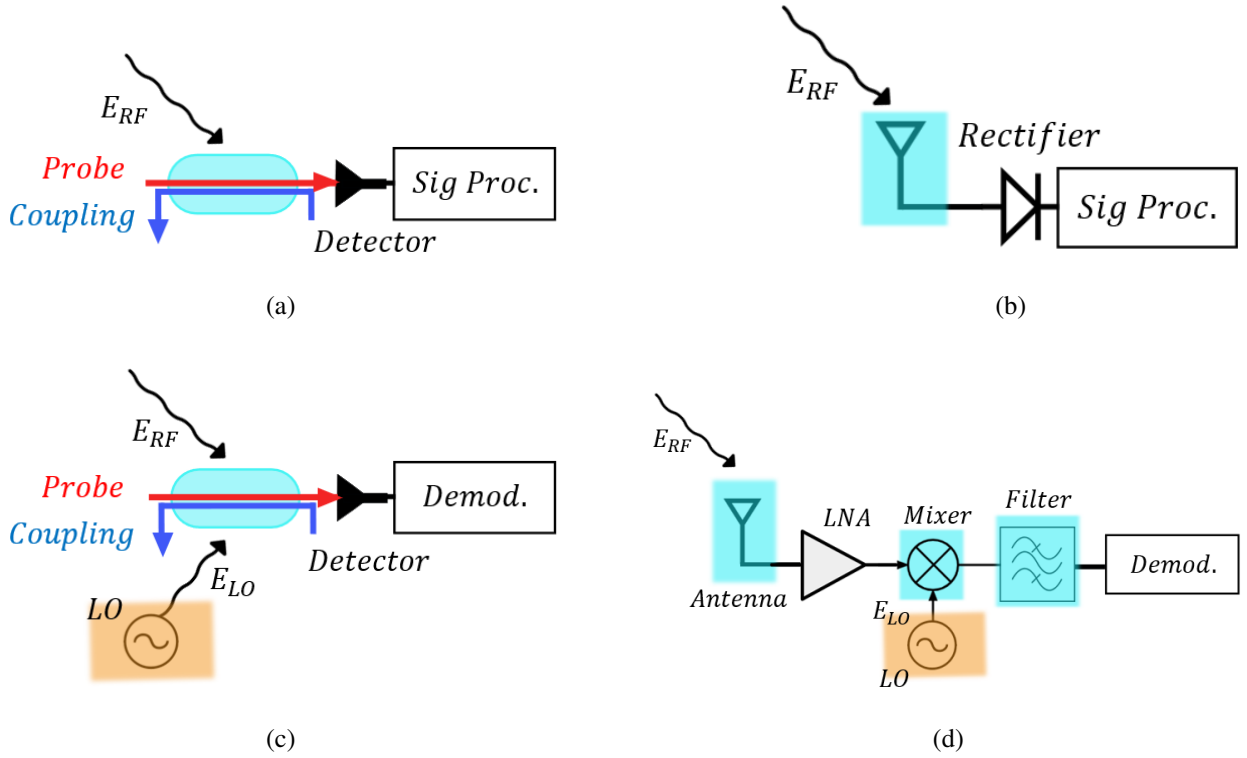


Figure 1.1: (a) A Rydberg-atom electrometer block diagram, compared to (b) a standard RF/microwave antenna coupled to a detector. (c) A Rydberg-atom receiver block diagram, compared to (d) a standard RF/microwave receiver.

At a high level, many components of a Rydberg receiver are analogous to those in a conventional receiver. In a Rydberg receiver, the atomic vapor cell together with the photodetector performs the function of the antenna, whereas in a conventional receiver the receiving antenna is typically a patch, horn, or dipole. The mixer in a Rydberg receiver is typically realized in one of two ways. In one configuration, the RF and

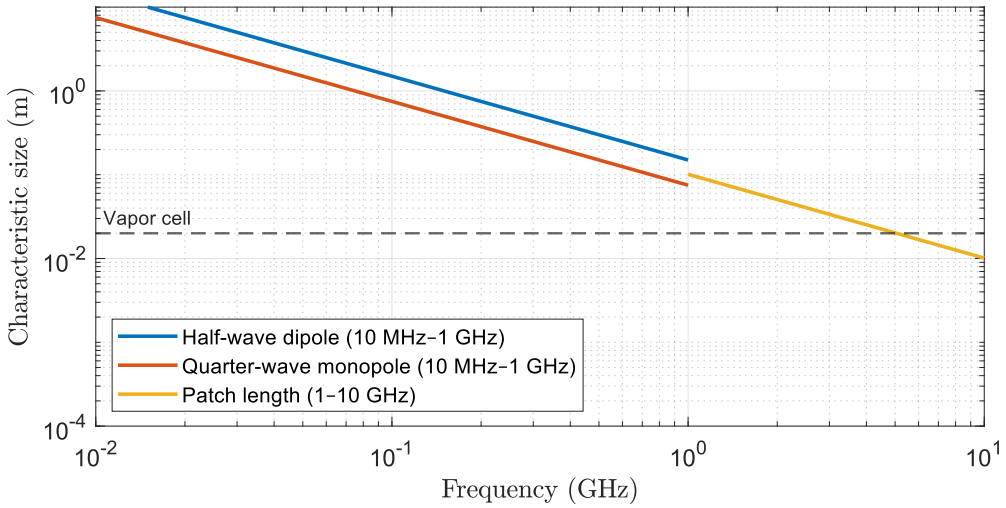
LO signals are combined in a coupler before being transmitted through a horn antenna [49], a topology generally used only in laboratory test setups. Alternatively, the RF and local oscillator (LO) fields are supplied by separate horns and combined directly within the vapor cell. In contrast, a conventional receiver uses a dedicated mixer, which is a three port device used for modulation or demodulation of the received signal. Rydberg receivers also exhibit a very narrow response bandwidth, typically on the order of 10 MHz at most [115] [98] [70], which inherently filters interfering signals. A conventional receiver, by comparison, requires a dedicated filtering stage to achieve similar selectivity. In summary, the vapor cell in a Rydberg receiver combines the functionality of the antenna, mixer, and filter found in a conventional receiver. A visual comparison of a Rydberg receiver and a conventional receiver is shown in Fig. 1.1.

1.1 Background

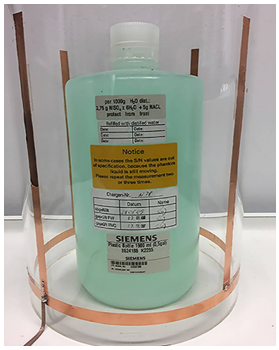
Rydberg receivers are able to measure RF electric field amplitudes with high precision, accuracy, and spatial resolution. For example, a room-temperature Rydberg-atom vapor confined to a 1 cm^3 volume has been shown to detect electric-field amplitudes for a wide tuning range of 2 to 24 GHz, with performance comparable to that of an electrically-small dipole antenna of a similar size [33]. Rydberg electrometry has achieved spatial resolution of $\lambda_0/650$ at 6.9 GHz, where λ_0 is the free-space wavelength of the RF wave [32]. Rydberg-atom receivers have also been used to measure the polarization of the incident RF wave with a resolution better than 1° [95], and the magnitude of the electric field within 1.4% for values ranging from approximately 0.5 to 3 V/m at 20.64 GHz [101].

The Rydberg sensors discussed in this thesis are limited to room temperature electrometers and receivers. They are compared with conventional microwave receivers based on low noise amplifiers, which face several challenges in certain frequency ranges. At lower frequencies, receiving antennas must increase in size to achieve adequate performance, as a result of the Chu-Wheeler-Harrington limit. In contrast, Rydberg receivers scale sensing frequency with laser wavelength, which may mitigate the size constraints imposed on conventional receivers [34]. A comparison of antenna sizes for Rydberg and conventional receivers is shown in Fig. 1.2. At higher frequencies, particularly at Ka-band and above, the noise figure of solid state amplifiers degrades, which can limit the sensitivity of conventional receivers. Rydberg receivers

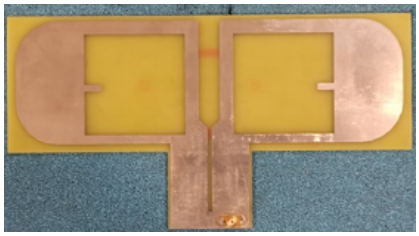
may offer sensitivity advantages in the millimeter wave regime, as discussed in further detail in this thesis. A sampling of cryogenic LNA noise figures as a function of gate length, a constrained parameter in LNA designs, is shown in Fig. 1.3.



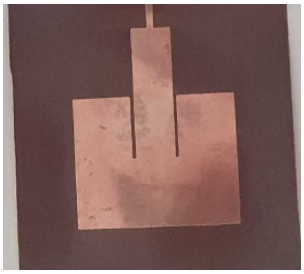
(a)



(b)



(c)



(d)

Figure 1.2: Example antennas: (a) Antenna size versus frequency, from 100 MHz to 1 THz. This assumes that the Rydberg vapor cell is 2 cm long and $\epsilon_{eff} = 2.2$ for a microstrip patch antenna. For comparison, a (b) quarter-wave monopole array [85] that is a minimum of 19 cm tall, (c) half-wave dipole [116] that is 24 cm long, and (d) microstrip patch that is 1.4 cm on the longest side [55].

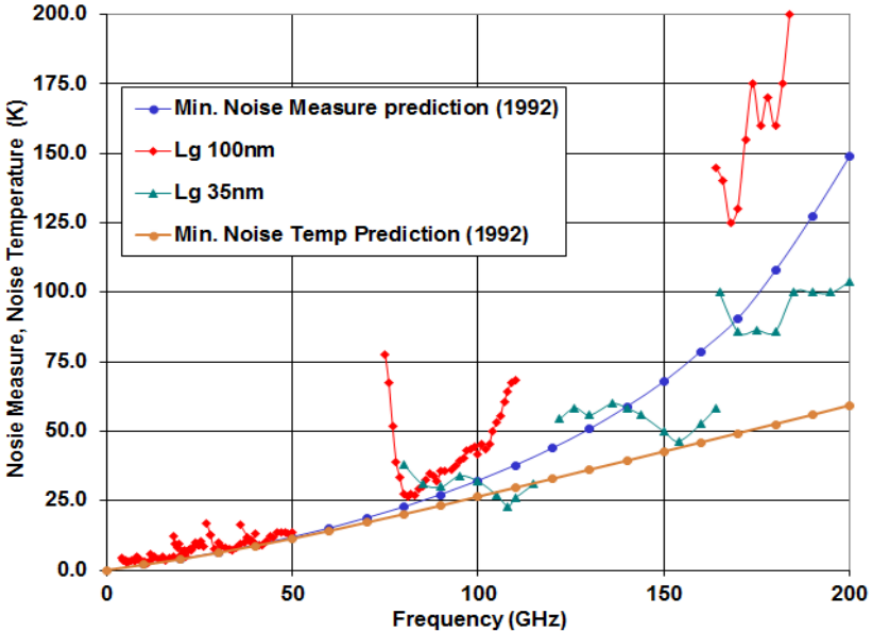


Figure 1.3: State-of-the-art cryogenic amplifiers with minimum noise temperature measurements, as well as predicted bounds [80]. At high frequencies, even at smaller gate lengths and cryogenic temperatures, standard low noise amplifiers are limited in their noise temperature and therefore sensitivity [42]

.

Receivers are used in a wide range of systems, with different applications prioritizing different performance metrics. High sensitivity applications include radio astronomy receivers [109] and internal body temperature sensing radiometers [62]. These systems typically employ amplifiers with low noise figures, often less than 2 dB, and moderate gain of approximately 20 dB. Some receivers are designed for bandwidth-driven applications, such as ultra wideband receivers [67] and spectrum monitoring devices. These systems are often designed for bandwidths greater than an octave, sometimes at the expense of increased noise figure. Lastly, high frequency receivers are commonly used in applications such as automotive radar and imaging radar. These systems typically exhibit higher noise figures, often greater than 3 dB, due to the performance limitations of low noise amplifiers at elevated frequencies [97].

1.2 Rydberg Atoms

A Rydberg atom is created when a population of atoms is excited to a high-energy state, in which the valence electron occupies an energy level far from the atomic nucleus. Any element can be excited to the Rydberg state, but typically alkali atoms are preferred because of their single valence electron [35]. The energy levels in an atom are denoted by spectroscopic notation nL_j, where n is the principal quantum number (orbital level) of the electron, L describes the shape of the energy level, and j corresponds to the total angular momentum of that energy level. An atom is considered to be a Rydberg atom when it occupies a state with a sufficiently high principal quantum number. At large n, the radius of the atom increases by n^2, and the binding energies of the electron decrease as $1/n^2$. This means that less energy is required to transition between successive higher-energy states. A low quantum number means the electron is closer to the nucleus of the atom. The high-energy atom creates a very strong dipole moment which interacts strongly with external fields. For example, rubidium has a ground state of $5\mathrm{S}_{1/2}$, and applying a quantized amount of energy (for example, a 780.24 nm and 480.04 nm laser) it transitions to the Rydberg state $52\mathrm{D}_{5/2}$. The open-source Alkali Rydberg Calculator (ARC) is used to calculate the energy required to transition to higher energy levels [118]. The energy required to transition between standard low-n energy levels, often called the energy gap, is:

$$\Delta E = E_1 - E_2 \tag{1.1}$$

where E_1 and E_2 are the known energy of two different states. These values are measured for a variety of energy transitions [57]. The subsequent laser wavelength needed for this energy transition is then found from:

$$\lambda = \frac{hc}{\Delta E} \tag{1.2}$$

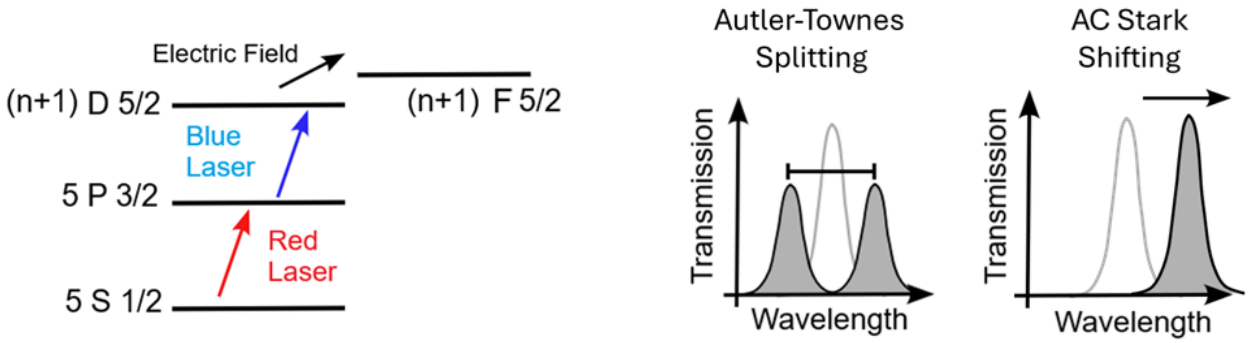
A different equation must be used when calculating the energy transition to a high-n Rydberg state. This is because, as the valence electron is excited far from the nucleus, the hydrogen approximation of atomic structure is valid, and thus, able to be calculated. The equation for Rydberg-state transitions is:

$$E_{nLj} = -\frac{Ry}{(n - \delta_{nLj})^2} \tag{1.3}$$

where n, L, j are previously-defined quantum numbers, Ry is the Rydberg constant, and δ_{nLj} is the quantum defect, which encapsulates the aspects of the energy level that cannot be modeled by hydrogen approximation. The quantum defect is defined for a particular orbital L, and values for most orbital levels are well-known [65]. The Rydberg constant is:

$$Ry = \frac{M}{M + m_e} * \frac{e^4 m_e}{16\pi^2 \epsilon_0^2 \hbar^2} \tag{1.4}$$

where M is the atomic mass of the nucleus, m_e is the electron mass, e is the electron charge, ϵ_0 is the vacuum permittivity, and $\hbar$ is the reduced Planck's constant. Given the above equations, the necessary laser wavelengths and RF fields can be calculated for any energy transition scheme.



(a) (b)

Figure 1.4: (a) A sample atomic energy transition scheme in rubidium, showing successive energy levels and the method by which an atom could be excited to each. (b) Autler-Townes (AT) splitting and AC stark shifting. Both traces show the output from the photodetector in the presence of an electric field (solid dark gray trace) versus the Rydberg-state without external field (unfilled light gray trace).

Many Rydberg receivers use a two-laser topology to provide excitation of the atoms, the energy-levels of which are thoroughly documented [106]. The first laser is referred to as the *probe* laser. It excites the

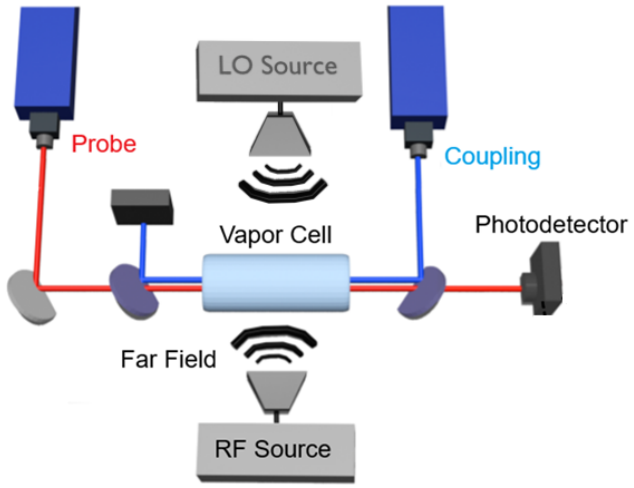
atoms to an intermediate state between the ground and Rydberg states. Rubidium exhibits fluorescence, a phenomenon where atoms emit absorbed energy as a photon that can be observed with the naked eye, when excited from the ground state $5S_{1/2}$ to an intermediate state at $5P_{3/2}$ via a laser with wavelength 780.24 nm, so this is an often-chosen intermediate state for many Rydberg set-ups. The second laser is the *coupling* laser, which supplies the additional energy necessary to reach the Rydberg state. The lasers must be co-polarized to properly interact. A two-photon energy transition scheme is shown in Fig. 1.4.

A plethora of energy transitions exist in the rubidium atom, enabling sensing at a variety of frequencies. For example, in X-band, there exists the following transition scheme: ground state ($5S_{1/2}$) to intermediate state ($5P_{3/2}$) via 780.24 nm laser, to Rydberg state ($59D_{5/2}$) via 479.81 nm laser, and the final AT splitting state ($60P_{3/2}$) via an external 10.22 GHz RF field. A similar scheme is possible in V-band: $5S_{1/2}$ (ground state) $\rightarrow 5P_{3/2}$ (intermediate state, 780.24 nm laser) $\rightarrow 34D_{5/2}$ (Rydberg state, 481.43 nm laser) $\rightarrow 33F_{7/2}$ (AT split, 61.32 GHz field). Note that both schemes excite to the same intermediate state, with the determining factor between the two configurations being the secondary laser wavelength and the external electric field. Thus, it is possible for a singular Rydberg receiver to detect both X-band and V-band signals, given a coupling laser that can tune from 479.81 to 481.43 nm. This is achievable with the majority of commercially-available laser systems, which can provide up to 20 nm coarse tuning range.

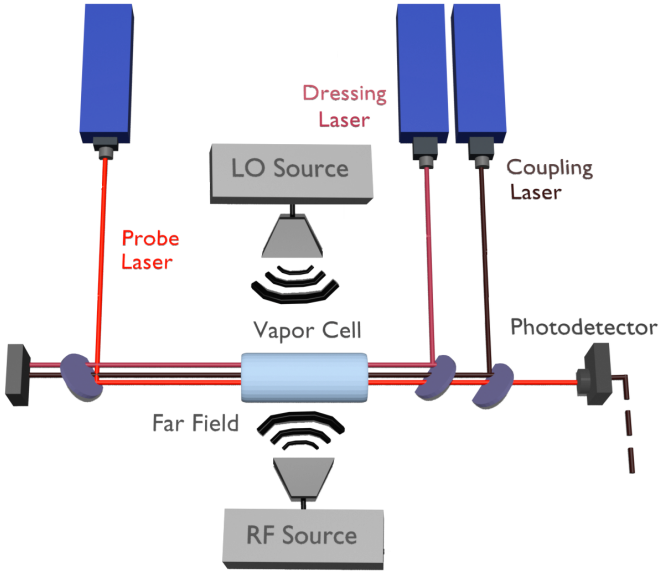
1.3 EIT, AC Stark Shifting, and AT Splitting

In the two photon excitation scheme, both lasers are required to reach the Rydberg state. If only one laser is present, the rubidium atoms do not reach the necessary excitation energy and therefore absorb the probe laser light. However, when the atoms are excited to the Rydberg state, they no longer interact strongly with the probe laser, allowing the probe light to transmit through the vapor cell and be detected by the photodetector. This phenomenon is known as electromagnetically induced transparency (EIT) [15]. EIT occurs because the high power coupling laser creates a coupled atom–laser system, referred to as a dressed state. The dressed state produces new energy levels that are slightly shifted from the original atomic energy levels. The superposition of these positive and negative energy shifts leads to destructive interference between excitation pathways. As a result, when atoms decay from the Rydberg state to the intermediate

state, the transition pathways interfere and cancel, producing the transparency window associated with EIT. When a microwave field is incident on the atoms, it introduces an additional energy level that the atoms can occupy. As a result, the single EIT resonance splits into two peaks that are separated in optical frequency. This phenomenon is referred to as Autler Townes (AT) splitting. A visualization of the EIT and AT splitting is shown in Fig. 1.4b.



(a)



(b)

Figure 1.5: (a) A two-photon excitation scheme, as well as (b) a three-photon Rydberg scheme, with the probe, coupling, and dressing lasers. Additional electronics (not pictured) are necessary to interrogate laser wavelength and lock the lasers to the necessary transition.

In addition to two-photon excitation schemes, three-photon excitation schemes are commonly used with cesium and provide excitation via a third *dressing* laser [23] [88]. This topology corresponds to an energy transition scheme with two intermediate states before the Rydberg state, as opposed to the single

intermediate state in the two-photon configuration. Three-photon Rydberg-atom electrometers have the potential to increase resolution by reducing linewidth, which reduces Doppler broadening and can access a wider range of energy transitions compared to two-photon receivers. However, this comes at the cost of additional components and increased laser stabilization requirements. A two-photon and three-photon Rydberg-atom receiver topology is shown in Fig. 1.5.

The magnitude of splitting between the two peaks in the AT splitting state directly corresponds to the amplitude of the incident electric field, such that:

$$\Omega = \frac{\rho * E}{\hbar} \tag{1.5}$$

where ρ is the dipole moment of the atom, $\hbar$ is reduced Planck's constant, E is the magnitude of the electric field, and Ω is the distance between Autler-Townes splitting peaks in the frequency domain, also referred to as the Rabi frequency. Thus, this measurement is self-calibrating because the splitting is directly proportional to the magnitude of the electric field and fundamental constants. As a plethora of energy transitions exist in Rubidium, Rydberg-atom receivers exhibit a narrowband response around the transition frequency and can respond to a range of frequencies, from low frequencies such as 347.32 MHz corresponding to the $179\mathrm{D}_{5/2}$ transition to very high frequencies such as 1.012 THz corresponding to the $14\mathrm{D}_{5/2}$ transition.

However, for AT splitting to occur, the frequency of the incident RF signal must correspond to an energy level transition in the Rydberg atom. If this is not the case, then AC stark shifting occurs instead, which is indicated by an offset of the EIT peak in the frequency domain, as expressed in this equation:

$$\Delta f = -\frac{1}{4}\alpha E^2 \tag{1.6}$$

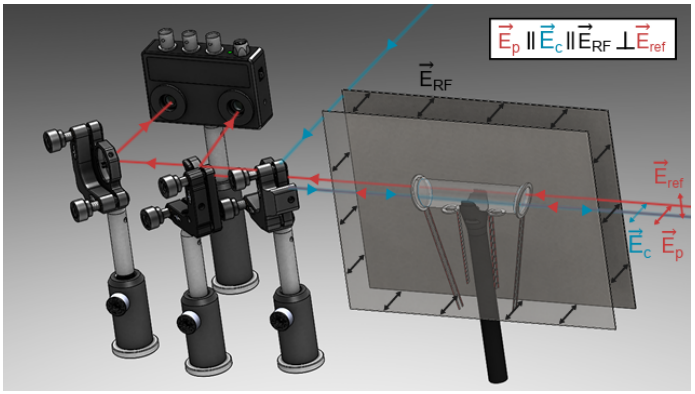
where Δf is the frequency shift of the EIT peak, α is the polarizability of the atomic transition, and E is the magnitude of the electric field.

Off-resonant sensing schemes are intrinsically less sensitive than on resonant schemes because the induced frequency shifts are much smaller in magnitude and the quadratic dependence on $|E|$. As a result, the off-resonant configuration typically imposes a more significant limitation on achievable sensitivity. AC

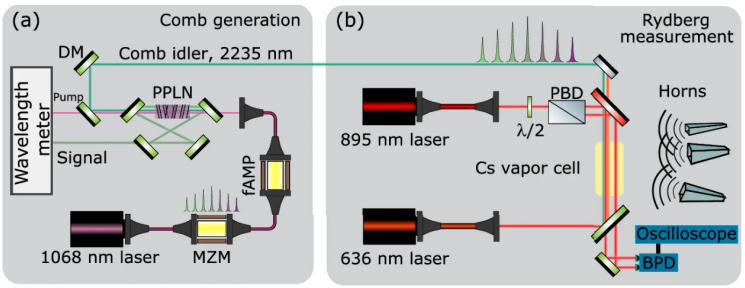
Stark shifting was first used for measurement by Zimmerman et al. in 1979 [117]. Shortly afterward, Rydberg atoms were used in an on resonant measurement configuration in a 100 GHz detector [35]. These experiments yielded a room temperature noise equivalent (NEP) of 5×10^{-15} W$/\sqrt{Hz}$. The first off-resonant Rydberg measurements were made by Osterwalder and Merkt in 1999 from 120–180 GHz, with the ability to sense fields as low as 20 $\mu V/cm$. Successive Rydberg systems have further improved on measurement sensitivity, with detection thresholds improving to 500 μV/m/$\sqrt{\text{Hz}}$ at 7 GHz in a homodyne optical detection scheme in 2017. A host of techniques have been proposed in the 21st century to further improve the sensitivity of Rydberg receivers and to expand the regime in which Rydberg receivers are effective. One method is referred to as the "RF photon ladder" in which additional RF sources are used to access lower frequency transitions that are not typically accessible in the two-photon scheme [1].

1.4 Previous Rydberg Demonstrations

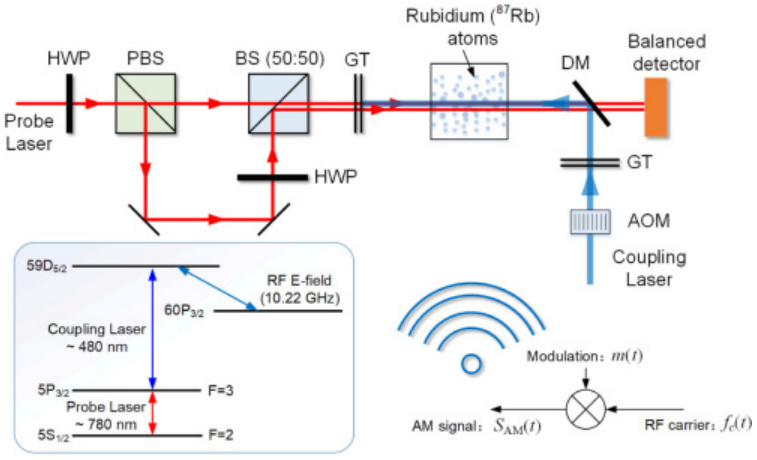
In the literature, the vast majority of Rydberg receivers operate in the 1–20 GHz frequency regime and employ either a two photon or three photon excitation configuration to reach the Rydberg state. Sampling is typically performed in either an electrometer (homodyne) configuration or a receiver (heterodyne) configuration. Most demonstrations focus on improving receiver sensitivity through modifications to either the optical interrogation scheme or the microwave coupling topology. Variations in these configurations include different optical detection methods, RF coupling geometries, and excitation schemes. Methods aimed at improving receiver performance will be discussed in greater detail in Chapter 3. Some example Rydberg-atom receiver topologies, including two-photon and three-photon receivers in cesium, rubidium, and potassium, are shown in Fig 1.6.



(a)



(b)



(c)

Figure 1.6: (a) A two-photon Rydberg-atom receiver in potassium, using 480 nm and 456 nm lasers [40]. (b) A three-photon receiver in cesium using 636 nm, 895 nm and 2235 nm lasers [83]. (c) A two-photon receiver in rubidium, using 480 nm and 780 nm lasers [104].

The current state of the art sensitivity for a Rydberg electrometer has been demonstrated at 13.9 GHz, achieving a noise equivalent field (NEF) of $0.39\,\mu\mathrm{V}/\mathrm{m}/\sqrt{\mathrm{Hz}}$, which was thermally-limited [16]. This sensitivity metric, and how it relates to more conventional receiver metrics such as noise equivalent temperature (NET) and noise figure (NF), will be discussed in Chapter 2. The receiver reported in [16] achieves this sensitivity using a photon counting detection scheme that measures individual photons rather than the aggregate response of a photodetector. While this approach significantly improves sensitivity, it also limits the amount of information that can be encoded in the received signal, and is not typical in the Rydberg receiver literature. A table summarizing the demonstrated performance of published Rydberg receivers is shown in Table 1.1.

Table 1.1: Noise-equivalent field (NEF) measurements for Rydberg-atom E-field sensors

Source	**Year**	**Frequency [GHz]**	**NEF (μV/m/$\sqrt{\text{Hz}}$)**	**Technique**	**On/Off Res**
[28]	2018	0.0001	14000	Homodyne	Off
[96]	2012	14.2	3000	Absorption	On
[59]	2017	5.05	500	Homodyne	On
[33]	2015	14.0	300	Homodyne	On
[82]	2024	0.162	100	HAMMER	On
[39]	2019	19.6	79	Heterodyne	On
[52]	2022	5.00	71.2	Heterodyne	Off
[31]	2023	2.30	70.5	Heterodyne	On
[103]	2024	6.65	28.02	Heterodyne	Off
[71]	2024	13.9	17.9	N-wave Mixing	On
[66]	2024	0.223	17.9	Resonator	Off
[19]	2023	0.655	13	Homodyne	On
[54]	2020	6.95	5.5	Superheterodyne	On
[84]	2021	17.0	3	Repumping	On
[92]	2024	10.2	1.58	Resonator	On
[21]	2022	10.7	1.25	Param Optimization	On
[22]	2023	6.51	0.51	Param Optimization	On
[16]	2023	13.9	0.39	N-wave Mixing*	On

* [16] implemented with unique method not comparable to other receivers.

1.5 Thesis Organization

This thesis will talk about Rydberg atoms in free-space and field-confined set-ups, with on-resonant and off-resonant measurements, and in electrometer (homodyne) and receiver (heterodyne) configurations.

The work in this thesis was advised by Professor Zoya Popovic at the University of Colorado at Boulder and performed in Professor Dana Anderson's lab space in the Duane Physics building with funding from Lockheed Martin. Some measurements were taken in collaboration with Infleqtion, a quantum technology company located in Boulder.

This thesis is organized as follows. Chapter 1 introduces the background and fundamental concepts relevant to this work. It begins with a general overview of the motivation for Rydberg-atom–based sensing, followed by a discussion of the necessary physics of Rydberg atoms. It also details the methods by which sensing is achieved, notably through electromagnetically-induced transparency (EIT), AC Stark shifting, and Autler–Townes (AT) splitting. Finally, previous demonstrations of Rydberg-based receivers and sensors are summarized to provide context for the work presented in this thesis.

Chapter 2 introduces the figures of merit used to evaluate receiver performance. Metrics such as sensitivity, noise-equivalent field (NEF), and noise-equivalent temperature (NET) are defined and discussed. These metrics are then used to compare Rydberg receivers with conventional LNA-based receivers. Additional considerations including system size, power consumption, and bandwidth are also examined.

Chapter 3 presents methods for enhancing the sensitivity of Rydberg-based receivers. An enhancement factor is defined and used to evaluate different approaches. The chapter then summarizes the previously-published topologies that have been used to achieve microwave enhancement, and introduces the use of a waveguide resonator for field enhancement. Two resonator designs at 15 GHz and 10.22 GHz are discussed, including simulations, RF characterization measurements, and full receiver-integrated measurements.

Chapter 4 presents a frequency-tunable resonator design at 10.22 GHz and 10.77 GHz. Similar metrics as those discussed in Chapter 3 are used to characterize this resonator, with additional analysis to quantify the performance trade-off between frequency tunability and sensitivity.

Chapter 5 investigates Rydberg sensing at higher frequencies in the millimeter-wave regime. The optical experimental setup is described, followed by measurements demonstrating millimeter-wave detection and an analysis of the role of polarization mis-match in the set-up. A high-frequency field enhancement technique is also introduced.

Chapter 6 examines the operation of Rydberg receivers at low frequencies using electrically small

Rydberg sensors. The limitations encountered in this regime are discussed, and experimental optical setup and measurement results are presented.

Finally, Chapter 7 summarizes the conclusions of this work and outlines potential directions for future research. In particular, the use of a microwave local oscillator for heterodyning is discussed.

Chapter 2

Figures of Merit for Receivers

Conventional receivers are typically characterized using two metrics: noise and dynamic range. The noise is the expressed as a relationship between the signal at the input S_i and the noise contributions of the input N_i to the signal S_o and noise N_o at the output of the device such that the noise factor F is:

$$F = \frac{S_i/N_i}{S_o/N_o} \tag{2.1}$$

In units of dB, this is called the noise figure (NF), such that:

$$\text{NF} = 10\log_{10}(F) \tag{2.2}$$

The relationship between the signal and noise at a given point is the signal-to-noise ratio (SNR), and is typically defined relative to an ambient temperature $k_B T_0$, where T_0 is the reference temperature in Kelvin and k_B is Boltzmann's constant. At room temperature, which is the most common reference temperature, $T_0 = 290\,\text{K}$. In a conventional receiver, the low noise amplifier also contributes gain to the system, and has a considerable impact on the noise of the system. Given an amplifier with gain G, it is possible to re-define the output noise and signal to be:

$$S_o = GS_i \quad \text{and} \quad N_o = GN_i + N_{Ao} \tag{2.3}$$

where N_{Ao} is the noise from the amplifier measured at the output, and is equal to $N_A G$. Substituting the above expressions into Eq. (2.1), we have an expression expressed solely in terms of noise:

$$F = 1 + \frac{N_A}{N_i} \tag{2.4}$$

where N_A is the noise from the amplifier measured at the input. Eq. (2.5) expresses the system noise relative to input (ambient temperature). It is also possible to express the noise relative to the noise temperature of the amplifier, given that $T_A = N_A/k$:

$$F = 1 + \frac{T_A}{T_0} \tag{2.5}$$

These metrics are often applied at the component level; at the system level, noise-equivalent temperature (NET) is often used. NET is the incident signal temperature required to equal the detector's internal noise, thereby producing a signal-to-noise ratio of one. Dynamic range is the range of operation over which a receiver can be approximated as linear, meaning that the output power is directly proportional to the input power [81]. A good receiver is characterized by high sensitivity and wide dynamic range. This chapter examines the ideal performance metrics of a Rydberg receiver. It begins by discussing the sensitivity limitations of Rydberg receivers and converting the sensitivity metric commonly used for such receivers, noise-equivalent field (NEF), into an equivalent noise temperature. It then outlines the assumptions required for this conversion and concludes with a discussion of limitations in size, power consumption, and bandwidth.

2.1 Sensitivity

Free-space-coupled Rydberg-atom receivers are typically characterized by the noise-equivalent field (NEF), with units of $\mathrm{V/m/\sqrt{Hz}}$. The NEF includes contributions from a variety of internal and external sources, and is defined as

$$\mathrm{NEF} = \frac{|E_{\min}|}{\sqrt{\Delta f}}, \tag{2.6}$$

where $|E_{\min}|$ is the minimum detectable microwave electric field and Δf is the measurement bandwidth of the photodetected signal. External contributions to the NEF include thermal noise from the environment and quantum fluctuations of the microwave field when a Rydberg-aton sensor is in the heterodyne configuration.

Internal contributions include fluctuations in the probe laser as it propagates through the atoms, probe photon shot noise, and photodetector electronic noise. These sources are generally treated as uncorrelated [94].

In principle, the theoretical sensitivity of heterodyne Rydberg receivers is limited by two sources: the blackbody limit due to thermal noise and the vacuum limit due to quantum fluctuations, both of which are external noise contributions [94]. Thermal noise imposes an effective sensitivity limit of approximately $0.24\,\mu\mathrm{V/m/\sqrt{Hz}}$ for Rydberg sensors in the X-band, while quantum noise imposes an additional limit of $6.8\times10^{-3}\,\mu\mathrm{V/m/\sqrt{Hz}}$. These theoretical limits, along with NEF values reported for demonstrated Rydberg receivers operating from 100 MHz to 20 GHz, are shown in Fig. 2.1.

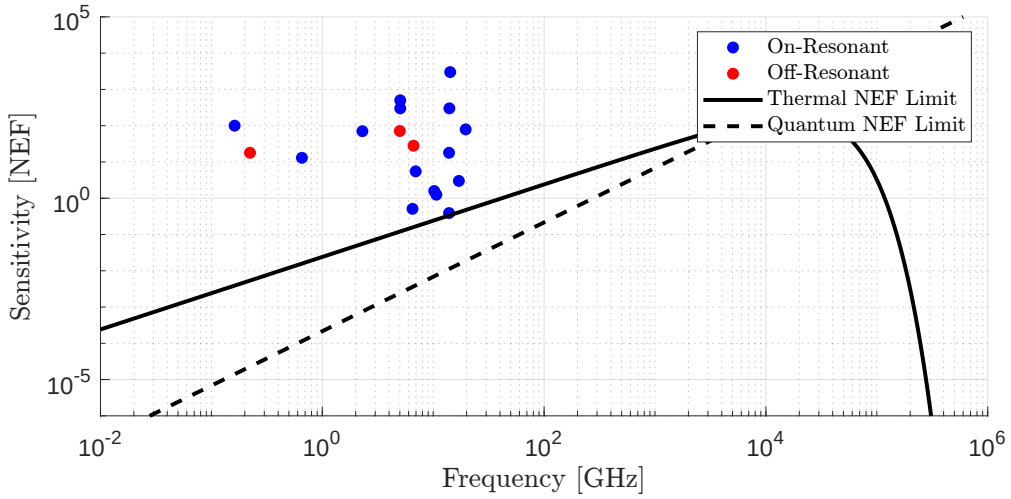


Figure 2.1: Theoretical limits set by thermal and quantum background noise, plotted alongside the sensitivity of several Rydberg receivers reported in the literature. The data point that intersects the thermal NEF line employs a unique sampling method that is not constrained by typical Rydberg measurement limits.

Several practical measurement factors also affect sensitivity. Finite laser linewidths are among the main contributors, since broader spectral peaks are more difficult to resolve in the case of Rydberg-atom electrometers. In addition, laser locking is important because the wavelength must remain fixed at a known value. Different transition schemes require different optical power levels, with lower-frequency transitions requiring more power to achieve the same resolution. For example, a blue laser operating at 30 mW may resolve the electric-field magnitude for the $34\mathrm{D}_{5/2}$ to $33\mathrm{F}_{7/2}$ transition (61.32 GHz), but fail to resolve a

measurement for the $34\mathrm{D}_{5/2}$ to $59\mathrm{D}_{5/2}$ transition (10.22 GHz), simply because the lower-frequency transition requires more power. This is because the necessary optical power required to excite an atom to a given energy state is directly tied to the Rabi frequency of the transition. Additionally, the red laser power is typically kept below 0.1 mW to avoid saturating the atoms.

The quality and properties of the vapor cell also affect the NEF. Improved sensitivity can be achieved with a longer interaction length, since a larger rubidium volume produces a stronger atomic response. In addition, factors such as vapor density, static charge accumulation on the cell walls, and interactions between the laser and the glass walls can degrade sensitivity. Measurements can also be affected by the angle of arrival of the RF signal, since proper overlap between the RF, LO, and the optical polarization is desirable, as well as by environmental noise contributions. The quantum receiver is sensitive to all sources of incident fields, including both the intentional signal and unwanted noise from the room-temperature environment, as well as the random quantum fluctuations of microwaves about their ground-state energy.

It is possible to express the sensitivity of a conventional microwave receiver as an NEF value, and therefore as a free-space measurement, to enable comparison with a Rydberg receiver. Similarly, the free-space sensitivity of a Rydberg-atom receiver can be converted into a noise figure.

2.2 Comparing to Conventional Receivers

As emphasized in [94], two comparison frameworks may be considered. In a free-space comparison, the atomic receiver is compared to a conventional receiver with an antenna-fed LNA and mixer, and translates the typical receiver noise figure into an NEF value. For this conversion, the result heavily depends on the assumed antenna aperture or gain. In contrast, a port-coupled comparison defines an equivalent receiver noise temperature for the atomic frontend directly, removing the impact of antenna choice.

2.2.1 Free-Space Method

In a standard microwave receiver, the noise figure is typically dominated by the low-noise amplifier (LNA). To compare the noise of an LNA with that of a free-space-coupled atomic receiver, consider an LNA connected to an antenna with gain G. The input power is

$$\mathrm{P_{in}} = G\frac{\lambda_0^2}{4\pi}\frac{|E_{RF}|^2}{2\eta_0} \tag{2.7}$$

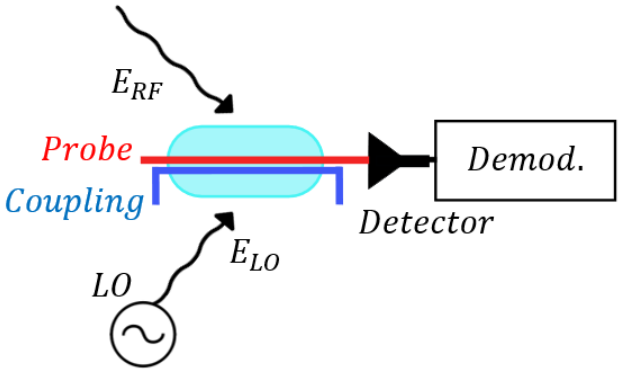
where G is the antenna gain, λ_0 is the free-space wavelength, and η_0 is the free-space impedance (377 ω). In addition, the noise floor of the LNA is $k_B T_{LNA}\Delta f$, where k_B is Boltzmann's constant, T_{LNA} is the noise temperature of the LNA, and Δf is the bandwidth. Rearranging Equation (2.7) for $|E_{RF}|$ and setting the input power equal to the noise floor yields the minimum resolvable electric-field magnitude:

$$|E_{RF}| = \sqrt{\frac{8\pi f^2}{\epsilon_0 c_0^3 G}}\sqrt{k_B T_{LNA}\Delta f} \tag{2.8}$$

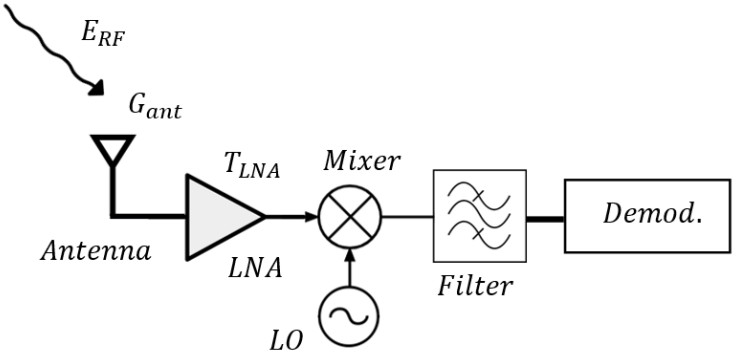
where c_0 is the speed of light in vacuum and ε_0 is the vacuum permittivity. This electric field can be converted into a bandwidth-independent noise-equivalent field by dividing by the square root of the measurement bandwidth:

$$\mathrm{NEF_0} = \sqrt{\frac{8\pi f^2}{\epsilon_0 c_0^3 G}}\sqrt{k_B T_{LNA}} = \sqrt{\frac{8\eta_0 \pi k_B T_{LNA}}{G\lambda_0^2}}. \tag{2.9}$$

From (2.9), it is clear that the NEF of a conventional microwave receiver depends strongly on the gain of the antenna used. Additionally, the reception pattern of a Rydberg sensor is approximately the same as that of a short dipole so the comparison is more equivalent in this regard [7]. Although there are multiple ways to choose the antenna gain to provide a fair comparison [94], the most optimistic case for Rydberg-atom receivers corresponds to a low-performing receiving antenna, which, if lossless, has a lower bound of $G = 3/2$. This corresponds to a small dipole antenna. Thus, an ideal method of comparison would be independent of antenna parameters.



(a)



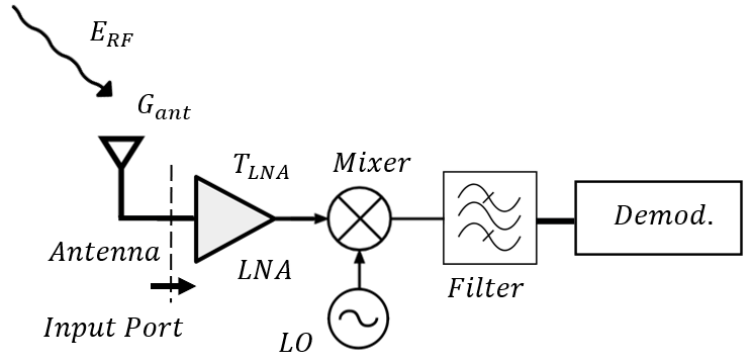
(b)

Figure 2.2: (a) Sketch of Rydberg atom-based microwave receiver. In the free-space treatment, we do not assume anything about it's performance or set-up. Compared to a conventional receiver topology (b), with an assumption that the LNA has sufficient gain and dominates receiver performance, with a given noise temperature, and a receiving antenna with a particular gain.

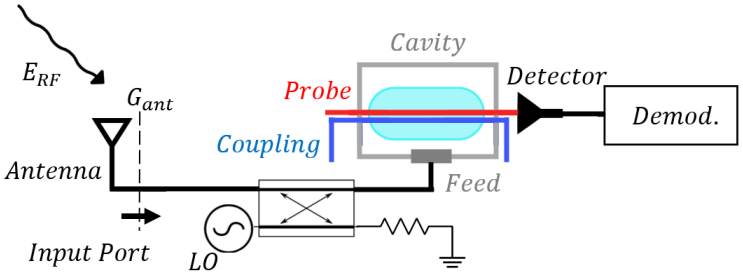
With a sensitivity metric established, it is possible to make a fair comparison between atomic and conventional microwave receivers. Several underlying assumptions are required to determine the sensitivity of a conventional receiver, including the neglect of thermal background contributions and the assumption of a receiver topology that includes an LNA. A visual comparison of a conventional receiver and a Rydberg receiver is shown in Fig. 2.3. As an example, consider an X-band comparison between a conventional receiver and a Rydberg receiver. Given a specific LNA, such as the Mini-Circuits PMA-183PLN-D+ LNA, a representative noise figure can be assumed for the conventional receiver. For this component, the noise

figure is 1.3 dB, corresponding to a noise temperature of approximately 100 K. A low-gain, electrically short dipole with $G = 3/2$ is chosen. It is also reasonable to assume a small dipole because the geometry and size can be easily compared to the volume encompassed by a small vapor cell. In the conventional case, this results in a receiver sensitivity of $0.098\,\mu\mathrm{V/m/\sqrt{Hz}}$. This is approximately four times more sensitive than the state-of-the-art Rydberg receiver reported in [17]. Therefore, for Rydberg-atom receivers to become competitive with standard receivers, some form of field enhancement is required. This will be discussed further in Chapter 3.

2.2.2 Port-Coupled Method



(a)



(b)

Figure 2.3: (a) Rydberg atom-based microwave receiver. In the port-coupled treatment, we assume the same antenna is connected to (a) as in the conventional case (b). This forumlation is useful for quantifying sensitivity enhancement.

A fairer comparison between Rydberg receivers and conventional receivers involves introducing a microwave port that feeds the vapor cell, as illustrated in Fig. 2.3. With this approach, a receiver noise temperature can be defined and directly compared with that of a conventional frontend, such as an LNA. In the port-coupled model, an important underlying assumption is that the electric field is coupled through an input port and is therefore independent of antenna gain. This can be done with a structure such as a metallic resonator. In the vapor cell, the electric field is defined as $|E_{in}| = K\sqrt{P_{in}}$ at the location where the atoms are probed inside the vapor cell. The constant K encapsulates the physical properties of the vapor cell and its accompanying structure. An electromagnetic structure that locally enhances the electric-field magnitude within the vapor-cell volume interacting with the laser beams can be designed to improve sensitivity, and will be further discussed in Chapter 3.

2.3 Rydberg Sensitivity Examples

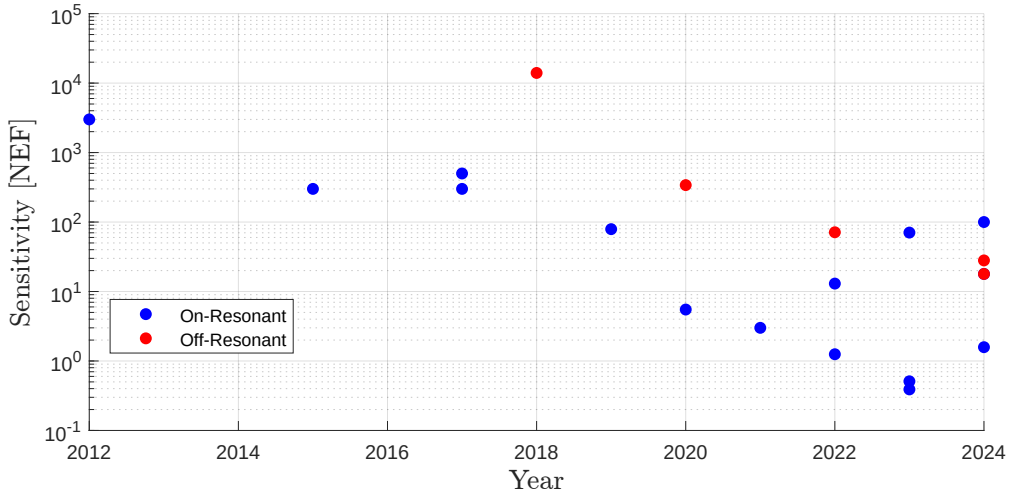


Figure 2.4: Sensitivity in units μV/m/$\sqrt{\text{Hz}}$ for a variety of Rydberg electrometers and receivers. Both on-resonant and off-resonant configurations trend towards higher sensitivities with time.

The sensitivity of Rydberg receivers has been continually refined over the years since the sensing properties of Rydberg atoms were first explored in the 1980s, as seen in Fig. 2.4. The current state-of-the-art sensitivity for a Rydberg electrometer is $0.39\,\mu\text{V}/\text{m}/\sqrt{\text{Hz}}$ at 13.9 GHz [16]. This paper utilizes a unique

sampling method that detects singular photons as opposed to an aggregate photodetector response. This effectively increases the sensitivity at the cost of limiting the amount of information that could be contained in the response. Thus, this Rydberg electrometer was sensitivity limited by the thermal background. State-of-the-art sensitivity has typically been achieved in Rydberg receivers that are in the on-resonant configuration, where the RF frequency is carefully chosen to correspond to atomic energy levels, and measured using the AT splitting. The best on-resonant sensitivities include:

Table 2.1: On-resonant Rydberg receiver sensitivities

Source	**Year**	**Frequency [GHz]**	**NEF (μV/m/$\sqrt{\text{Hz}}$)**
[92]	2024	10.2	1.58
[16]	2023	13.9	0.39
[84]	2021	17.0	3
[21]	2022	10.7	1.25
[22]	2023	6.51	0.51

Off-resonant excitation schemes are intrinsically less sensitive to incident electric fields, due to the lower dipole moment, and therefore are a less-often used topology in sensitivity-focused Rydberg set-ups. Some sensitivities from off-resonant set-ups include:

Table 2.2: Off-resonant Rydberg receiver sensitivities

Source	**Year**	**Frequency [GHz]**	**NEF (μV/m/$\sqrt{\text{Hz}}$)**
[52]	2022	5.00	71.2
[103]	2024	6.65	28.02
[66]	2024	0.223	17.9
[28]	2018	0.0001	14000

A survey of Rydberg receiver and electrometer sensitivities are shown in Fig. 2.5, in which they are

compared to demonstrated LNA values.

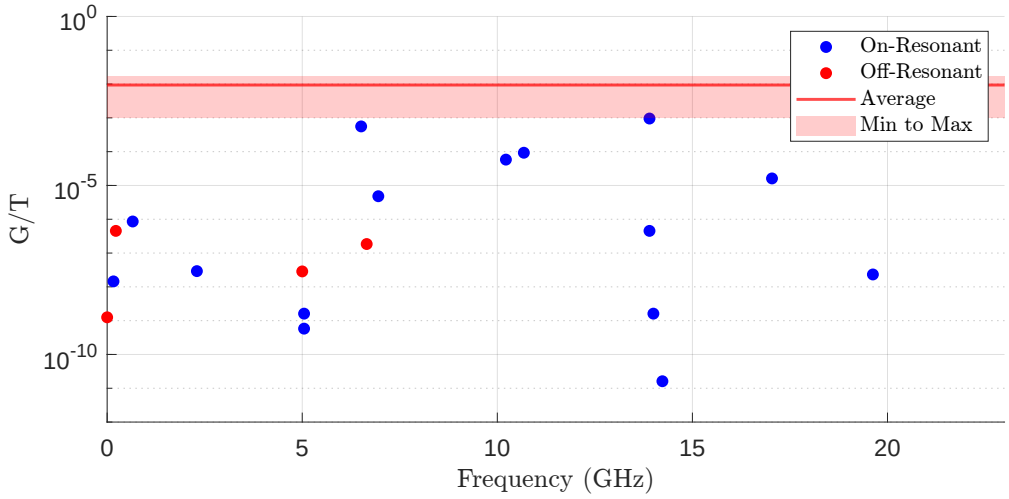


Figure 2.5: The sensitivity (expressed as gain over noise equivalent temperature) versus frequency for a variety of Rydberg receivers, in both off and on-resonant configurations. This sensitivity is expressed as a G/T value. In the figure, the red band represents the sensitivity of a sample of conventional, low-noise amplifier-based receivers, assuming each one is connected to dipole with gain 3/2. [9] The NET of the conventional receivers is found from the the LNA, the first of which, in a cascaded system, would dominate the noise temperature.

2.4 Size, Power Consumption, and Bandwidth

To date, the literature on Rydberg receivers shows that most are confined to optical tables, such as the one shown in Fig. 2.6. This is a function of the high accuracy required for proper laser alignment, and places a lower limit on the size of a Rydberg receiver. Even if the size between individual optical components can be reduced, a minimum of two cavity-based diode lasers are required for energy excitation, which, if combined, occupy a volume of at least $18 \times 15 \times 37$ cm for the two laser heads and $15 \times 45 \times 35$ cm for the control unit. This does not take into account any external wavelength monitoring or laser locking systems, which will contribute additional volume to the receiver, but are necessary for higher sensitivity measurements. It is possible to mitigate some of the in-situ size limitations using fiber optic cables, to move the vapor cell itself off an optical table as in [46], but the larger optics are still associated with the receiver. In terms of size,

vapor cells with a sufficient number of atoms can only be miniaturized to a certain volume, usually with a diameter of a few millimeters. Too-small cells will also yield degraded sensitivities, as receiver sensitivity is a function of interaction length. This can be seen with the micro-machined cell in [38], which has a cavity volume of $2 \times 2 \times 1.4$ mm, but exhibits a minimum sensitivity of $1000\,\mu\mathrm{V}/\mathrm{m}/\sqrt{\mathrm{Hz}}$ at 15.1 GHz.

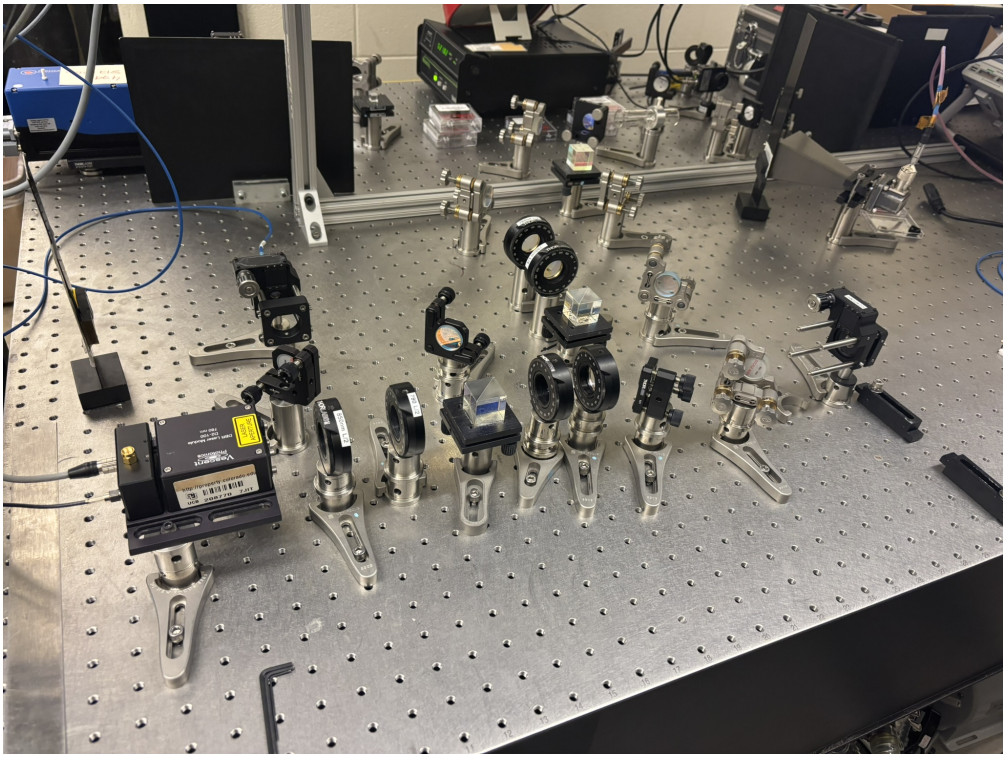


Figure 2.6: Rydberg receiver optical components mounted to an optical table, which encompasses an area approximately 75 by 125 cm. This photo does not show the associated electronics for controlling the laser heads, which are on a rack above the table, and also have a footprint of approximately 75 by 125 cm.

Though the optical power required for Rydberg receivers is low, on the order of hundreds of mW or less, these powers are generated by wall-plug diode lasers with low efficiency, generally around 1%. Thus, the power consumption is on the order of 10-100 W for a single laser. This does not take into account the power consumption of additional electronics for laser stabilization, photodetector readout, and local oscillator generation in heterodyne receivers.

Rydberg receivers are also bandwidth-limited as a function of the atomic response time. The majority

of published receivers exhibit bandwidths from 1-10 MHz, such as in [48]. Some studies have been conducted on the relationship between bandwidth and other parameters in a Rydberg receiver, such as [51], which achieved a maximum response bandwidth of about 6.8 MHz. They found that bandwidth decreases with probe Rabi frequency, which is directly proportional to laser power, and scales with frequency. This means that there is potential for better bandwidths at higher frequencies, when laser power is lower. Bandwidth is also inversely proportional to beam waist. Smaller waists improve bandwidth but reduce atom number and therefore sensitivity.

Some of the contributions of this chapter are published in [92] and [91]. In particular, the discussion and interpretation of sensitivity metrics is given in detail in [92], while the discussion on bandwidth and interpretation of comparison to the state-of-the art is given in [91].

Chapter 3

X-band and Ku-band Sensitivity Enhancement

From the comparison with conventional receivers, it is evident that some method of enhancement must be used to make Rydberg receivers more sensitive. This chapter examines resonant-structure enhancement as a method for improving the sensitivity of Rydberg-atom microwave receivers. The discussion in this chapter introduces the enhancement factor used to quantify this improvement, reviews previously demonstrated optical and microwave enhancement approaches, and then demonstrates the use of metallic waveguide resonators as a solution due to their high quality factor, structural robustness, and compatibility with laser-interrogated vapor cells. Design considerations such as field uniformity, interaction length, and coupling regime are also introduced as key parameters for overall receiver performance.

3.1 Enhancement Factor (F)

To quantify the impact that an enhancement structure has on a Rydberg receiver, we define an enhancement factor F, which is a ratio of the internal field in the cavity to the external field:

$$F = \frac{|E_{in}|}{|E_{ext}|} \tag{3.1}$$

where $|E_{in}|$ is the magnitude of the RF electric field inside the vapor cell with enhancement, and $|E_{ext}|$ is the electric field without the enhancement method. We assume that E_{in} is measured in the same environment as $|E_{ext}|$, e.g. at a specific input power and specific polarization. The external field is $E_{ext} = \sqrt{P_{in} 8 \eta_0 \pi / (G\lambda^2)}$, where G is receiving antenna gain, η_0 is the free space impedance, and P_{in} is the input power at the

receiving port. Assuming thermal noise contributions from the enhancement method are negligible, the noise equivalent field with and without enhancement are related by the enhancement factor F such that [94]:

$$F = \frac{\text{NEF}}{\text{NEF}_0} \tag{3.2}$$

where NEF_0 is the free-space noise-equivalent field without enhancement.

3.2 Other Enhancement Methods

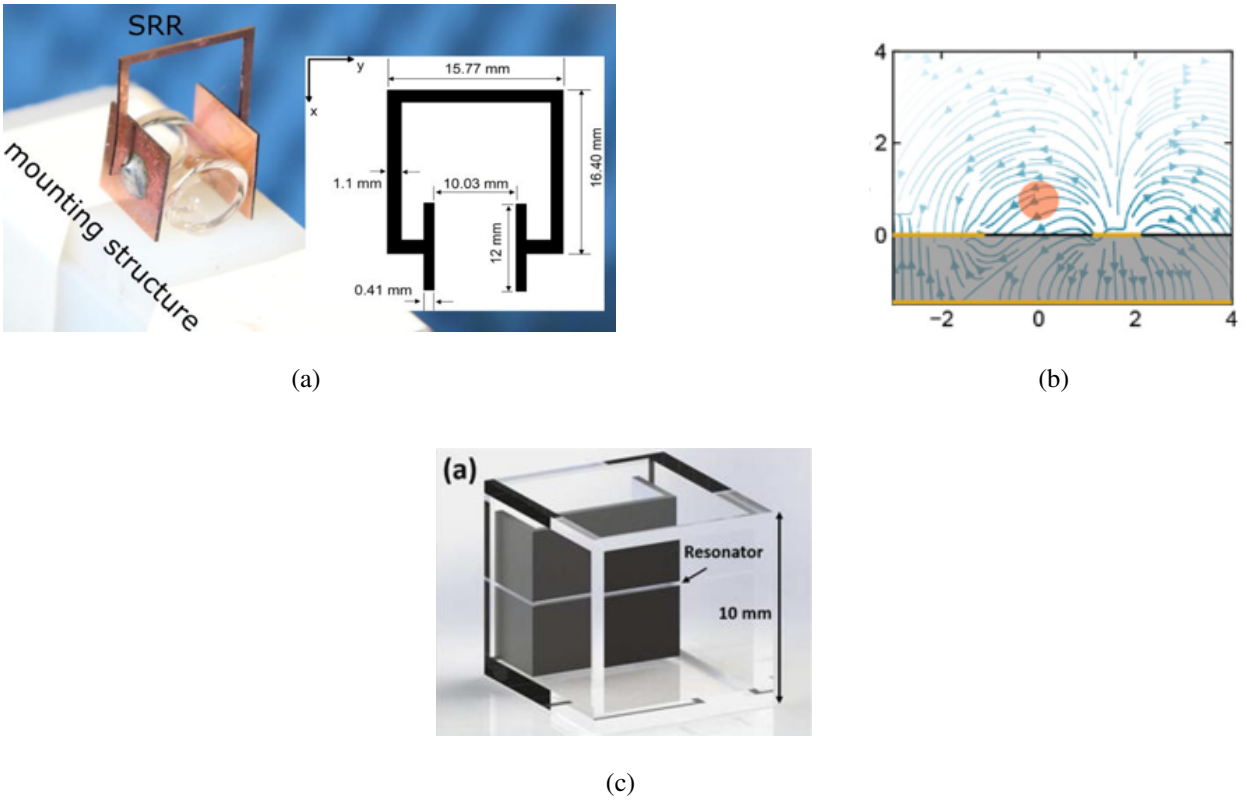


Figure 3.1: Other microwave enhancement methods, including a split ring resonator (a) from [45], close-proximity co-planar waveguide line [74] (b), and parallel plate resonator [3].

A variety of methods have been proposed to enhance the sensitivity of Rydberg receivers, including laser repumping [84], parameter optimization [21], and the introduction of a microwave local oscillator (LO) [54]. While repumping and parameter optimization are optical enhancement methods, sensitivity can also be

improved in the microwave domain using resonant structures based on lumped elements, coupled lines, or cavities. In L-band near 1 GHz, a split-ring resonator achieved a field enhancement factor of $F = 100$ and a sensitivity of 5.5 μV/m/$\sqrt{\text{Hz}}$ [45]. Although effective, this lumped-element approach is best suited to lower frequencies and is difficult to scale to shorter microwave wavelengths. In C-band, a parallel-plate resonator embedded inside a vapor cell demonstrated an enhancement factor of $F = 16.2$ [3], though no NEF value was reported. Another microwave enhancement approach uses the fields above a coplanar waveguide (CPW) transmission line [74], but no enhancement factor or NEF was reported.

Metallic waveguide resonators have been demonstrated for single-frequency enhancement, with reported enhancement factors of $F = 14$ at 15.096 GHz [93] and $F = 14.5$ at 10.22 GHz [92]. These structures are attractive because they can support much higher intrinsic Q-factors than lumped-element resonators. While lumped-element implementations in the GHz range typically have Q-factors of only several tens, metallic waveguide resonators can reach several thousands, enabling enhancement factors greater than $F = 20$. In the dominant mode, the resonator electric field is polarized along a single axis, allowing straightforward co-polarization with the excitation lasers. Metallic resonators are also structurally robust and can be readily fabricated in aluminum using CNC machining. Resonant cavities in copper [108] and niobium [60] have been demonstrated in Rydberg-based systems, although neither study reported the resulting sensitivity enhancement. In a free-space Rydberg setup, a resonant cavity must be connected to a receiving antenna in order to couple incident fields into the structure. In this configuration, the receiver loses the advantage of operating as an electrically small antenna beyond the Chu limit, but retains its high sensitivity and the potential to approach the atom shot noise limit. Some enhancement topologies are shown in Fig. 3.1.

Several parameters must be considered when designing a resonant structure for a Rydberg sensor. During the design process, two factors are especially important: the interaction length L between the atoms and the optical fields, and the coupling coefficient C of the resonator. Previous work suggests that maximizing the interaction volume between the atoms, lasers, and RF field improves resolution, motivating the use of a large interaction length [72]. The coupling coefficient is also important because the optimal coupling regime depends on the free-space sensitivity of the receiver. As shown in [94], highly sensitive systems with free-space sensitivities near 10 μV/m/$\sqrt{\text{Hz}}$ or lower are best enhanced with an overcoupled

cavity, whereas less sensitive systems with free-space sensitivities above 40 μV/m/$\sqrt{\text{Hz}}$ benefit more from critical coupling. When the cavity is overcoupled, thermal noise generated inside it leaks out through the coupling port, effectively radiatively cooling the mode and reducing the thermal noise contribution. However, overcoupling also lowers the cavity's ability to build up and store energy, decreasing intra-cavity enhancement. This creates a fundamental tradeoff between minimizing thermal noise and maintaining strong field enhancement inside the cavity. Since the free-space sensitivity is sensor-dependent, an ideal resonator should be tunable between both coupling regimes. Coupling tunability is achieved by changing the dimensions of the coupling aperture between the input port and the resonator. This can be accomplished in a few ways, e.g. by inserting a dowel or rod through the top of the coupling aperture to change its effective size [93], or by constructing a sliding feed as shown below. The resonator performance is also influenced by the vapor-cell geometry and composition, the rubidium population, and the manufacturing method.

3.3 Waveguide Resonator

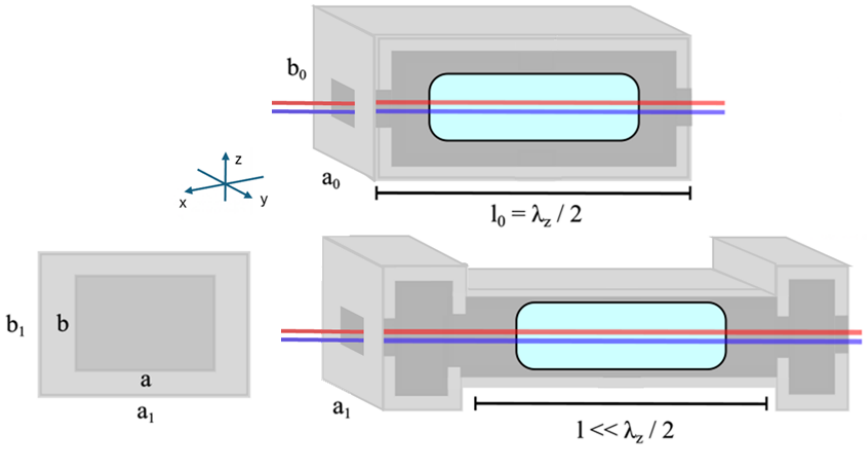


Figure 3.2: (a) A regular $\lambda/2$ length waveguide. The waveguide is fed through an aperture on one side of the waveguide (y-axis), while there are two optical windows on the x-axis to accommodate the probe and coupling lasers. The electric field is pointed along the z-axis. (b) An improved resonant cavity design, where a smaller, electrically shorter but physically longer section of waveguide is placed between two electrically longer larger sections.

The simplest half-wavelength long metal waveguide resonant cavity is a rectangular waveguide, with the atom vapor cell inside the metal enclosure, as shown in Fig. 3.2(a). For the dominant TE_{10} mode, the electric field is in the z direction and co-polarized with the optical fields. While this cavity can provide enhancement through its Q factor, the electric field that the atoms are subjected to inside the vapor cell is strongly non-uniform. In a standard waveguide, the atoms situated in the volume with a stronger field will sense many different field amplitudes, and therefore exhibit many different AT splittings [86]. This effectively broadens each of the two AT splitting peaks, reducing the resolution of the field measurement. This motivates the design of the cavity shown in 3.2(b). A field of higher uniformity is obtained by reducing the physical size of the waveguide to be closer to cut-off of the TE_{10} mode, which results in a long guided wavelength in the x direction, from $\lambda_z = \lambda_0/\sqrt{1-(f/f_c)^2}$, where $f_c = c_0/2a$, and a is the x dimension of the waveguide. To form a full resonator, larger waveguide sections (a_1, b_1) load the smaller waveguide at the two ends. A slot on the longer wall couples the incident external microwave field $\vec{E}_{ext}$ into the cavity, resulting in an enhancement factor which is a function of the loaded Q of the resonator.

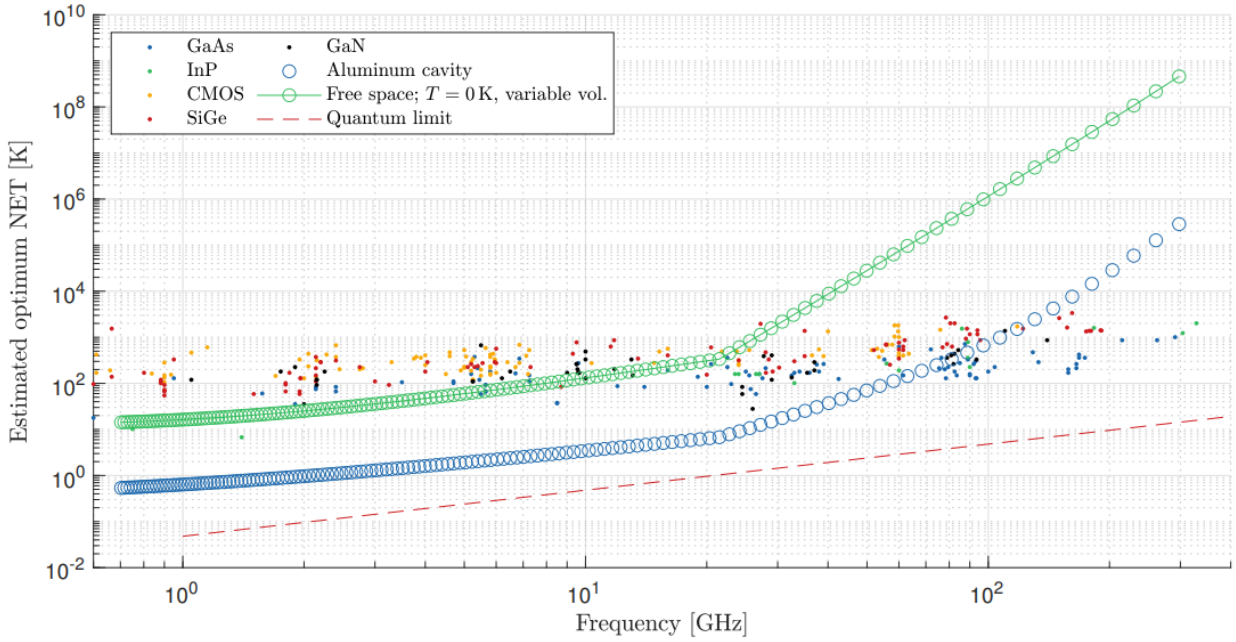


Figure 3.3: Noise temperature versus frequency for a sampling in low-noise amplifiers, manufactured in different technologies. LNA sensitivity tends to decrease with increasing sensitivity, as shown by the plot. [9]. Furthermore, we can see that the sensitivity of a Rydberg-atom receiver can be enhanced through the use of a half-wavelength long resonator, from the formulation shown in [94].

As an example, in a cavity of the design from Fig. 3.2(b), assuming a frequency of 10 GHz and a realistic intrinsic Q-factor of 2000 in a critically-coupled waveguide, an enhancement factor of $F = 39.5$ can be achieved. If this enhancement if applied to the current state-of-the-art Rydberg sensitivity shown in [16], it is reduced from $0.40\,\mu\mathrm{V/m}/\sqrt{\mathrm{Hz}}$ to $0.05\mu\mathrm{V/m}/\sqrt{\mathrm{Hz}}$ when the resonator is optimally overcoupled for radiative cooling [94]. This is equivalent to a noise temperature of 25 K, and is more competitive with conventional receiver noise figures [9]. Fig. 3.3 compares the noise-equivalent temperature as a function of frequency for Rydberg-atom receivers and conventional receivers implemented in several technologies. In free space, Rydberg receivers exhibit promising sensitivity from L-band to C-band. With the introduction of a microwave resonator, following the formulation in [94], this sensitivity threshold is reduced further, suggesting that Rydberg-atom receivers may be competitive with conventional receivers in terms of sensitivity up to Ka-band.

3.4 15 GHz Design - RF Characterization

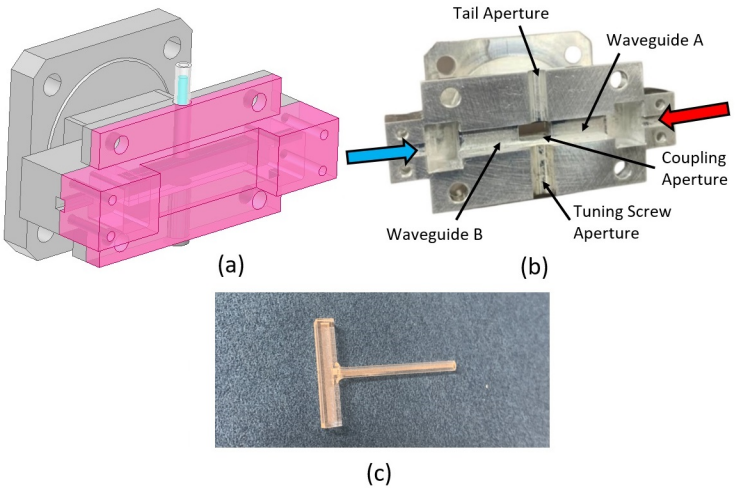


Figure 3.4: (a) 3D view of the field-enhancement 15.096-GHz cavity fed by a WR62 rectangular waveguide. The total volume of the resonator is approximately $20 \times 30 \times 40$ mm. (b) Photograph of one half of the split-block machined structure. In addition to the waveguide sections A and B, additional apertures accommodate the excitation laser beams (shown in blue and red arrows), the filling tube of the vapor cell, and a tuning screw. (c) Photograph of the unfilled fused silica vapor cell.

A resonator design for microwave enhancement at 15.096 GHz is shown in Fig. 3.4(a). The feed is chosen to be a WR62 rectangular waveguide, which is coupled to the resonator through a small aperture for a 15.096 GHz design frequency. The cavity is composed of three rectangular waveguide sections. On either side of the main resonant cavity are two sections of WR62 waveguides $\approx \lambda_g/4$ long, where λ_g is the associated guided wavelength. The central section between them, is 25 mm long with a transverse cross-section of 6.5 mm $\times$ 4.318 mm and operates close to its cutoff frequency where the guided wavelength is large. This makes the resonator electrically short, with high field uniformity. The fused silica ($\epsilon_r = 3.8$, $\tan\delta = 0.00025$ [79]) vapor cell containing Rubidium atoms is fully enclosed by the central resonant cavity with a small aperture cut in the top of the resonator to accommodate the tail left on the cell after Rb filling, seen in Fig. 3.4(c). Laser beam optical windows 2 mm in diameter are manufactured in both sections of outer waveguide. This resonator is designed to resonate at a precise frequency to optimally observe AT splitting;

however, manufacturing tolerances (200 μm) can result in a frequency shift. A hole is therefore added at the bottom of the resonator for a tuning screw, which can mechanically shift the resonant frequency.

The full-wave simulation (Ansys HFSS) of the resonator with the fused silica vapor cell inserted shows a resonance at 15.0960 GHz with $|S_{11}| = -20.7\,\mathrm{dB}$. The cavity is designed to be critically coupled, with $Q_i \approx Q_c \approx 1800$. The simulated field enhancement factor is $F \approx 20.4$, assuming the input is coupled to an electrically small antenna with $G = 3/2$. The tuning screw provides a tuning range of 216 MHz, shown in Fig. 3.5, while the electric field magnitude is given in Fig. 3.6. The electric field should be linearly co-polarized with the optical field, and for this resonator the polarization extinction ratio is better than 30 dB. The coupling factor is designed by varying the length of the aperture between the WR62 feed and central waveguide section by 200 μm from the nominal value of 5.9 mm, keeping the height constant at 3 mm, with resulting simulated reflection coefficient magnitude and phase shown in Fig. 3.7.

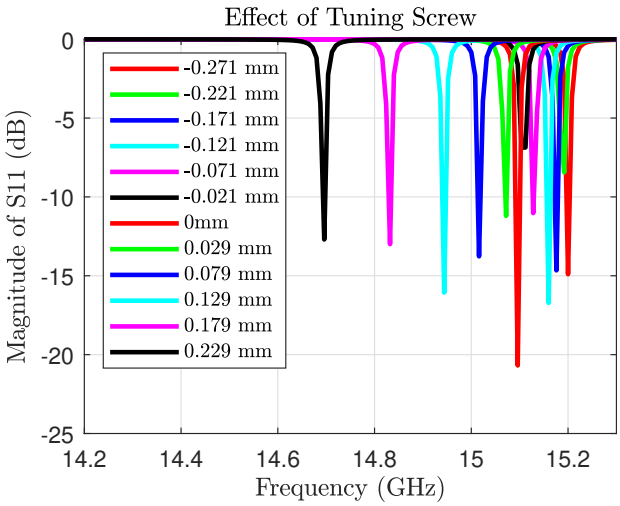


Figure 3.5: Dependence of reflection coefficient at the WR62 waveguide feed on tuning screw displacement from -0.271 mm to $+0.229$ mm relative to the position when it is flush with the waveguide wall. The full tuning range is 216 MHz without significant degradation in Q factor.

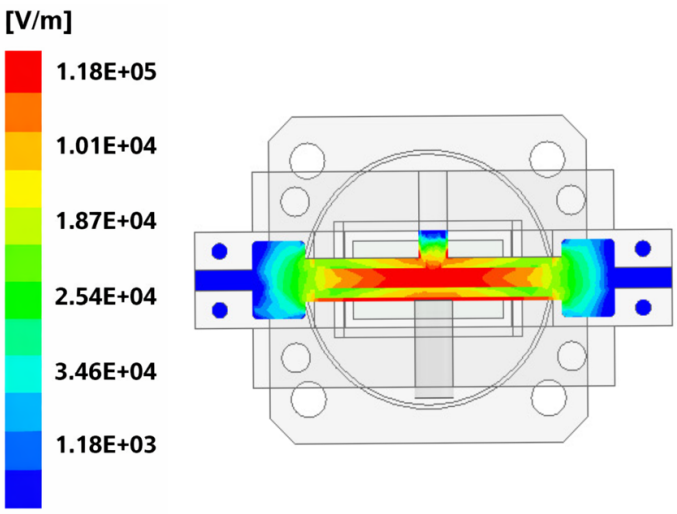


Figure 3.6: The magnitude of the electric field in the resonating cavity. Inside the vapor cell, the maximum E-field is $1.18 \cdot 10^5$ V/m for a 1 W input power at the waveguide feed. The electric field is linearly polarized.

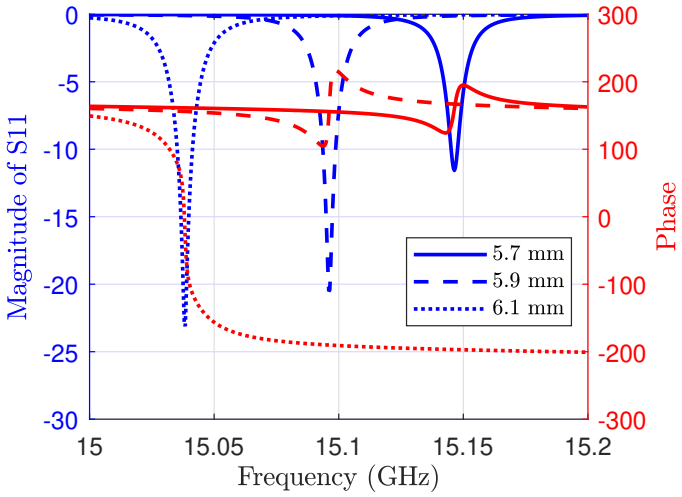


Figure 3.7: Simulated reflection coefficient magnitude and phase vs. frequency for three lengths of a 3-mm tall aperture: nominal length of 5.9 mm $\pm 200\ \mu$m. The mode changes from undercoupled to overcoupled as the aperture increases.

The resonator connected to a 3.5 mm coaxial-to-WR62 waveguide adapter is measured with a PNA with SOLT calibration at the coaxial reference plane (due to the unavailability of WR62 calibration standards). Fig. 3.8 shows the magnitude and phase of the measured reflection coefficient. A resonance is measured at 15.5016 GHz, less than 4% (412 MHz) above the target resonance frequency. Last-minute modifications had

to be done to the cavity to accommodate unexpected features in the fused silica vapor cell, namely a bulge in the region where the filling tube attaches to the cell. The cylindrical channel for the filling tube needed to be enlarged near the cavity wall, creating an air pocket that increases the cutoff frequency of the waveguide, thus making it electrically shorter and shifting the resonance to a higher frequency. As shown in Fig. 3.8, the reflection coefficient near resonance is normalized in magnitude and phase to 0 dB and 0 °, respectively, and fitted with the theoretical reflection coefficient of a single-mode resonator with intrinsic (unloaded) and coupling (external) quality factors Q_i and Q_c, respectively [93]:

$$S_{11} = \frac{\frac{Q_c - Q_i}{Q_c + Q_i} + j\frac{2Q_cQ_i}{Q_c+Q_i}\left(\frac{f-f_0}{f_0}\right)}{1 + j\frac{2Q_cQ_i}{Q_c+Q_i}\left(\frac{f-f_0}{f_0}\right)}. \tag{3.3}$$

From the fitting, we estimate $Q_i \approx 1100$ and $Q_c \approx 2860$. We attribute the strongly undercoupled behavior of the cavity to extra losses arising from the drilling modifications.

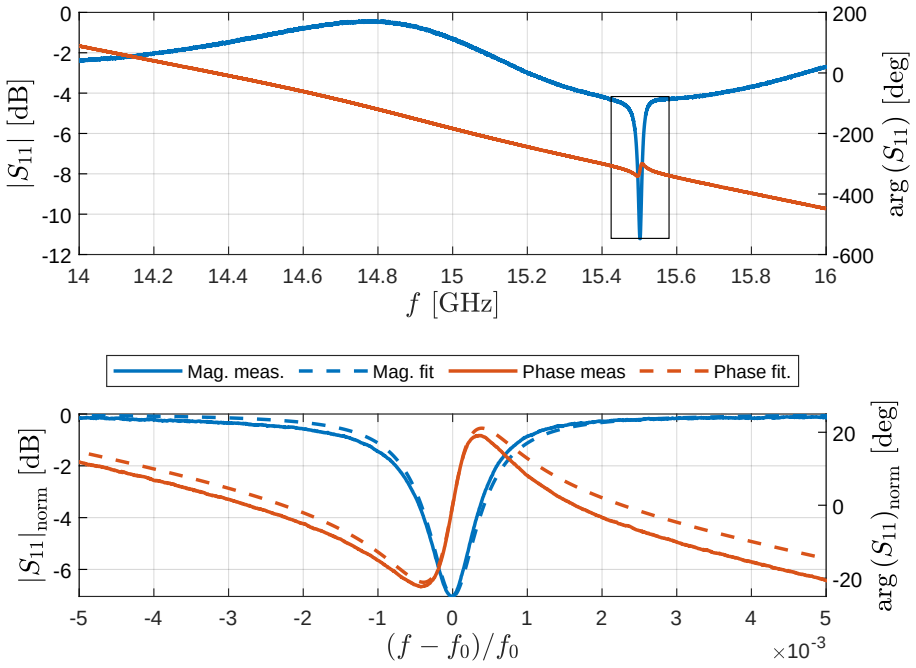


Figure 3.8: (Top) Magnitude and phase of measured reflection coefficient showing a resonance at 15.5016 GHz. (Bottom) Inset of the resonance shown in the top figure, and theoretical fit (dashed) curves.

As shown in [**?**], a field-enhancing port-fed cavity exhibits an input-referred noise temperature T_e given by:

$$T_e = \frac{hf}{k_B} + \frac{Q_c}{Q_i}\left(2T_p + \frac{hf}{k_B}\right) + \frac{\mathrm{NEF}_0^2}{k_B F^2 \Lambda^2}, \tag{3.4}$$

where Q_i and Q_c are the intrinsic and coupling quality factors of the resonator, respectively, T_p is the physical temperature of the resonator, h is the Planck constant, f is the receiver frequency, and

$$\Lambda^2 = \frac{8\pi f^2}{\varepsilon_0 c_0^3 G}, \tag{3.5}$$

where ε_0 is the vacuum permittivity, c_0 the speed of light and G the antenna gain used to calculate F. F is a function of Q_i and Q_c, and decreases for the case where Q_c/Q_i is less than one, producing the noise-enhancement trade-off noted in the previous chapter. Additionally, we assume there are no temperature contributions from the antenna.

Using the experimentally measured Q_i along with Eq. (3.4), the noise temperature of an atomic receiver enhanced with the manufactured cavity is estimated in Fig. 3.9 as a function of the intrinsic (not-enhanced) atomic sensitivity NEF_0. The noise temperature results are compared to the best reported noise temperature of an LNA in the $14\,\mathrm{GHz}$ to $16\,\mathrm{GHz}$ range, $T_{\mathrm{LNA}} \approx 83.6\,\mathrm{K}$ [25, 9]. For each case, the results are also compared with the equivalent noise temperature of the atomic receiver without the enhancement cavity. The cavity-enhanced atomic receiver is competitive to LNAs for intrinsic sensitivity values better than $\mathrm{NEF}_0 \sim 1\,\mu\mathrm{V\,m^{-1}\,Hz^{-1/2}}$. In this case, the minimum noise temperature $T_e \approx 110\,\mathrm{K}$ is achieved for a significantly overcoupled cavity where $Q_i/Q_c \approx 13.8$. Note that without the cavity, the atomic receiver exhibits a noise temperature $T_e \approx 4160\,\mathrm{K}$. Therefore, despite exhibiting half of the the designed intrinsic Q, the manufactured cavity can significantly improve the noise performance of a non-enhanced Rydberg receiver. This would require enlarging the coupling aperture so that the undercoupled mode becomes overcoupled.

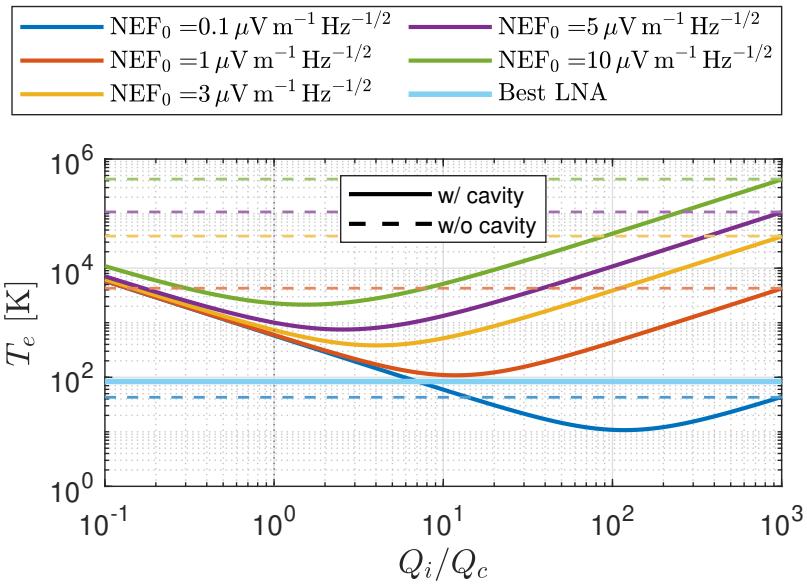


Figure 3.9: Estimated noise temperature of manufactured cavity as a function of the coupling strength, for different NEF_0 values.

This design was ultimately not integrated into a Rydberg receiver because the vapor cell was not able to be successfully filled with a significant atomic population of rubidium. However, this work still demonstrates significant results in the regime of sensitivity enhancement for Rydberg receivers. This chapter shows the design and characterization of a Ku-band metallic waveguide cavity with an internal fused silica vapor cell for sensitivity enhancement of a room-temperature Rydberg atom electric field sensor, designed for a Rubidium $52\mathrm{D}_{5/2}$ transition. The resonator is designed to have a high field uniformity for a linearly-polarized mode, and is tunable to account for manufacturing tolerances. Post-manufacturing modifications to the microwave cavity had to be done to accommodate unexpected geometric features of the vapor cell, degrading the intrinsic Q, and reducing the field enhancement factor from 20 to 14. Despite this, the cavity can provide more than one order of magnitude of sensitivity improvement with respect to non-enhanced atomic sensors.

3.5 10.22 GHz - RF Characterization

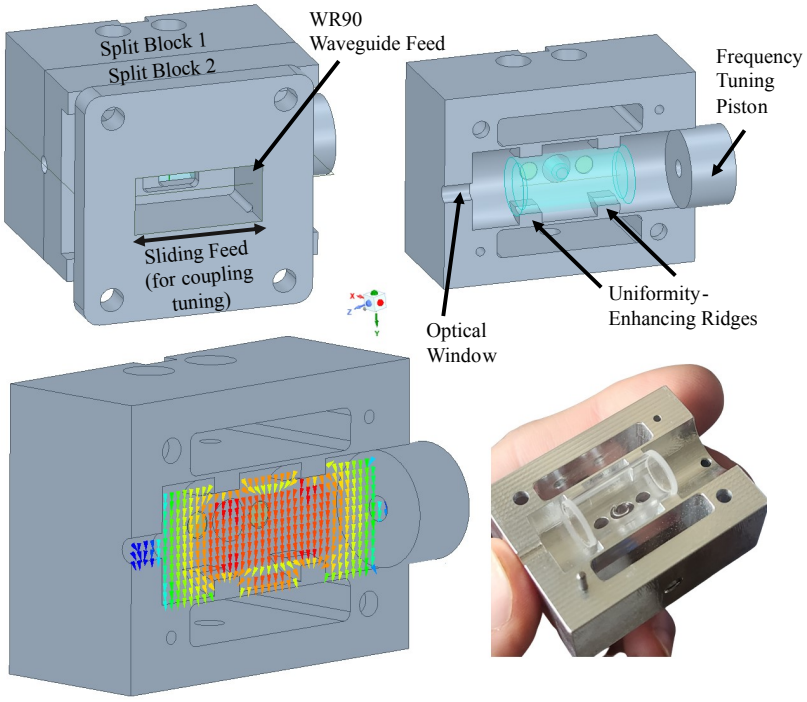


Figure 3.10: The geometry of our resonant cavity. This resonator was machined in two parts, and is therefore composed of two split blocks. Designed for a 10.22 GHz transition, it is fed with a WR90 waveguide. The coupling between this resonator and the waveguide can be modified using a sliding feed, which changes the effective aperture size. The vapor cell sits inside the resonant cavity, where it can be tuned using a frequency tuning piston.

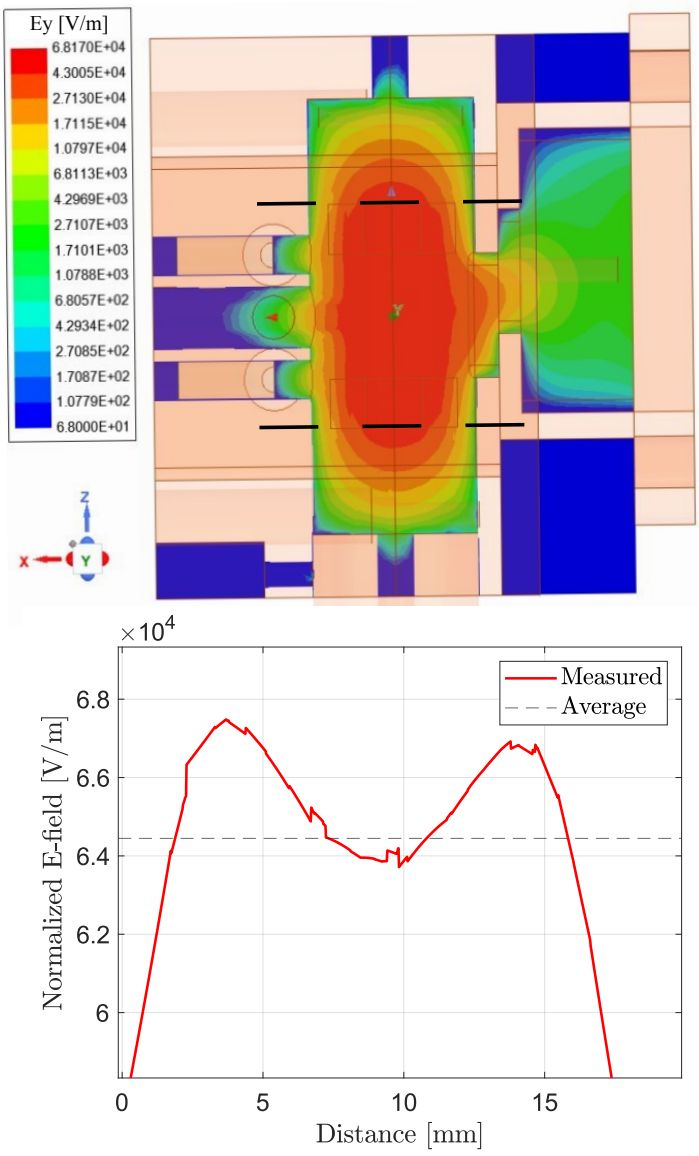


Figure 3.11: The fields along the z-direction of the resonator, with the same polarization as the linearly polarized laser (y-direction). There is a high degree of uniformity in this waveguide compared to a standard $\lambda/2$ waveguide, varying between $5.8 \times 10^4\,\mathrm{V/m}$ and $6.75 \times 10^4\,\mathrm{V/m}$ with an average value of $6.44 \times 10^4\,\mathrm{V/m}$ for a 1 W input power.

This cavity is designed for the $59\mathrm{P}_{1/2}$ energy transition, corresponding to a 10.22 GHz frequency. Inside the cavity is a $20\,\mathrm{mm}$ long and $10\,\mathrm{mm}$ diameter vapor cell filled with Rubidium 87 and manufactured by Precision Glassblowing. The cavity has both frequency tuning and coupling tuning mechanisms; the coupling is controlled by a sliding feed that changes the coupling aperture size. Frequency tuning is done

using a two large copper rods that are inserted in the y-direction, and allows for 150 MHz of tuning. Additionally, there is a frequency tuning piston that translates in the z-direction, and provides an additional 83 MHz of tunability. Overall the dimensions of the cavity are 35 mm x 40 mm x 45 mm, excluding the feed, and is made of aluminum 6061. The overall geometry of the cavity can be seen in Figure 3.10. The split-block cut was not aligned with the E-plane of the mode in order to accommodate the sliding feed design.

In simulation, the cavity shows a slightly overcoupled resonance at 10.2195 GHz, with an $S_{11} = -11.96\,\mathrm{dB}$, when properly tuned. The intrinsic and coupling quality factors are $Q_i = 2657$ and $Q_c = 1690$, respectively. Sweeping the displacement of the frequency tuning piston from 2 mm into the cavity to 4 mm out of the cavity, the resonant frequency can be tuned from 10.28 GHz to 10.20 GHz, for a total accessible range of 80 MHz. Similarly, when the coupling tuner is swept from 0 mm displacement (perfectly aligned) to 5 mm offset, the cavity resonates within all three types of coupling. Namely, a displacement of 5 mm is undercoupled, while 0 is overcoupled, with a critically coupled regime in the transition between the two.

The cavity is designed for a high level of electric field uniformity, which is shown in the simulation of Fig. 3.11 when feeding with $1\,\mathrm{W}$ at the input. The volume where the cell is located is significantly shorter than the guided wavelength, despite the physical length being 68% of the free-space wavelength. However, the field decay at the edges of the cell is compensated by adding narrow ridges, thus improving uniformity. Overall, the field varies most between such ridges and the edges of the cell, where the complex magnitude of the electric field in the y direction, $\vec{E}_y$, varies between $5.8 \cdot 10^4$ V/m and $6.75 \cdot 10^4$ V/m with an average value of $6.44 \cdot 10^4$ V/m, for an input power of 1 W.

This results in a field standing wave ratio of $\mathrm{SWR} = 1.16$. Uniformity is most desirable in the y-direction because it is co-polarized with the excitation lasers. Initial tests with the resonator and vapor cell yielded no resonance. The cavity was then tested without the cell to troubleshoot the error and it was found that measured results matched expectations, though with a slightly degraded intrinsic $Q_i \approx 2230$ against the simulated one without the cell $Q_i \approx 2900$. Manufacturing defects and gaps arising from the split-block machining process are potential contributions towards decreasing Q-factor between simulated and measured results. It was determined that some of the Rubidium within the cell had condensed, so the

microwave properties of the vapor cell were not as anticipated. Heaters were the attached to the cavity to vaporize the condensed Rubidium, and measurements recorded with a vector network analyzer (VNA) in several multiple-hour increments.

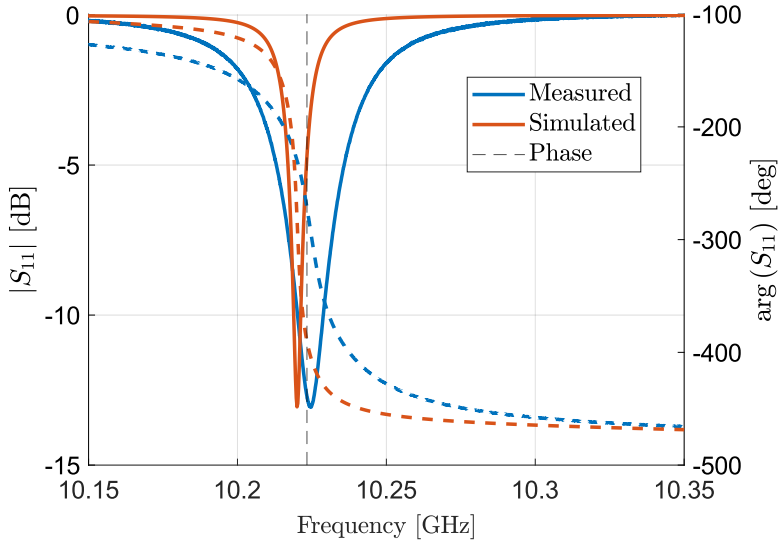


Figure 3.12: Comparison of the measured and simulated resonator properties. In order to observe resonance, heaters are applied to the cavity with the cell inserted and VNA measurements are performed for several hours while the heat was applied. The measured resonance is at 10.2246 GHz, or within 0.045% of the target frequency.

The cavity exhibits resonance at 10.22 GHz in simulation, and 10.2246 GHz in measurement, which are both shown in Fig. 3.12. The data from these simulations is fit using the following expression [94]:

$$\Gamma_{in} = e^{-\alpha} e^{i\phi} e^{-i\delta\omega(\tau_w + k_{\text{disp}}\delta\omega)} \left(\frac{a e^{-i\delta\omega\tau} - |r|}{1 - |r| a e^{-i\delta\omega\tau}} \right), \tag{3.6}$$

where α is the input waveguide loss, ϕ is an arbitrary reference phase, $\delta\omega = \omega - \omega_0$, where ω_0 is the resonance frequency, τ_w is the input waveguide delay, k_{disp} is the input waveguide dispersion factor, a is the cavity roundtrip loss, τ is the cavity roundtrip time, and $|r|$ is the coupler reflection coefficient. The intrinsic and coupling quality factors are then obtained as $Q_i = \exp\left(\omega_0\tau / \ln a^2\right)$ and $Q_c = \exp\left(\omega_0\tau / \ln |r|^2\right)$, respectively. Compared to Eq. 3.3, the expression shown in Eq. 3.6 fits to the VNA-based measurement

results, which include features such as loss and delay. From this fitting equation, we observe degradation of the intrinsic Q-factor (Q_i) of the resonator from the expected value of $Q_i = 2657$ to $Q_i \approx 700$. This is attributed to the Rubidium vapor even after heating over several hours. To confirm, we also tested an empty fused silica vapor cell with no intrinsic Q degradation shown. Previous literature suggests that Rubidium is lossless in the microwave domain [74], though these experiments were not performed with resonant methods and therefore are potentially less sensitive.

Q-factor measurements are recorded over a thirty-hour time period, along with the temperature of the two heaters applied to either side of the resonant cavity. It was observed that the intrinsic Q-factor improves from virtually 0 to ≈ 600 over the full measurement duration as shown in Fig. 3.13. Ultimately, the maximum intrinsic Q-factor achieved was ≈ 700, after several days of continuous heating. The frequency and the coupling tuners of the cavity resonator are tested by calibrating a vector network analyzer (VNA) to the plane of a WR90 waveguide adapter. The cavity is heated for a few hours before this experiment and the heater is off while the measurements are taken. This degrades the intrinsic Q to about ≈ 180, not relevant for the frequency and coupling tuning characterization.

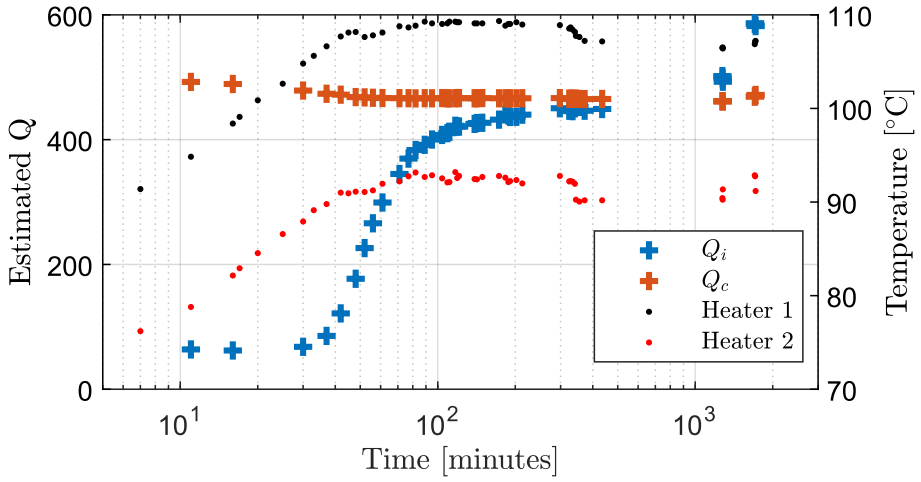


Figure 3.13: The effect of heating the resonator over a 30-hour time period. There was some asymmetry in heating the two thermistors as a result of the limits of the control panels. For the time interval of 400 to 1300 minutes, data was not recorded as the experiment was left running overnight. Ultimately, the Q-factor improved from 0 (no resonance) to $\approx$ 600 over the full time period.

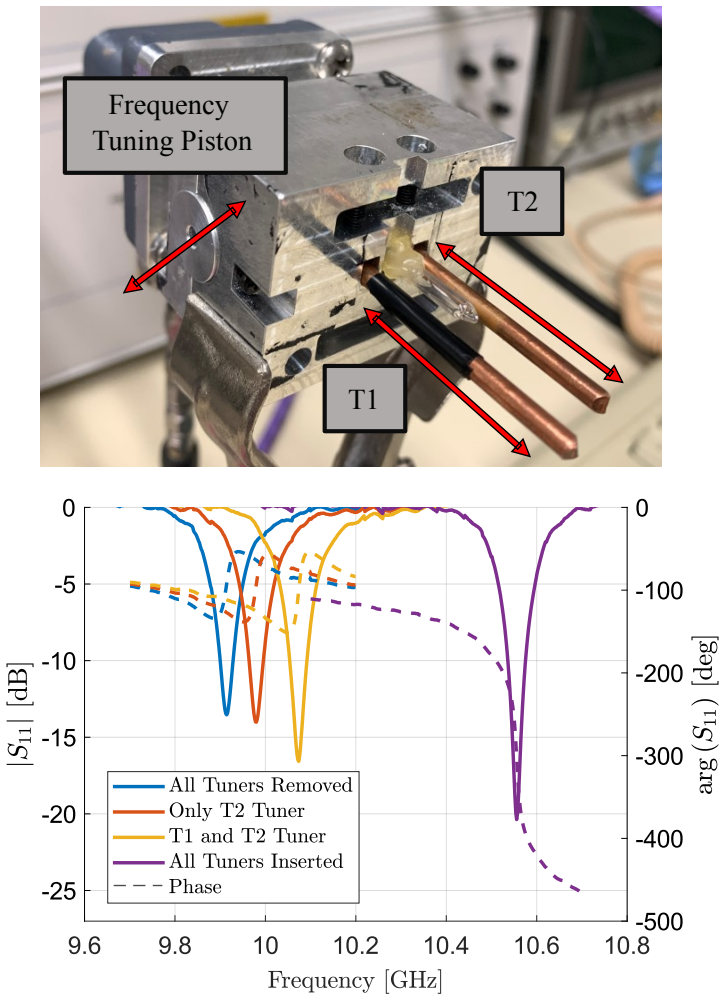


Figure 3.14: The measured frequency tuning for three configurations of the resonator: with one tuning rod T1, tuning rod T2, and the frequency tuning piston. All frequencies between the all-removed and all-inserted configurations are accessible.

The two copper tuning rods, T1 and T2, are displaced in one millimeter increments and the change in resonance is recorded. These results can be seen in Fig. 3.14. With neither the tuners nor the piston inserted, the cavity resonates at 9.91 GHz, which can be tuned up to 9.98 GHz with a single copper rod (T2) fully inserted. Thus, T2 provides 66 MHz of tuning. With maximal insertion of the second copper rod (T1), resonance can be tuned an additional 90 MHz to 10.07 GHz. Lastly, the tuning piston is tested, and it significantly shifts the resonant frequency of the cavity, up to 10.56 GHz when fully inset. Overall, the three tuning mechanisms enable the resonator to target transitions from 9.91 GHz to 10.56 GHz, or a 650 MHz

tuning range. These results are shown in Fig. 3.14.

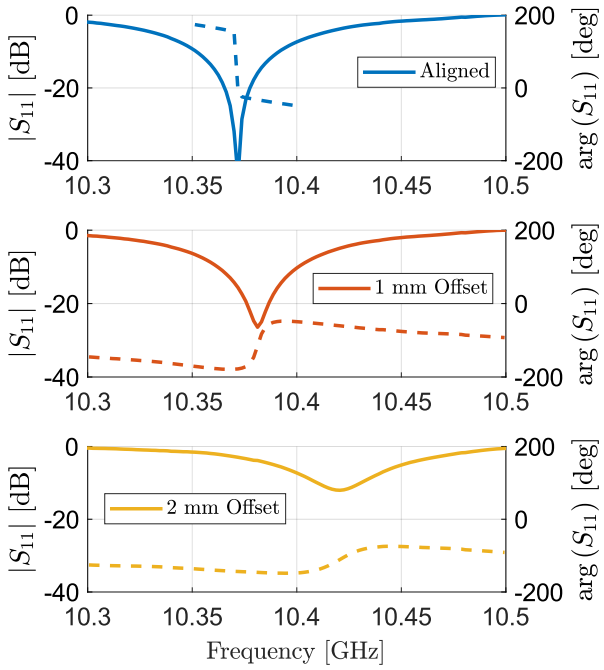


Figure 3.15: Measurements of resonator reflection coefficient magnitude and phase based on three sliding feed positions, and the frequency tuners at maximal insertion. The first measurement corresponds to the apertures completely aligned, and therefore maximal transmission. The second and third plots are with the feed slid one and two millimeters, respectively.

The feed in the waveguide can slide to change the effective size of the aperture connecting the resonant cavity to a WR90 adapter. Modifying the aperture size impacts the coupling into the cavity, thus changing the properties of the resonance. As changing the type of coupling used in the resonator is integral to its function in a Rydberg receiver, the position of the sliding feed was swept and the resulting resonant magnitude and phase was recorded, as shown in Fig. 3.15. Three configurations were tested: with the apertures perfectly overlapped, and with displacement one and two millimeters sideways. The maximally-aligned configuration exhibited an intrinsic Q-factor of 174 and an coupling Q-factor of 176. Similarly, in the one millimeter offset measurement, $Q_i = 185$ and $Q_c = 196$. In the last measurement, the two millimeter offset, $Q_i = 177$ and $Q_c = 286$. This trend is as expected; the intrinsic Q does not change with the tuner, but the coupling

Q does change, indicating that the coupling coefficient $C = Q_i/Q_c$ is tunable within this resonator. The coupling Q can be tuned all the way up to $Q_c \to \infty$ by sliding the feed until the aperture is closed. Fig. 3.15 also indicates the change in phase as a result of this coupling coefficient, transitioning from overcoupled to undercoupled regimes between the maximally aligned and 1 mm offset measurements.

3.6 10.22 GHz - Optical Measurements

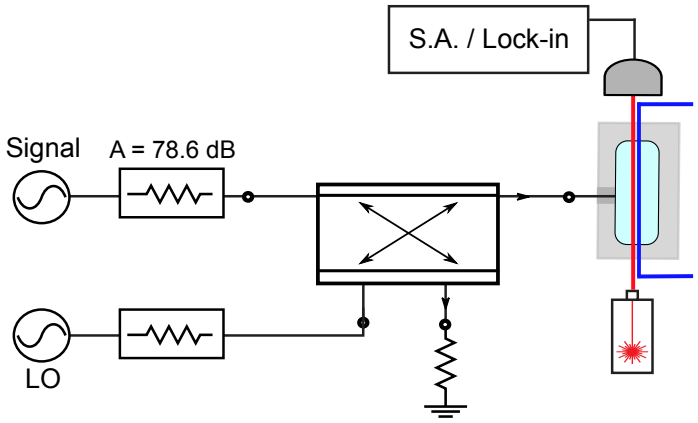


Figure 3.16: The experimental set-up used for measuring the sensitivity of the Rydberg receiver with cavity enhancement. From this topology, the AT splitting is measured, and then used to calculate the minimum detectable field at the input of the resonator. The coupler is a 20 dB coupler.

The sensitivity of the enhanced Rydberg receiver is characterized experimentally using the configuration shown in Fig. 3.16. A signal generator provides the microwave field that we want to detect, while a local oscillator provides a signal for mixing, and therefore heterodyning. Attenuators are used to bring the noise floor of the signal generator and LO to thermal background level, at the expense of the desired tones. The two signals are added in the 20-dB coupler, which maximizes the transmission power of the signal and minimizes the thermal contributions from the LO.

After the two signals are added in the coupler, they are transmitted to the feed of the resonant cavity, where the LO polarizes the Rydberg atoms to an AT splitting level. The signal modulates the transmitted probe light on a 10 kHz intermediate frequency beat note. In analysis, we purposely added 76.8 dB of

attenuation to both ensure that the signal is limited by the 300K background thermal radiation and to avoid any nonlinearities (e.g. harmonic distortion) in the signal source.

Probe (780 nm) and Coupling (480 nm) light waves are produced by a Toptica DL pro and Toptica TA SHG pro lasers, respectively, and are frequency stabilized to a >1000 finesse Stable Laser Systems optical reference cavity using the Pound-Drever-Hall method. A sideband and modulation is generated on the lock beam through an EOM, allowing the lasers to be locked at arbitrary detuning from the optical cavity resonance. The probe laser is stabilized to the rubidium-87 D2, F=2 to F'=3 transition. The coupling laser is locked resonant to the $5P_{3/2}$ to $59D_{5/2}$ transition. The probe and coupling light are combined and split on dichroic mirrors, and counter-propagated through the RF cavity and cell. Each beam waist diameter is approximately 1 mm, and the probe and coupling powers incident on the cell and cavity assembly are approximately 50 μW and 25 mW, respectively. The probe beam is incident on one detector of a Thorlabs PDB210A balanced photodetector while the other is unused, and the output is connected to a spectrum analyzer.

The optical and RF local oscillator field powers are optimized to maximize the intermediate frequency signal observed on the signal analyzer. The microwave power at the input port of the cavity is calibrated with a power meter. The intra-cavity electric field is calibrated using Autler Townes splitting of the $59D_{5/2}$ Rydberg state as shown in Fig. 3.18. Interestingly, the measured intra-cavity field magnitude is 10% higher than expected from the simulations, after correcting for the measured degraded quality factor. The reason of the discrepancy is unknown, but could be attributed to an overestimated loss in the power calibration (by $0.6\,\mathrm{dB}$), the non-uniformity of the intra-cavity electric field, variations in the Q of the cavity between RF and optical measurement campaigns, or a combination of these factors.

The intermediate frequency power measured by the spectrum analyzer set to $1\,\mathrm{Hz}$ resolution bandwidth is recorded as a function of power output from the signal RF source as shown in Fig. 3.17. The spectrum analyzer is set to conduct a 100 Hz sweep with a resolution and video bandwidths of RBW = VBW = 1 Hz, centered at the IF frequency. Multiple traces are averaged, which effectively reduces the VBW/RBW ratio well below 1, recommended for noise measurements. The spectrum analyzer uses a Gaussian filter with a power-equivalent bandwidth that is 1.06 times the 3-dB RBW, which results in a small improvement in the

noise floor of only 0.2 dB/Hz and gives a conservative estimate of the sensitivity.

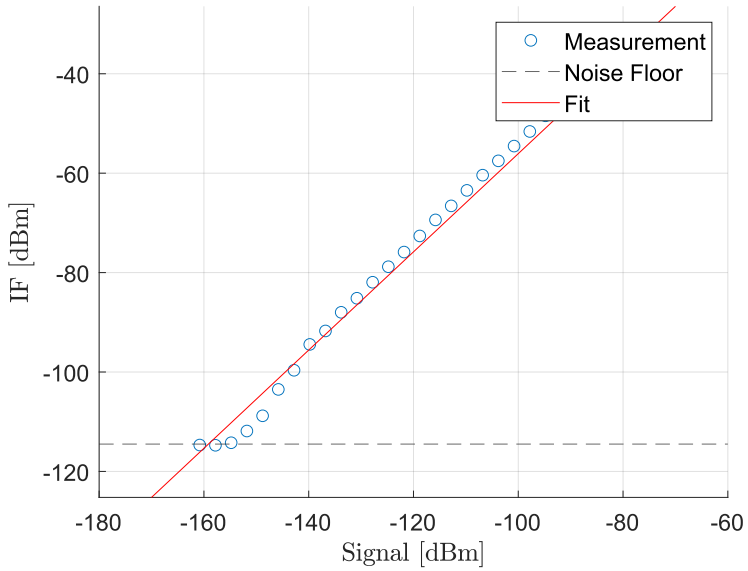


Figure 3.17: Intermediate frequency power as a function of signal power at the plane of the cavity port. Measurements are recorded with 1 Hz resolution bandwidth on the spectrum analyzer. The two values should be directly correlated, as maintained in this measurement for a majority of the data collection interval.

A drift occurred during the experiment while data was collected at $< -60\,\mathrm{dBm}$ signal generator power ($< -136.8\,\mathrm{dBm}$ at the cavity port), likely from a laser unlocking and varying by a few MHz. This unlock can lead to slight signal degradation, and yielded results that were less sensitive than expected. Ultimately, the lowest signal generator power that can be resolved is $-78\,\mathrm{dBm}$ even though from the linear fit it should have intersected the noise floor at $-82.8\,\mathrm{dBm}$. After accounting for 76.8 dB path loss measured from a power calibration of the link, we observe an input-referred receiver noise floor of $-154.8\,\mathrm{dBm/Hz}$, corresponding to a receiver temperature of $\mathrm{NET} \approx 23983\,\mathrm{K}$. From the AT calibration performed, this value corresponds to an intra-cavity field sensitivity of $\mathrm{NEF}_0 \approx 23\,\mu\mathrm{V/m}/\sqrt{\mathrm{Hz}}$, and an external field sensitivity of $\mathrm{NEF} \approx 1.58\,\mu\mathrm{V/m}/\sqrt{\mathrm{Hz}}$ when connected to a $G = 3/2$ antenna. To find the sensitivity of the Rydberg receiver, we calibrate with a known power at the port and measure the absolute field that the atoms sense via AT calibration. Then, for the minimum measurable input power, we solve for the minimum intra-cavity

field, as shown in Fig. 3.17. Additionally, using the antenna theorem, we can calculate the minimum value of external E-field that would be measurable if the cavity was connected to an antenna with a gain of 1.5, which is chosen as a conservative value.

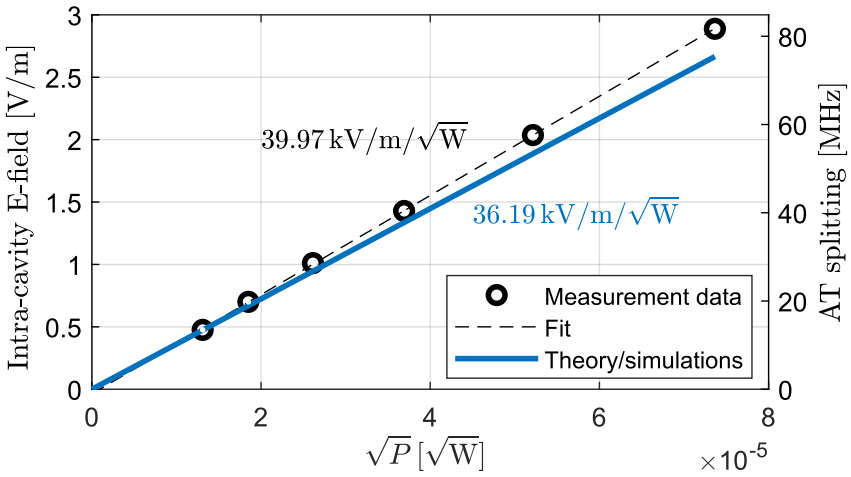


Figure 3.18: Intra-cavity electric field measured via AT splitting as a function of the square root of the power at the input port of the resonator.

The $\mathrm{NEF}_0 = 23\,\mu\mathrm{V/m}/\sqrt{\mathrm{Hz}}$ measured represents the minimum field spectral density resolvable by the atoms. This is the sensitivity the vapor cell would exhibit in a free-space setup, with no field enhancement. This value is approximately an order of magnitude higher than the one measured with the same optical setup but using a Thorlabs reference cell with similar interaction length, where $\mathrm{NEF}_0 \approx 2\,\mu\mathrm{V/m}/\sqrt{\mathrm{Hz}}$ could be measured. Had this NEF_0 been achieved with the Precision Glassblowing vapor cells, and the resonator been tuned for optimal coupling, the optimal sensitivity would have been $\mathrm{NEF} \approx 0.21\,\mu\mathrm{V/m}/\sqrt{\mathrm{Hz}}$, and therefore a new state-of-the-art sensitivity for Rydberg electrometers (see Fig. 3.19). Due to the poor NEF_0 value, the thermal contributions from the resonant cavity are less influential on the overall sensitivity, indicating that the ideal coupling of this cavity is critically coupled. Conducting these measurements also allowed for additional comparison between conventional and Rydberg receivers; we found that had this topology shown a sensitivity of $\mathrm{NEF}_0 = 0.4\mu\mathrm{V/m}/\sqrt{\mathrm{Hz}}$, a reasonable sensitivity threshold, then an overcoupled resonant cavity would have allowed the Rydberg receiver sensitivity to be

competitive with the LNAs used in conventional receivers.

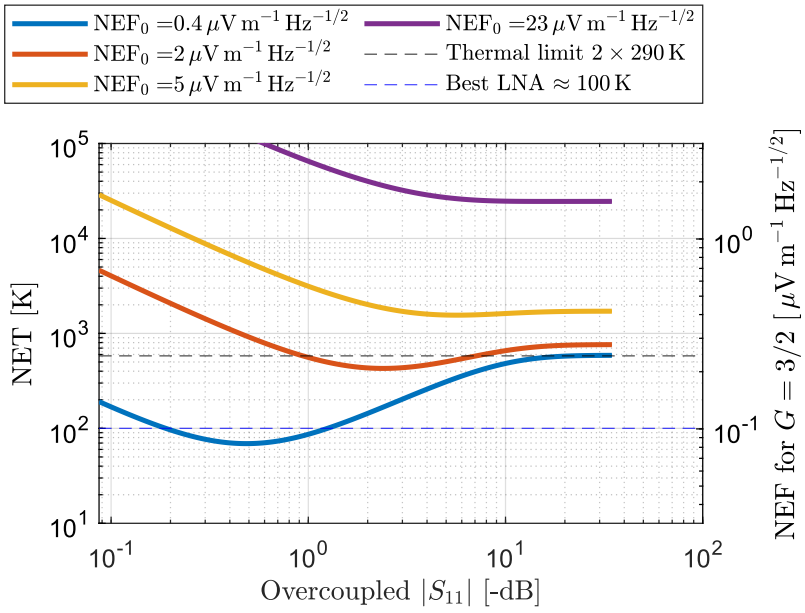


Figure 3.19: The realizable NEF (and equivalent NET) for a given NEF$_0$ and resonant cavity coupling coefficient. At higher NEF$_0$ thresholds, a resonant cavity provides the most enhacement when critically coupled. With a lower sensitivity free-space noise equivalent field, an overcoupled cavity gives the best sensitivity.

The experimental demonstration in this section demonstrates the concept using a metallic resonant microwave cavity at 10.22 GHz. Simulated and measured microwave performance of the resonant cavity enclosing a Rubidium-filled vapor cell are presented, and its potential for enhancement in a larger Rydberg receiver topology demonstrated. In simulation, the resonator shows 233 MHz of frequency tunability with the use of two copper dowels and an aluminum piston. It also shows coupling tunability, allowing the resonator to have over-, critically, and under-coupled operation. The theoretical Q factors of the cavity are $Q_i = 2657$ and $Q_c = 1690$. Experimental values were also recorded, after it was determined that Rubidium vapor within the vapor cell had condensed and required heating. Following characterization with a VNA, the waveguide cavity resonates at 10.2246 GHz with an intrinsic Q-factor $Q_i \approx 700$. We attribute this degradation to the Rubidium within the cell, as previous trials of empty vapor cells in enhancement cavities

showed no significant Q_i degradation. Using both methods of frequency tuning, the cavity demonstrated 650 MHz of tunability, and coupling tuning with access to all three resonance regimes.

The equivalent no-enhancement field sensitivity resulted $\text{NEF}_0 = 23\,\mu\text{V/m}/\sqrt{\text{Hz}}$ as obtained from AT splitting calibrations. This was a relatively high threshold, which indicated that the optimal coupling presented by the resonator is critically coupled. The minimum detectable spectral density was directly measured, corresponding to an input-referred noise figure of 19.23 dB. If an antenna with $G = 3/2$ was connected to the cavity, the noise equivalent field for the cavity-enhanced receiver is $\text{NEF} = 1.58\,\mu\text{V/m}/\sqrt{\text{Hz}}$. This represents more than 23 dB improvement in noise figure of the receiver.

The results from this chapter are reported in [93], [90] and [92].

Chapter 4

Frequency-Tunable X-band Sensitivity-Enhanced Rydberg Receiver

Microwave enhancement that targets a single energy transition is useful for RF applications that are single-frequency or very narrowband. However, a large variety of applications are wide-band or dual-band in operation, necessitating some form of microwave enhancement that can function at multiple frequencies. This chapter will give details on the design, RF characterization, and receiver-integrated performance of a frequency-tunable resonant cavity designed for Rydberg states between 10.16 and 11.26 GHz. This section will also discuss the impact of vapor cell sampling location on Rydberg receiver measurements.

4.1 Resonator RF Characterization

The sensitivity-enhancing resonator is designed for Rydberg states at $59D_{5/2}$ (10.22 GHz) and $58D_{5/2}$ (10.77 GHz) along the P→D transition line. These transitions are chosen because resonator enhancement is most applicable at longer wavelengths (Ku-band and lower). Additionally, there are a large number of available conventional receivers that can be used for a sensitivity comparison [**?**]. There is also interest in using Rydberg atoms in quantum computers at X-band [102] [89].

There are three central components to this resonator design. First, the central resonant cavity which houses the Rubidium-filled vapor cell. This cell is manufactured by Precision Glassblowing in fused silica. The dimensions of the central waveguide section are $33 \times 11 \times 6$ mm and designed to house a 20 mm long and 5 mm diameter vapor cell. The waveguide segments on either side of the central resonator can be displaced using plungers that can be depressed from $d_{min} = 0$ mm up to $d_{max} = 8$ mm in order to change the interior volume of the resonator and tune the frequency. This topology yields a tuning range of

10.15–10.77 GHz for a total resonator length L varied from $L_{min} = 8.3\,\text{cm}$ to $L_{max} = 9.9\,\text{cm}$. Optical windows in the sliding outer sections allow for laser light to enter the cavity and interact with the atoms in the vapor cell, as shown in Fig. 4.1.

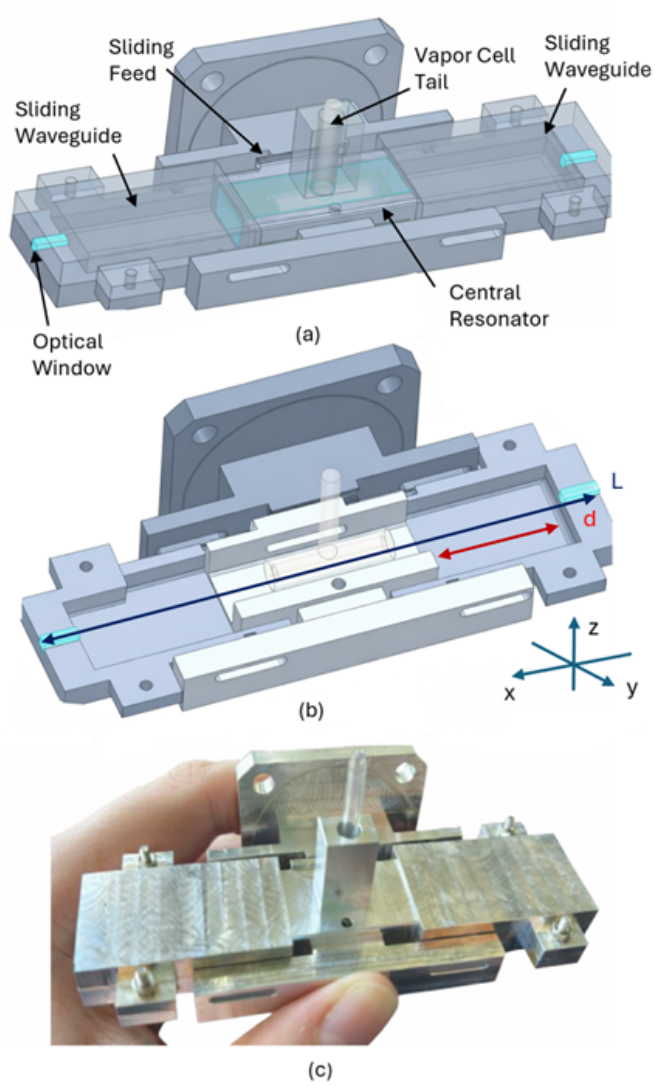
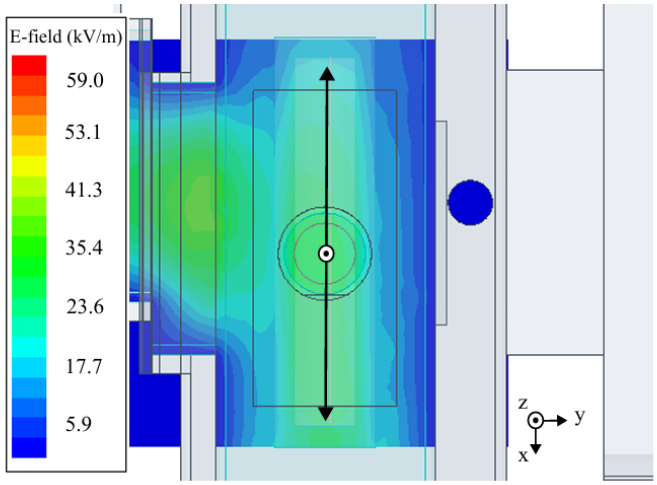
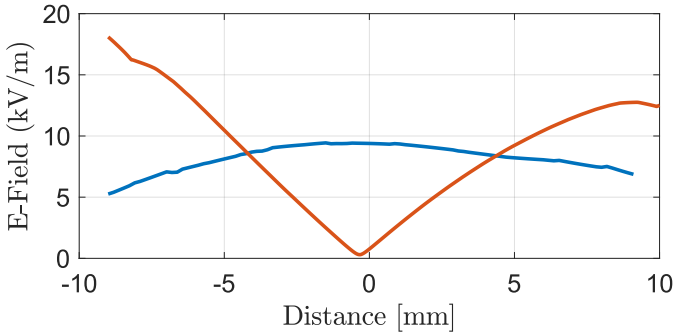


Figure 4.1: (a) A full render in Ansys HFSS of the resonator. The center section contains the vapor cell, while the sliding waveguide components on either side can be displaced to tune the resonant frequency. (b) A cut-away of the resonator, so that the interior can be seen. (c) The resonant cavity in aluminum after CNC machining. For fabrication purposes, it is split into seven pieces and assembled with screws.



(a)



(b)

Figure 4.2: (a) Simulated magnitude of the z-directed electric field vector component at 10.22 GHz, plotted across the interaction length x of the vapor cell. (b) the magnitude of the electric field in the z-direction on a cross-section along the x direction. The values are normalized to a 1 W incident power at the waveguide port.

The WR90 feed has dimensions 22.86 mm$\times$ 10.16 mm, and is connected to the main resonator section via a sliding rail. The aperture size can be modified by changing the overlap of the apertures on the feed and the center resonator, which allows the coupling aperture size to scale from 8 to 13 mm wide ($\ell = 0 - 5$ mm aperture overlap) by 2 mm tall. This additionally allows under-, critically-, and over-coupled resonances, which is necessary to minimize thermal noise contributions from the resonator itself, which could degrade

the receiver sensitivity. The central waveguide has dimensions 10.8 mm×6 mm×31.4 mm, and is designed for operation near the cutoff frequency, increasing uniformity of the vertically-polarized electric field along the propagation direction.

In simulation, the resonator has a reflection coefficient of -33.02 dB at 10.22 GHz, which occurs when the tuning plunger is at $d = 6.6$ mm and the coupling aperture overlap is at $\ell = 2.5$ mm. In this configuration, it also has a Q-factor of 4546 and an enhancement factor $F = 9.3$. To observe performance at a second Rydberg state, the resonator is set for a second resonance at 10.77 GHz. This occurs when the plunger is set to $d_{min} = 0$ mm and the coupling offset to $\ell = 0$ mm. At 10.77 GHz, the reflection coefficient is $|S_{11}| = -18.17$ dB, $Q = 5520$ and $F = 3.5$. The difference in resonator performance between the two Rydberg-state frequencies is due to deliberate placement of the vapor cell within the resonant cavity. The offset nature of the cell doubles the tuning range, at the cost of uniformity at higher frequencies.

The uniformity of the field within the vapor cell, and therefore within the resonator, is useful for improving the sensitivity of a Rydberg receiver. A highly non-uniform field will result in several Autler-Townes splittings, decreasing the resolution of the overall field amplitude measurement. The field distribution in the main section of the resonator at 10.22 GHz is plotted in Fig. 4.2.

This resonator is fabricated in Aluminum 6061 via CNC split-block machining and characterized on a Rohde-Schwarz ZNA calibrated with an X-band waveguide calibration kit to the plane of a WR-90 adapter. The resonator feed is connected to the adapter to record S_{11} measurements. With the tuners maximally displaced at $d_{min} = 0$ mm, $L_{min} = 8.3$ cm, the resonator exhibits a reflection coefficient magnitude of -3.74 dB at 11.26 GHz. With the tuners fully extended for $d_{min} = 8$ mm, $L_{max} = 9.9$ cm, the resonator shows a reflection coefficient of -30.37 dB at 10.16 GHz, representing a full tuning range of 10.16 to 11.26 GHz, or 1.1 GHz, plotted in Fig. 4.3. These measurements are conducted when the sliding feed is set to critical coupling at the frequency of choice (10.22 GHz). When a particular frequency is chosen, the resonance depth and coupling Q-factor can be changed by modifying the feed position. The secondary resonance off each peak is a deliberate design choice; this is a result of the vapor cell being slightly offset from center in the resonator, which enables a wider frequency-tuning range at the cost of uniformity.

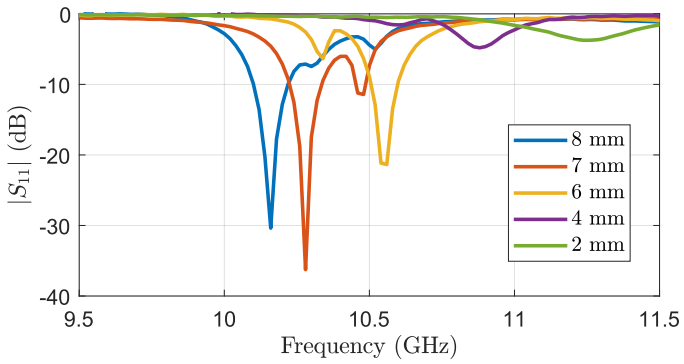


Figure 4.3: Measured reflection coefficient as a function of plunger displacement, which modifies the cavity length from 8 to 2 mm. The desired 10.22 GHz transition occurs when the cavity is $d = 7$ mm long (plunger displaced 1 mm.)

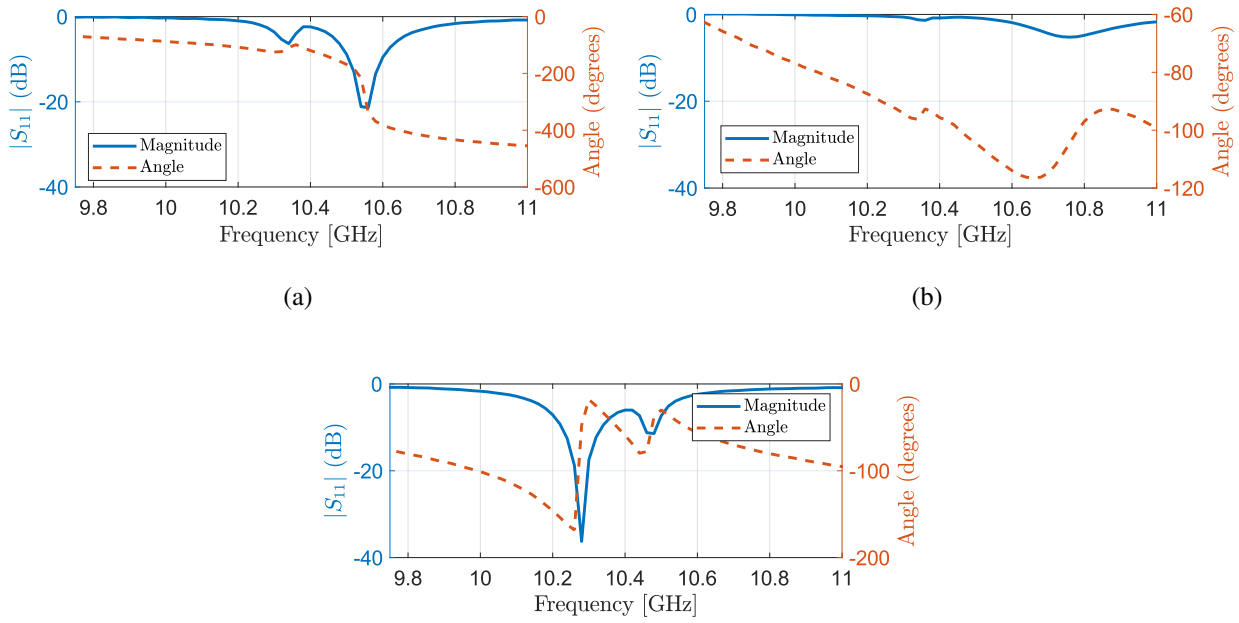


Figure 4.4: Resonator reflection coefficient magnitude and phase, indicating tuning to all three coupling regimes: over-, under-, and critically coupled, which are (a), (b), and (c) respectively.

Changing the coupling coefficient of the resonator is important for integration into a Rydberg system

to mitigate noise contributions from the resonator, which impacts overall system sensitivity. Three configurations of the sliding feed, corresponding to different coupling coefficients, are tested: maximum overlap (no offset) with $\ell = 0\,\text{mm}$; $\ell = 2.5\,\text{mm}$ offset; and $\ell = 5\,\text{mm}$ offset. The resulting magnitude and phase of S_{11} is plotted in Fig. 4.4.

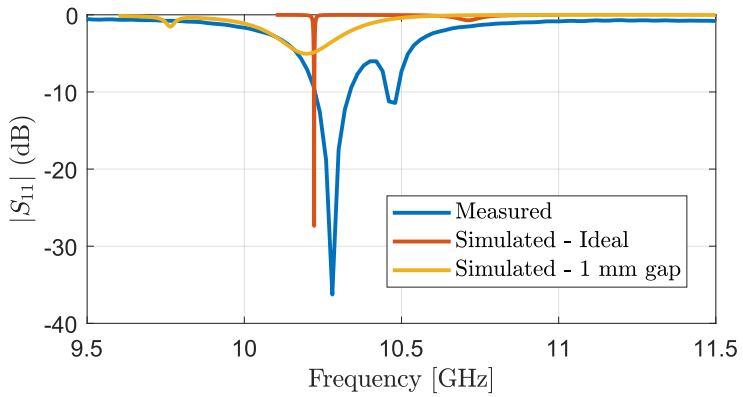


Figure 4.5: Simulated and measured resonant frequency for the $59D_{5/2}$ (10.22 GHz) Rydberg transition. Both values were calculated using a plunger depression of 1 mm and critical coupling. The small artifact measured on the blue trace is a result of the placement of the vapor cell within the resonator.

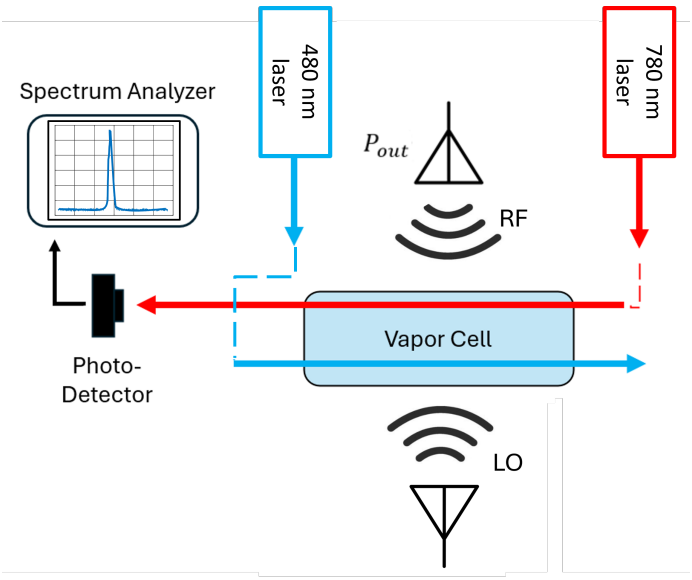
Measurements of the resonator without the vapor cell are made in order to identify the source of dips at other frequencies in the $|S_{11}|$ measurements. Here we assume that the vapor cell is made of low-loss 1-mm thick quartz with a permittivity of $\epsilon_r = 3.7 \pm 0.03$ and a loss tangent of $\tan\delta < 0.005$ from 320 MHz to 325 GHz [10]. Without the vapor cell, the cavity resonates at 11.96 GHz (-39.06 dB) in simulation, and at 12.70 GHz (-5.14 dB) in measurement. With the vapor cell, the Q-factor decreased from multiple thousand in simulation to 20 in measurement, corresponding to an enhancement factor of 2. Assuming the vapor cell is made of quartz and has 1 mm thick walls as specified by the manufacturer, the reduction in Q-factor is likely a result of the split-block assembly, where gaps between blocks and tolerances in the machining process can result in substantial loss at X-band. Additionally, further testing determined that the small notch in measured results is a byproduct of the vapor cell placement within the cell. A similar Q-factor degradation is observed when the vapor cell is inserted into the cavity, as shown in Fig. 4.5. Furthermore, the degradation

in Q-factor did not change between measurements with and without the cell, indicating that the Rubidium within the cell is not condensed enough to change the conductivity on the cell walls [92]. Measurements are made after the vapor cell had been heated at 450°F for two hours, to improve the Rubidium distribution in accordance with recommendations in the literature, but does not yield any significant improvements in Q-factor.

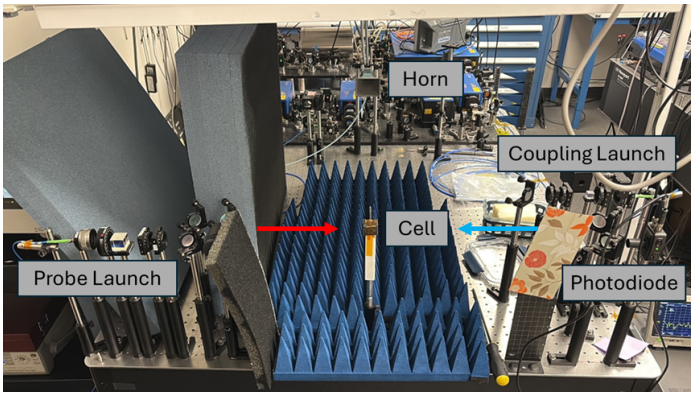
4.2 Rydberg Receiver Sensitivity Enhancement Measurements

The sensitivity of the Rydberg receiver is characterized with and without microwave enhancement as shown in Fig. 4.6. The setup consists of two Toptica DL pro lasers with wavelengths at 480 nm and 780 nm mounted to an optical table and connected to Toptica DLC pro control modules. The current and temperature of the 780 nm red probe laser are adjusted such that the laser is coarsely locked to the Rubidium spectroscopic line at 780.24 nm. The 480 nm blue coupling laser scans over a narrow range centered on the wavelength of choice, which varies for the multiple measurements taken. Both lasers are aligned through the vapor cell via dichroic mirrors, which combine and separate the counter-propagating blue and red beams. The coupling laser light is absorbed after the vapor cell, and the probe light continues to the Thorlabs PDA36A2 photodetector. The photodiode output is connected to a spectrum analyzer for sensitivity measurements or an oscilloscope for diagnostics, splitting, or shift measurements.

The probe laser wavelength at 780.24 nm has an optical power less than 1 mW and does not saturate the atomic transition of the Rubidium in the cell [44]. Similarly, the 480 nm coupling laser varies in power between measurements, as different atomic transitions require varying power levels, but is within the range of 20–200 mW. The lasers each have a beam waist of less than 1 mm. Testing the empty cavity shows near 100% transmission of both the probe and coupling beams, and no observable beam scatter, meaning the beams are well-focused and aligned through the resonator. Referring to Fig. 4.1, the lasers are co-polarized in the vertical z direction. The optical power of each laser is chosen to optimize EIT resolution.



(a)



(b)

Figure 4.6: (a) The optical scheme used for the Rydberg receiver. Off table, the photodetector connects to a spectrum analyzer for readout of the splitting response. Additionally, the laser head current, temperature, and scan amplitude are controlled by external modules. (b) The test set-up, as arranged in the lab. In experiment, a singular horn delivers the RF and LO fields, to simplify the number of devices used.

Previous sensitivity measurements of Rydberg receivers indicate that condensed Rubidium within the vapor cell has a significant impact on performance. This is especially important when employing a metallic waveguide resonator; while the gaseous form of Rubidium does not interact with the vapor cell

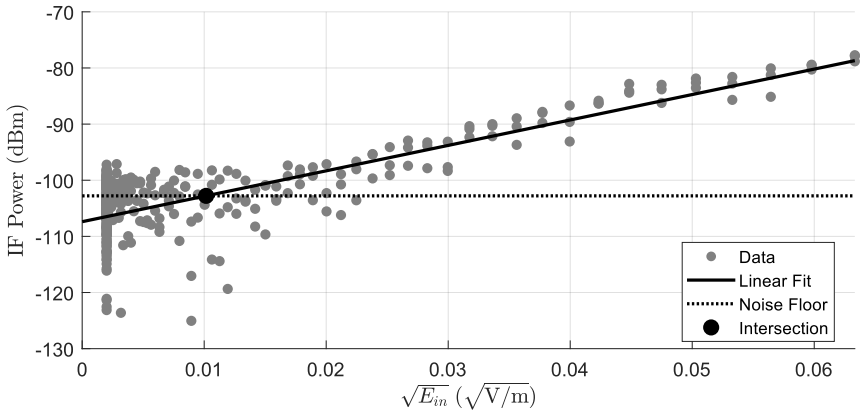
[75], condensed Rubidium is a conductor that changes the electrical properties of the quartz cell walls. In turn, this can impact the resonant frequency and Q-factor of the waveguide resonator, which can degrade the sensitivity of the overall receiver. Therefore, to mitigate potential performance degradation from condensed Rubidium, the vapor cells are heated in an oven at 450°F for one hour before receiver measurements are made.

4.2.1 Free-Space Recevier at 10.22 GHz

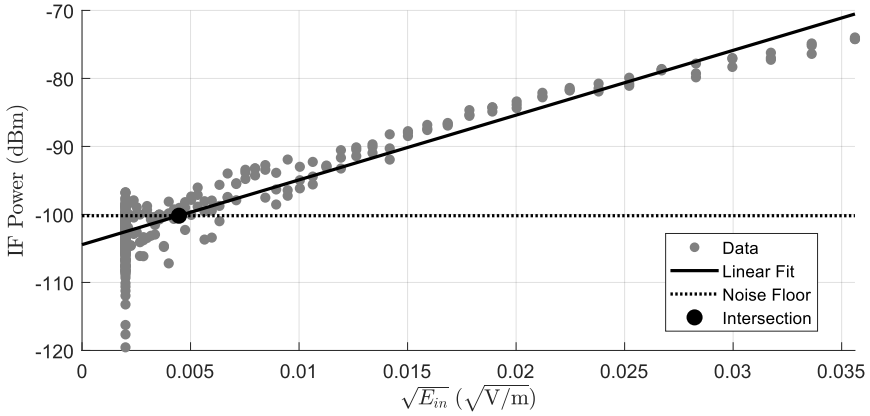
First, the receiver performance is characterized in free-space, without the resonator, using the 2 cm long cell described above, as well as a larger 7.62 cm long cell in order to show the impact of interaction volume on receiver performance. For the large cell, the RF electric field is set to 10.22 GHz, with the power swept to determine system sensitivity. The LO is set to the same frequency, with a power from the source that varies from -5 to $+5$ dBm, corresponding to an incident LO electric field magnitude of approximately 0.01 V/m at the vapor cell. Both signals are provided by signal generators, and combined using a 10 dB NARDA 4229-10 coupler. To determine the sensitivity of the Rydberg receiver, the output of the photodetector is connected to a spectrum analyzer set to 10 Hz resolution and video bandwidth. The probe laser is set to 780.24 nm with 80 μW output power. The coupling laser is set to 479.81 nm with 30 mW output power. The full atomic transition of this system is from the ground state at $5\mathrm{S}_{1/2}$ to the intermediate state at $5\mathrm{P}_{3/2}$ via the red probe 780.24 nm laser, to the Rydberg state at $59\mathrm{D}_{5/2}$ via the blue coupling 479.81 nm laser, to the AT splitting state at $60\mathrm{P}_{3/2}$ via an external 10.22 GHz RF field.

The sensitivity is characterized via two methods: direct AT splitting measurements; and RF path loss measurements [56]. In both cases, the noise equivalent field is calculated from the expression $NEF = C\sqrt{\mathrm{NEP}}$, where NEP is the noise-equivalent-power from the signal source. The two methods vary in the calculation of C. In the direct method, which yields a sensitivity of NEF_{AT}, the power of the RF signal is varied and the distance (in frequency) between the AT splitting peaks is measured. A fitting function is generated from this data to establish the minimum power required to resolve the Autler-Townes splitting. This utilizes the expression $|E| = (h/\rho)\Delta f_{AT}$ for the electric field inside the cell along the optical path, discussed in the introduction of this chapter. In the noise floor method, the intermediate frequency power is

measured by a spectrum analyzer, as a function of the power of the RF source, which is gradually reduced to find the noise floor of the system. This noise floor is then converted into a noise equivalent field value, NEF_{RF}, which expresses the field just in front of the cell. The variance in sensitivities between these two methods can be attributed to the slightly different locations at which the fields are sampled to calculate the NEF. The setup for both sets of measurements is shown in Fig. 4.6.



(a)



(b)

Figure 4.7: The output power (received at the spectrum analyzer) as a function of the electric field. Plot (a) is for the small Precision Glassblowing vapor cell while plot (b) is for the larger ThorLabs vapor cell. The electric field is gradually decreased to find the noise floor of the system, such that it can be fit with a line to determine the minimum field that can be resolved by the receiver.

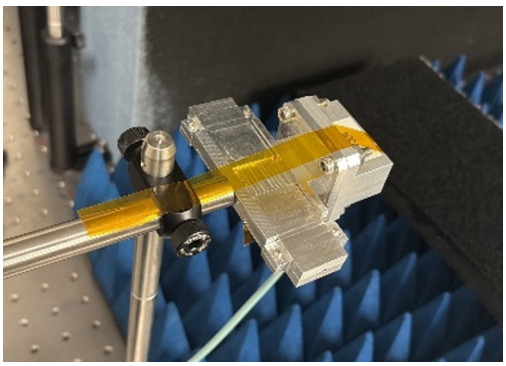
In free space, without any form of microwave enhancement and using a large Rb vapor cell, the system exhibits an AT-splitting sensitivity of $NEF_{AT} = 17\ \mu$V/m/$\sqrt{\text{Hz}}$, or an RF-defined sensitivity of $NEF_{RF} = 10\,\mu$V/m/$\sqrt{\text{Hz}}$. This metric is achieved using a standard X-band horn antenna placed one meter away from the vapor cell with a gain of 16.35 dB at 10.22 GHz, for an on-resonant energy transition at $59\text{P}_{1/2}$. The free-space path loss is calculated from the known antenna gain, and together with cable losses amounts to 53.96 dB, which is included in the data of Fig. 4.7.

In comparison, when the same measurements are performed for the smaller Precision Glassblowing vapor cell with an interaction length of 2 cm, the AT-splitting sensitivity is reduced to $NEF_{AT} = 56\,\mu$V/m/$\sqrt{\text{Hz}}$ or an RF-defined sensitivity of $NEF_{RF} = 51\,\mu$V/m/$\sqrt{\text{Hz}}$. The shift in sensitivity as a function of vapor cell size is predicted by the literature [92], and is the function of a variety of factors. The smaller vapor cell has a shorter interaction length, thus eliciting a weaker response from the atoms. Additionally, the vapor cell radius is small enough that the atoms experience significant interactions with the quartz glass cell walls. The noise floor measurements for the large and small cell are shown in Fig. 4.7. Each blue dot on the plots represents a singular power measurement, with the value gradually decreasing to identify the noise floor using the first order polynomial fitting line in black. In our free-space sensitivity measurements of the Thorlabs cell, we observed a residual electric field that we attribute to leakage from the RF source, which is present whether the RF output is connected or disconnected from the transmit antenna. This suggests the digital synthesis inside the system is leaking through the case, rather than leakage through the SMA cable. Placing RF absorber around the source mitigates the leakage signal somewhat but is not completely effective. In future efforts, more care can be taken to use RF absorber to surround the RF sources and better isolate the test area from external signals.

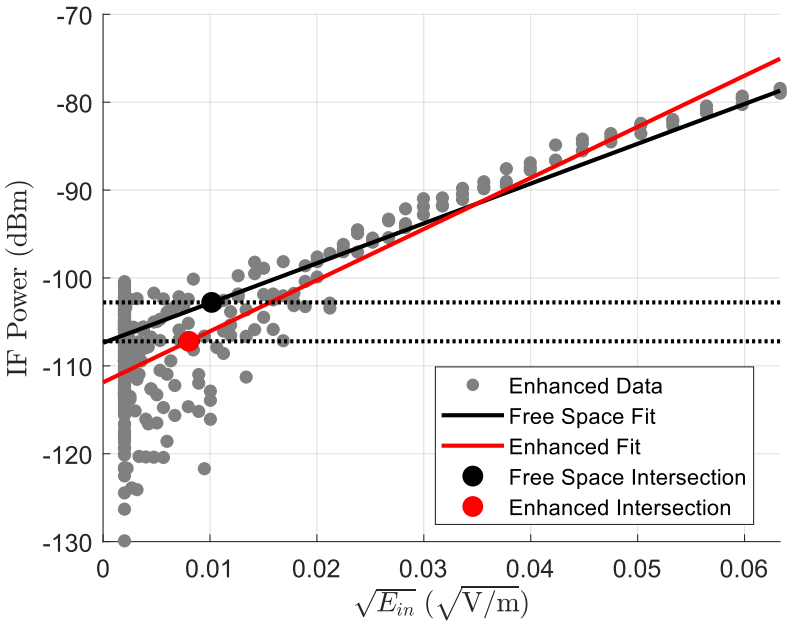
4.2.2 Enhanced Receiver at 10.22 GHz

We next describe sensitivity measurements of the Rydberg receiver at 10.22 GHz using the small vapor cell integrated with the tunable cavity, in an on-resonant configuration. The laser power and wavelength are the same as in the free-space configuration, with laser alignment only slightly adjusted to accommodate the new position of the vapor cell inside the resonator. The RF and LO electric fields are directly fed into the

cavity through a WR90 waveguide to 3.5-mm coaxial adapter. The resonant frequency is measured using a vector network analyzer (VNA), which shows the cavity resonance at 10.279 GHz with a corresponding $|S_{11}|$ = -22.93 dB.



(a)



(b)

Figure 4.8: (a) The port-coupled resonator as positioned in the Rydberg receiver. Foam is placed on the metallic optical table to minimize environmental noise effects. (b) The power received at the spectrum analyzer as a function of the electric field inside the vapor cell for the 10.22 GHz measurement configuration.

The on-resonant configuration exhibits a noise equivalent field of 34 μV/m/$\sqrt{\text{Hz}}$. A photograph of the resonator in the setup as well as the noise floor measurements are shown in Fig. 4.8. With the introduction of the resonator, the sensitivity of the receiver improves from 51 μV/m/$\sqrt{\text{Hz}}$ in free space to 34 μV/m/$\sqrt{\text{Hz}}$ with enhancement, corresponding to an enhancement factor of $F = 1.5$. By observing Fig. 4.7 and Fig. 4.8, it is obvious that a larger interaction volume enables higher sensitivity, while the enhancement cavity recovers some of that sensitivity in the case of a smaller vapor cell.

4.2.3 Free Space and Enhanced Receiver at 10.77 GHz

Next we characterized the free-space and enhanced sensitivity of the receiver at 10.77 GHz. The full atomic transition in this case is from the ground state at $5\text{S}_{1/2}$ to the intermediate state at $5\text{P}_{3/2}$ via the red 780.24 nm laser, to the Rydberg state at $58\text{D}_{5/2}$ via the blue 479.84 nm laser, to the AT splitting state at $59\text{P}_{3/2}$ via the 10.77 GHz incident RF field. The resonator is tested on the VNA with $|S_{11}|$ = -17.06 dB at 10.77 GHz. The measurement results are qualitatively similar to those in Fig. 4.8. The sensitivity improves from 49 μV/m/$\sqrt{\text{Hz}}$ in free space to 32 μV/m/$\sqrt{\text{Hz}}$ with enhancement, corresponding to an enhancement factor of $F = 1.53$, in good agreement with measurements taken at 10.22 GHz.

4.3 Additional Effects on Sensitivity and Resolution

We investigated several relevant parameters that affect sensitivity and resolution. The first is the position of the laser beams within the vapor cell, measured using the larger Thor labs cell. The second effect is the impact of VNA calibration, showing the ability of the Rydberg receiver to measure standing waves.

To investigate how the location of the laser beams inside the vapor cell affects the resolution, measurements are performed with the 7.62-cm long cell that has a 2.54 cm diameter, allowing variations in laser beam sampling. Nominally, the AT splitting measurements are taken with the probe and coupling beams positioned 0.3175 cm (1/8") from the front wall of the cell, indicated in Fig. 4.9. The resulting AT splitting for center, front, and back of the cell at the same output power from the RF generator are shown in Fig. 4.9. The measured vertically-polarized electric field amplitude in the front of the cell appears to be substantially smaller compared to the the field in the center of the cell. The measurement in the back of the cell shows

an inhomogeneous field. The important conclusion of the results from Fig. 4.9 is that the cell affects the measured field. In publications to date, the reported field values are measured at the center of the cells, e.g. [44], and do not report the diffraction effects due to reflections off the cell walls.

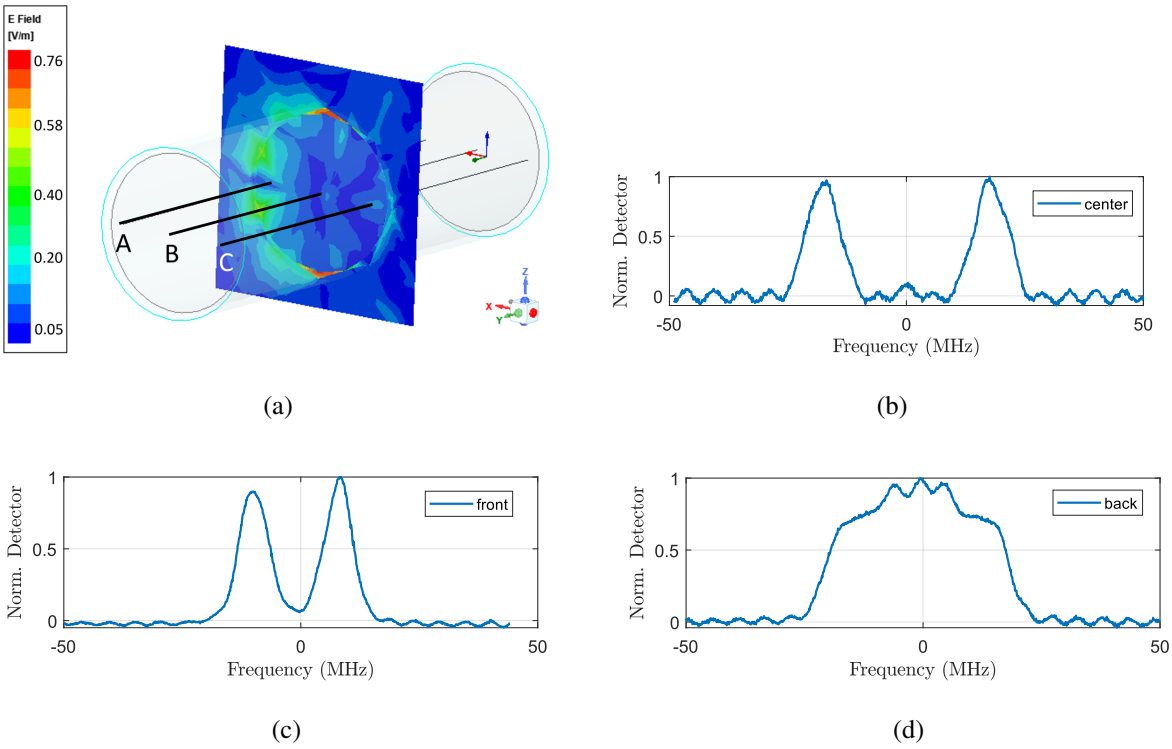


Figure 4.9: (a) Horn antenna and vapor cell. The "center" sample occurs in the middle of the central cylinder on the cell, line B. The "front" occurs on the side of the glass closest to the horn, line A. The "back" occurs on the side of the glass farthest from the horn, line C. The photo is a representation of the set-up and does not indicate the actual distance between horn and cell. (b)-(d) 10.8 GHz free-space AT splitting at different locations in the Thorlabs cell for equal incident field.

In addition to cell-wall reflections, there can be other impedance mismatches in the equipment setup itself, e.g. from cables and connectors. It is interesting to show that the Rydberg-atom electric field measurements can detect such reflections. An experiment is performed by setting the resonator to an arbitrary well-defined resonance between 10.22 and 10.77 GHz. We choose one around 10.33 GHz and measure $|S_{11}|$ with a VNA calibrated to the SMA connector at the end of a 1.4-m long 3.5-mm cable.

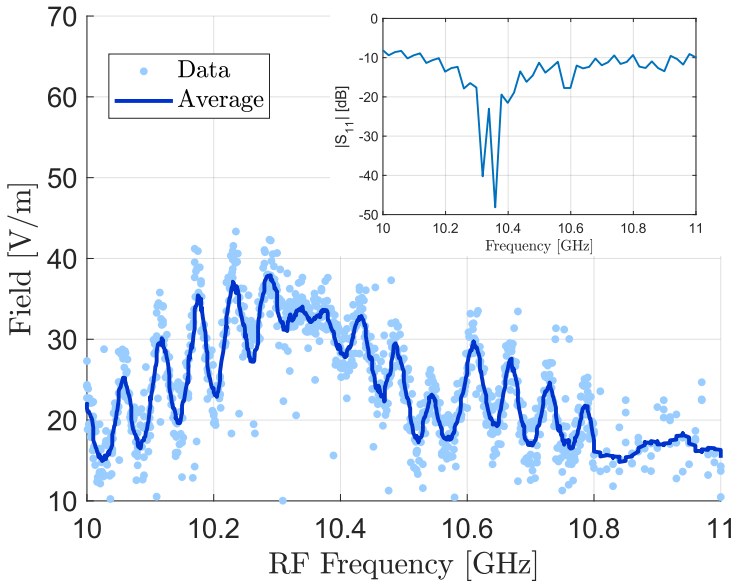


Figure 4.10: Field measured with AC Stark shifts. All lines are spaced by 59 MHz highlighting the shared periodicity, with unique offset for each measurement and above and below 10.3 GHz. Inset to (b), $|S11|$ measurement of the Cavity with the cell held in place with packing peanuts. There are two resonance troughs, -48.1 dB at 10.36 GHz and -40.3 dB at 10.31 GHz.

The resonance dips are at 10.32 GHz ($|S_{11}| = -40.3$ dB) and 10.36 GHz ($|S_{11}| = -48.1$ dB). VNA measurements of the cavity can be observed in the inset of Fig. 4.10, showing uncalibrated ripples. The long SMA cable is not calibrated using SLOT calibration, therefore creating a standing wave. The separation between ripples is about 59 MHz, which corresponds to a cable of length 1.75 m assuming a relative permittivity of 2.1 (PTFE), corresponding to the actual cable in the experiment that is 1.8 m long. Off-resonant (AC Stark shift) measurements of the 61S state at many frequencies are used to map the field internal to the cavity, with results shown in Fig. 4.10. The 59-MHz is clearly measured by the Rydberg sensor. Note that the general resonance shape without the standing wave agrees with the Ansys HFSS simulations in Fig. 4.3(b). The measurement at the same location within the vapor cell shows a standing wave as well, indicating that the atoms are respond to the actual field strength, which is affected by the reflections at the ends of the cable. The Rydberg sensors are effectively taking on the role of the network analyzer to detect impedance mismatch at the ends of the cable which produces the incident RF field.

4.4 Conclusions

We show that field enhancement in the microwave domain improves Rydberg-atom RF receivers to be more competitive with conventional LNA-based receivers. This chapter demonstrates the capability of a single metallic resonant waveguide cavity to enhance multiple on-resonant Rydberg transitions, with demonstrations at 10.22 and 10.77 GHz. Experimental validation shows an enhancement factor of 1.5, lower than the theoretical limit by a factor of about 6. This reduction in enhancement is due to practical limitations related to the cavity Q-factor, such as insertion of the vapor cell, machining roughness, gaps due to the split-block manufacturing, and radiation through various apertures in the metal of the resonator related to placement of the cell. In simulation, the resonator shows 620 MHz of frequency tunability, which is accomplished through the use of two frequency-tuning pistons on either side of the resonator. Measurements confirm simulations of coupling tunability, with over-, critically, and under-coupled configurations. In measurement, the resonator shows 1.1 GHz of frequency tunability.

The results of the on-resonant experiments are summarized in Table 4.1. The free-space Rydberg set-up is characterized to generate baseline measurements for the receiver sensitivity at 10.22 GHz. This sensitivity is $NEF_0 = 10$ μV/m/$\sqrt{\text{Hz}}$ with a larger, 7.62 cm long ThorLabs vapor cell, and $NEF_0 = 51$ μV/m/$\sqrt{\text{Hz}}$ with the 2 cm long Precision Glassblowing cell. The degradation in sensitivity is in part due to the decreased interaction length in the small cell compared to the larger cell. When introducing the resonator, the noise equivalent field improved to 34 μV/m/$\sqrt{\text{Hz}}$, or an enhancement factor of $F = 1.5$. Similar enhanced measurements are conducted at 10.77 GHz, which exhibited a free space sensitivity of $NEF_0 = 49$ μV/m/$\sqrt{\text{Hz}}$, and an enhanced sensitivity of $NEF_0 = 32$ μV/m/$\sqrt{\text{Hz}}$, or an enhancement factor of $F = 1.53$.

Table 4.1: Summary of on-resonant experimental results.

Freq (GHz)	Enhanced?	NEF (μV/m/$\sqrt{\text{Hz}}$)
10.22	No	51
10.22	Yes	34
10.77	No	49
10.77	Yes	32

The results are compared to other microwave-based, sensitivity-enhancing topologies in Table 4.2. The largest enhancement is obtained for a single L-band transition with a lumped-element resonator surrounding the vapor cell, which is not scalable easily to higher frequencies. The off-resonant sensor in [3] does not report their free-space sensitivity, but would be fundamentally limited due to the off-resonant sensing set-up. In [93], [92] single-frequency resonators at X-band are shown with cells $25\,\text{mm}$ long and $4\,\text{mm}$ wide and $20\,\text{mm}$ long and $10\,\text{mm}$ wide, respectively. According to the literature, this is the only multiple-transition enhancement device for on-resonant sensors.

Table 4.2: Comparison of Rydberg-atom receiver enhancement in the microwave domain.

Source	Freq (GHz)	On-Res	F	NEF
[45]	1.3	Yes	100	5.5 μV/m/$\sqrt{\text{Hz}}$
[3]	2.58-5.15	No	16.2	N/A
[93]	15.10	Yes	14	N/A
[92]	10.22	Yes	14.5	23 μV/m/$\sqrt{\text{Hz}}$
This work	10.16-11.26	Yes	1.5	32 μV/m/$\sqrt{\text{Hz}}$

Connecting a receiving antenna with a gain G to the resonator would increase the sensitivity of the

overall receiver by a factor of $NEF/\sqrt{\mathrm{G}}$. For example, in the case of the measurements at 10.22 GHz, the a noise equivalent power (with path loss) of -82.8 dBm/Hz corresponding to $NEF = 32\,\mu V/m/\sqrt{\mathrm{Hz}}$. When a receiving antenna with $G = 3/2$ (short dipole) is included, the sensitivity improves to $NEF = 27.76$ μV/m/$\sqrt{\mathrm{Hz}}$. Future promising improvements for metallic resonators could leverage the longer interaction lengths of larger cells, adding an electrically-small antenna, and reducing losses in the cavity with improved fabrication. The results shown in this Chapter are currently in preparation for submission.

Chapter 5

V-band and S-band Rydberg-atom Sensor Measurements

Rydberg-atom receivers can potentially compete with the sensitivity of LNA-based receivers at millimeter-wave frequencies above 75 GHz, due to the intrinsic device limitations in low-noise amplifiers [94]. However, there have been limited demonstrations at millimeter-wave frequencies, e.g. [63], which details a receiver configured with cesium at 96 GHz (W-band). The majority of publications address the frequency range between 2 and 8 GHz [43], [61], [31]. Some receivers have also been demonstrated at X-band [92] [112]. With the performance gap in sensitivity between Rydberg and conventional receivers, all areas of performance degradation in the system should be well-characterized. To date, there has been limited literature documenting the impact that radio-frequency (RF) components have on this type of a quantum electrometer. Here we present a millimeter-wave two-photon Rydberg electrometer at 61.32 GHz ($34\mathrm{D}_{5/2}$ to $33\mathrm{F}_{7/2}$ transition), expanding the literature on higher-frequency RF atomic receivers. Additionally, we characterize the impact of RF components on Rydberg-atom sensor measurements, and we investigate effects of incident RF power density and polarization on the electrometer accuracy and sensitivity.

Furthermore, Rydberg receivers are useful at low frequencies because the aperture size (vapor cell) does not scale with resonant frequency like in conventional receivers. In theory, a Rydberg receiver with a highly stable coupling laser and widely tunable wavelength could change in sensing frequency between MHz and THz regimes without a physical change in hardware. In this chapter, we will discuss the potential frameworks for analyzing Rydberg receivers in the electrically-small antenna regime and introduce a unique method for sensing low frequencies using a high-frequency intermediate energy level. Then we will present demonstrated sensitivity in a low-frequency Rydberg receiver, analyze the impact that the local oscillator

has on the receiver, and demonstrate the receiver's immunity to interference from a potential interferer.

5.1 V-band Set-Up and Measurements

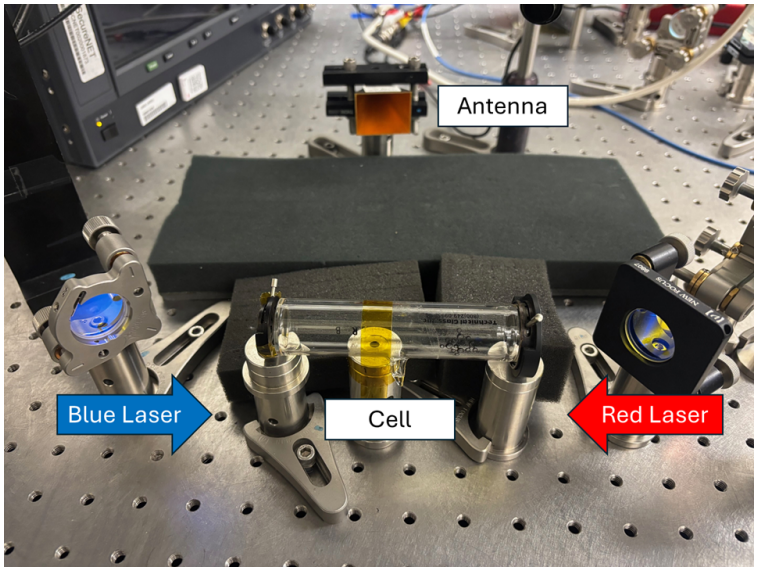


Figure 5.1: The Rydberg electrometer setup, consisting of a vapor cell, two lasers, and a photodetector (out of view). The incident millimeter-wave field is radiated from a V-band standard gain horn antenna for the experiments discussed in this paper.

The Rydberg electrometer two-photon setup with a rubidium vapor cell is shown in Fig. 5.1. A ThorLabs 8 cm long and 2.5 cm diameter vapor cell is filled with natural isotopic abundance rubidium. The cell material is quartz glass. A near-infrared Vescent laser and saturated absorption spectroscopy system at 780 nm is the "probe", while a blue Toptica DL pro laser and control module with wavelength around 480 nm is the "coupling" beam. The red laser is tuned to rubidium spectroscopic line 780.24 nm to excite the atoms from the ground state at $5S_{1/2}$ to the intermediate $5P_{3/2}$ energy state. The blue laser scans across a wavelength range centered on 481.43 nm, exciting the atoms from the intermediate state to the Rydberg state at $34D_{5/2}$. Both lasers have beam waists < 1 mm. The red laser power is set to approximately 0.1 mW, while the blue laser is set to ≈ 30 mW. The counter-propagating laser beams are aligned through the vapor cell with dichroic mirrors, where the red light transmission is detected using a photo-detector, which connects to the

DL pro laser module for data monitoring and capture. The lasers are vertically polarized, and co-polarized with the incident millimeter-wave electric field.

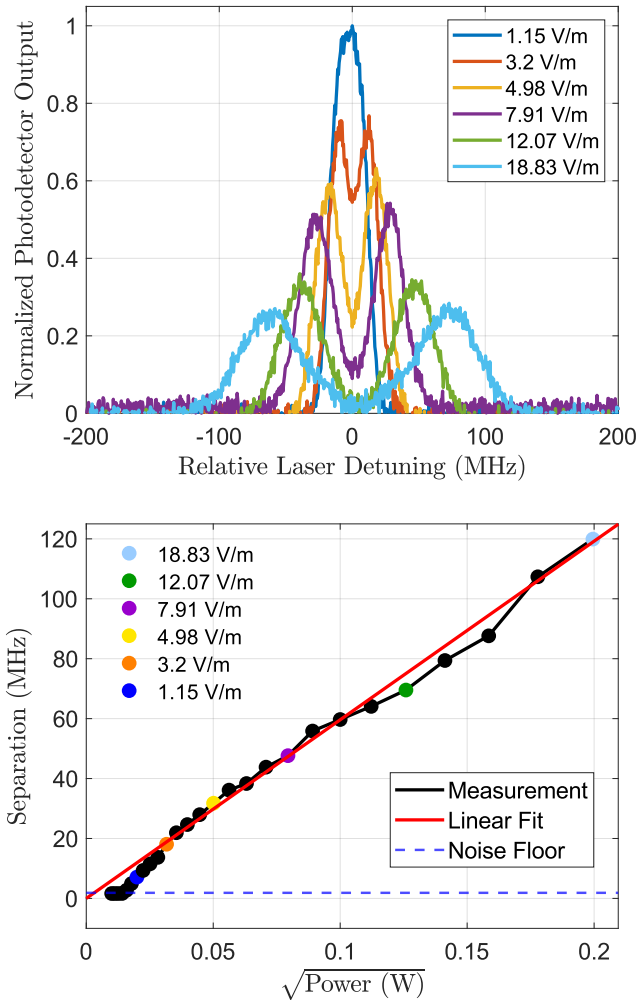


Figure 5.2: (a) Measured AT splitting for a range of incident millimeter-wave electric field magnitudes, obtained by varying the signal generator power. The y-axis is in arbitrary units of transmitted probe laser power. The value of ρ for this energy transition is $628\alpha e$ where α is the Bohr radius and e is the electron charge. (b) The magnitude of AT splitting versus signal generator output power from 0.01 to 0.2 W. We expect the response of the system to be linear. Deviations from this trend are due to peak broadening at high powers and to limitations from the EIT linewidth at lower power levels.

The incident RF electric field is provided by a Keysight E8257D signal generator set to output at

61.32 GHz, which corresponds to the $34D_{5/2}$ to $33F_{7/2}$ AT splitting state. The signal generator is connected to a 1.85-to-1 mm adapter, a 1 mm cable, and a 1 mm-to-WR15 adaptor, adding together 6 dB of loss. The V-band (50–75 GHz) horn antenna has a WR15 feed and a measured gain of 23 dBi. The horn antenna is placed in the antenna far field, 40 cm away from the vapor cell. In initial measurements, the power from the signal generator is swept to observe the AT splitting as a function of power, with measured results shown in Fig. 5.2. The measurements are compared to the theoretically calculated field values at the same point, which are calculated from the power density assuming a known antenna gain G_T and free space impedance (377 Ω), such that:

$$E = \sqrt{377 \frac{P_T G_T}{4\pi d^2}} \tag{5.1}$$

where P_T is the signal generator power in watts and d is the distance from the source antenna to the vapor cell. The sensor has a limit on the resolution of the AT split at lower field amplitudes, as indicated by the measurement at 1.15 V/m, where the two peaks have nearly returned to a singular peak. At higher powers, the AT peaks exhibit an effect called "power broadening". Previous literature indicates that high laser power densities can cause EIT lineshapes to broaden [36], and it is likely that a similar effect occurs in the AT splitting state. For example, with a 3.2 V/m field, we observe a linewidth of of 8.29 MHz. However, this broadens to 25.1 MHz with a 18.83 V/m field, indicating that there are constraints on the RF field amplitudes that can be reliably sensed with Rydberg quantum sensors. Furthermore, the results from the AT splitting measurements are then compared to the RF electric field magnitude calculated at the location of the cell and at the same distance from the antenna, as shown in Table 1. The field magnitudes from measurement and calculation are overall in good agreement, with the margin of error falling between 0.5 and 6% for higher input powers. Notably, there is a distinct error in the lower power level, as it is difficult to resolve the AT splitting peaks at such low powers.

Additional power measurements are taken to determine the effective noise floor and the response linearity of the system. An ideal Rydberg system would directly correlate AT splitting with electric-field magnitude, as shown in the introduction of this thesis. Furthermore, the sensitivity threshold of this receiver

is fundamentally limited due to the lack of laser locking mechanisms, and the absence of a local oscillator field to enhance sensitivity [43]. The subsequent system noise floor can be seen in Fig. 5.2. The AT splitting response should be linear, as shown in Eq. 1. This is true for the AT splitting measurements made at intermediate power levels. However, at very high power levels, the peaks exhibit power broadening that make it difficult to resolve the frequency separation between them, and causes the graph to deviate from a linear response. Similarly, at low power levels, the distance between peaks is difficult to resolve as it is on the order of the EIT linewidth, which is half the FWHM, which is 9.83 MHz. This linewidth limit is dominated by the transit time broadening, a constraint that arises from the limited time the atoms have to interact with the lasers. The linewidth limit is why the linearity of the AT splitting deviates when the separation is under 20 MHz.

Additionally, we characterize the impact that polarization loss has on the AT splitting resolution. The antenna is mounted to a rotating mount, and the AT splitting is recorded in 15-degree sweeps. The laser wavelength, power, and alignment are held constant from the power measurements. Four AT-splitting plots with different polarizations are plotted on Fig 5.3. Additionally, this data is refined using Savitzky-Golay filtering, in order to resolve the slight deformation differences between measurements at $\theta = 60$ and 90 degrees. At 0 degrees, the electric field with a 8 dBm input power is 10.43 V/m. For the same configuration, but a 30 degree rotation, the electric field is 8.52 V/m. This constitutes a loss of 0.06 V/m per degree of rotation between 0 and 30 degrees. However, though the most defined AT splitting occurs when the field and lasers are co-polarized, there is still a resolved field measurement when the field is polarized in the orthogonal direction. When the antenna mount is rotated 90 degrees, effectively presenting a horizontally-polarized field to the atoms, it decreases the magnitude of the splitting peaks, effectively degrading the SNR of the measurement. Additionally, a distorted EIT lineshape is introduced that degrades the resolution of the splitting. This distorted lineshape may be a function of the the energy levels, such as the additional excitation of the m_j levels as the RF excitation changes. In the RF domain, this may also be a function of the changing Fresnel coefficients in the vapor cell as the field is rotated.

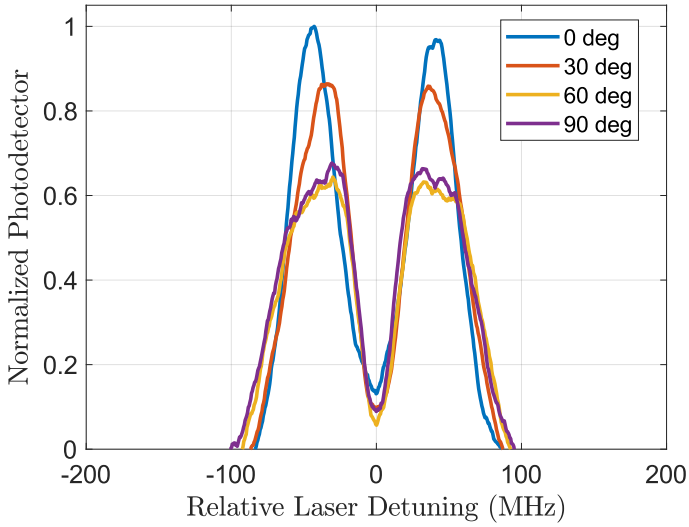


Figure 5.3: AT splitting versus degree of antenna polarization. At 0 degrees, the electric field from the horn and the lasers are fully co-polarized in the vertical direction. At 90 degrees, the electric field is entirely in the horizontal direction. Though the atoms are still able to resolve the rotated field, there is some degradation in the resolution associated with the polarization mismatch.

By characterizing the AT splitting response of a Rydberg-atom electrometer as a function of incident RF power and polarization, we investigate sources of performance degradation that arise from RF-based components in the quantum sensor. These effects are particularly important as Rydberg electrometers and receivers currently under-perform compared to their conventional electronic counterparts using low noise amplifiers. Field measurements based on Autler–Townes splitting demonstrate good agreement with calculated far-field electric field values over a range of input powers, as shown in the table below:

Table 5.1: Comparison of Theoretical and Measurement E-field

Power (dBm)	AT Field (V/m)	RF Field (V/m)	Percent Error
16	18.83	19.03	1.05
12	12.07	12.01	0.50
8	7.91	7.57	4.49
4	4.98	4.78	4.18
0	3.2	3.01	6.31
-4	1.15	1.9	39.47

The variance between measured and calculated field values, and therefore the error of the Rydberg-atom receiver, is between 0.5 and 6% at intermediate power levels. Deviations from ideal linear behavior are observed at both ends of the power sweep. At low input powers, the AT splitting approaches the system noise floor, limiting the minimum resolvable field to approximately 0.25 V/m, corresponding to a splitting of about 2 MHz. At high input powers, power broadening of the EIT lineshape makes it difficult to accurately resolve the peak separation. These results indicate limitations on a Rydberg-atom quantum sensor's ability to resolve high and low power levels. Polarization measurements further show that co-polarization between the RF electric field and the optical fields produces the most well-defined AT splitting. Additionally, as the polarization mismatch increases, the measured field resolution decreases. Notably, even under orthogonal polarization conditions, the sensor retains some sensitivity to the incident field, though with a degraded signal-to-noise ratio. This behavior underscores the importance of field alignment.

5.2 Low Frequency Comparison to Conventional Receivers

The performance of Rydberg-atom electric field sensors at low frequencies has been documented within the established literature. In [28], fields in the range of approximately 100 kHz to 40 MHz are measured using an indirect detection approach, yielding a noise-equivalent field of about 14 mV/m/$\sqrt{\text{Hz}}$.

for an applied field amplitude of 80 V/m. Additional work from 770 Hz to 1.5 kHz achieved an NEF of 0.34 mV/m/$\sqrt{\text{Hz}}$. over the frequency range [53]. Over a large frequency range, from kilohertz to 200+ MHz, a low-frequency Rydberg receiver exhibited a sensitivity of between 0.4 and 2 mV/m/$\sqrt{\text{Hz}}$. All the above measurements are collected from Rydberg receivers in off-resonant detection schemes, reducing the potential sensitivity threshold significantly. Thus, it is clear that Rydberg receivers are of most interest in low-frequency regimes because of their aperture-independent nature.

The correct framework to analyze a Rydberg receiver as an electrically-small antenna is not trivial. The limits imposed on traditional electrically-small antennas do not apply because of the underlying assumptions in a Rydberg receiver. For instance, the Chu/Wheeler/Harrington limit [27] establishes the relationship between antenna Q and size, given the minimum radius of a sphere enclosing the antenna, L_A, such that:

$$Q = \frac{\lambda}{2\pi L_A} + \left(\frac{\lambda}{2\pi L_A}\right)^3 \tag{5.2}$$

$$FBW = \frac{1}{Q}\frac{VSWR - 1}{\sqrt{VSWR}} \tag{5.3}$$

where FBW is the fractional bandwidth, VSWR is the voltage standing wave ratio for the antenna, L_A is the length of the antenna, and λ is the wavelength. The figure-of-merit is typically that of the FBW_V times the efficiency η. The maximum efficiency η is the measured gain over ideal gain. Together, it is possible to place a constraint on the bandwidth as a function of size of an electrically-small antenna. This is shown in Fig. 5.4.

In Fig. 5.4, we assume that the bandwidth is determined by the tuning range of the Rydberg-atom receiver. In theory, this is a fairly wide range, but diode lasers have a finite frequency tuning range and potential mode-hopping. Thus, we assume a modest tuning range of 200 MHz from a single Rydberg-atom receiver. Furthermore, the efficiency of the quantum receiver is expressed as:

$$\eta = \frac{8\pi k_B T_0}{\text{NEF}^2 c\epsilon_0 D\lambda^2} \tag{5.4}$$

where T_0 is the environment temperature, NEF is the sensitivity of the receiver, and D is the directivity

[114].

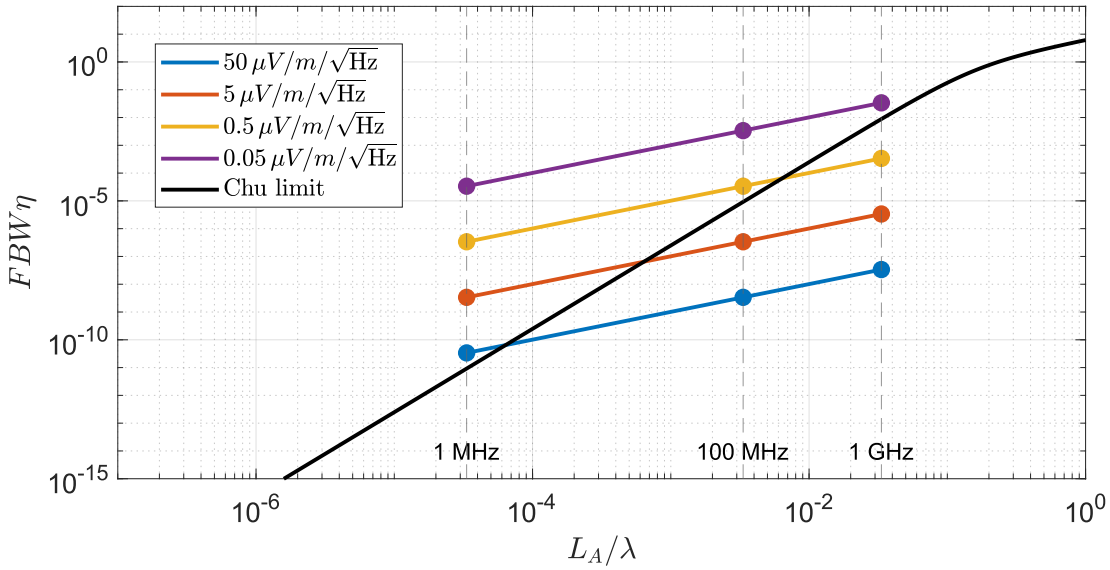


Figure 5.4: The Chu limit as a function of antenna size. For the conventional limit (black line), we assume a VSWR of 2, and a maximum η of 1. For the Rydberg-atom receivers, we assume a vapor cell that is 1 cm long, in a room temperature (290 K) environment. [99]

From Fig. 5.4, we see that Rydberg receivers do not always outperform the Chu limit in terms of aperture size. For example, a 1 cm vapor cell does not have a size advantage in a receiver with a poor sensitivity of 50 $\mu\text{V}/\text{m}/\sqrt{\text{Hz}}$ operating at 1 GHz. However, the same vapor cell inserted into a receiver of high sensitivity 0.5 $\mu\text{V}/\text{m}/\sqrt{\text{Hz}}$ operating at 100 GHz effectively "breaks" the Chu limit. It is important to note that Chu [27], Wheeler [110], and Harrington [41] formulated the limits on bandwidth, size, and gain under the assumption of a passive antenna. On the other hand, the lasers required to excite the atoms to the Rydberg state are active and require a substantial amount of DC power. Thus, this limit cannot be considered the standard for analyzing electrically-small Rydberg receivers.

A dipole antenna presents a capacitive impedance at the port that connects the antenna to the receiver. To match, a negative capacitance can be used, which is accomplished through the introduction of an active circuit. This is a viable option for analysis, but it is still difficult to establish which components are active for a Rydberg receiver. Therefore, it becomes necessary to identify a figure of merit for Rydberg receivers

as electrically-small antennas.

5.3 S-band Optical Set-Up

Detecting low-frequency electric fields using Rydberg-atom sensors typically requires strong optical power from the coupling laser to access the desired Rydberg transition. When coupling laser power is limited, direct excitation of the sensing state may not be achievable. To overcome this limitation, we implement a multi-step excitation scheme that uses a high-frequency microwave transition to access a nearby Rydberg state that couples to the desired low-frequency transition. This effectively allows low-frequency sensing while reducing the optical power requirements of the coupling laser. This is shown in Fig. 5.5. The excitation pathway used in this work consists of four sequential transitions. A probe laser at 780.24 nm drives the $5S_{1/2} \rightarrow 5P_{3/2}$ transition in ^{87}Rb. A coupling laser near 480 nm then excites atoms to the Rydberg state $34D_{5/2}$. A high-frequency microwave field at 61.3246 GHz couples this state to $33F_{7/2}$, creating an intermediate splitting state. Finally, a low-frequency electric field at 2.275 GHz drives the $33F_{7/2} \rightarrow 33G_{9/2}$ transition, which acts as the sensing transition. From here, measurements can be taken from this sensor in a configuration without a local oscillator (electrometer) and with local oscillator (receiver).

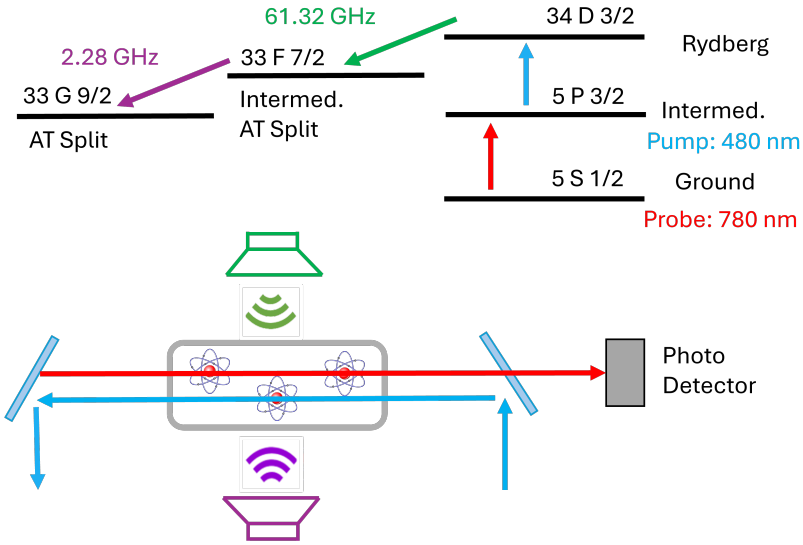


Figure 5.5: The excitation scheme for a high frequency to low frequency RF transition. This layout assumes no local oscillator.

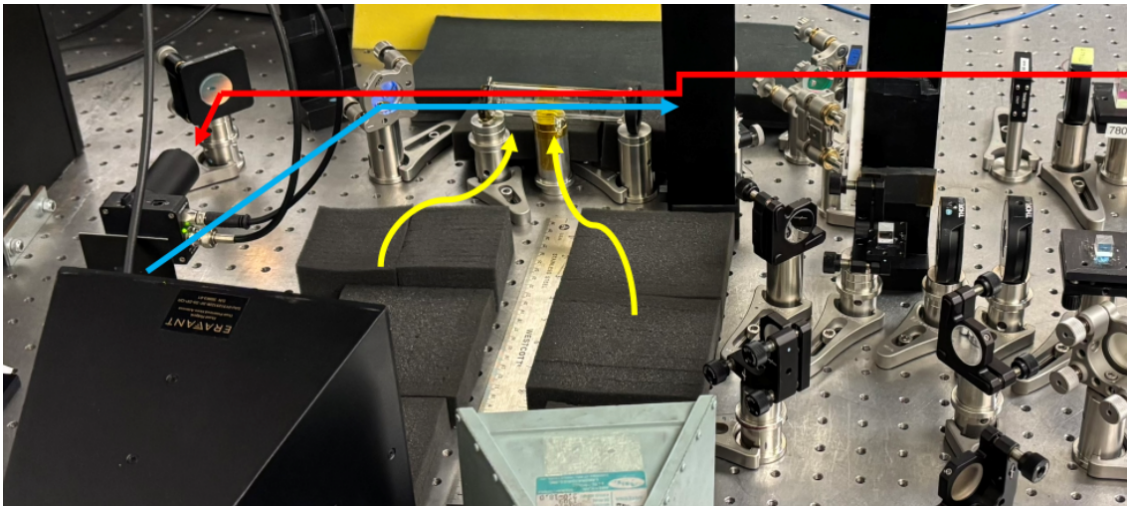


Figure 5.6: The low-frequency Rydberg-atom receiver, mounted to an optical table. The blue and red arrows show the path of the probe and coupling lasers, counterpropogating. The red laser is ultimately read out on a photodetector, indicated by the red arrow. The electric field from the source (gray horn) and the interferer (black horn) are indicated by yellow arrows. A V-band horn antenna (not shown) provides the intermediate microwave transition that couples the initial Rydberg state to the splitting state.

The probe laser (780 nm) consists of a Vescent laser head, saturated absorption spectroscopy system, and control system. The coupling laser ($\approx$ 480 nm) is a Toptica DL pro laser with associated control module. The probe laser is set to the proper wavelength (780.24 nm) associated with the rubidium-87 D2, F=2 to F'=3 transition. This is confirmed using confirmed using saturated absorption spectroscopy. The resulting frequency stability is on the order of a few MHz over several minutes, sufficient to maintain stable EIT conditions. The probe laser optical power is 135 μW, and the coupling laser power is 25.46 mW at the cell, with both lasers less than 1.5 mm in diameter. The probe laser drives the $5S_{1/2} \rightarrow 5P_{3/2}$ transition. The coupling laser scans across a wavelength range centered on 481.43 nm when in the electrometer configuration, and is set to the center wavelength in the receiver set-up. In both cases, it excites the atoms to the Rydberg state at $34\mathrm{D}_{5/2}$. The probe and coupling beams are spatially overlapped within the vapor cell using dichroic mirrors and aligned to counter-propagate along a common optical axis.

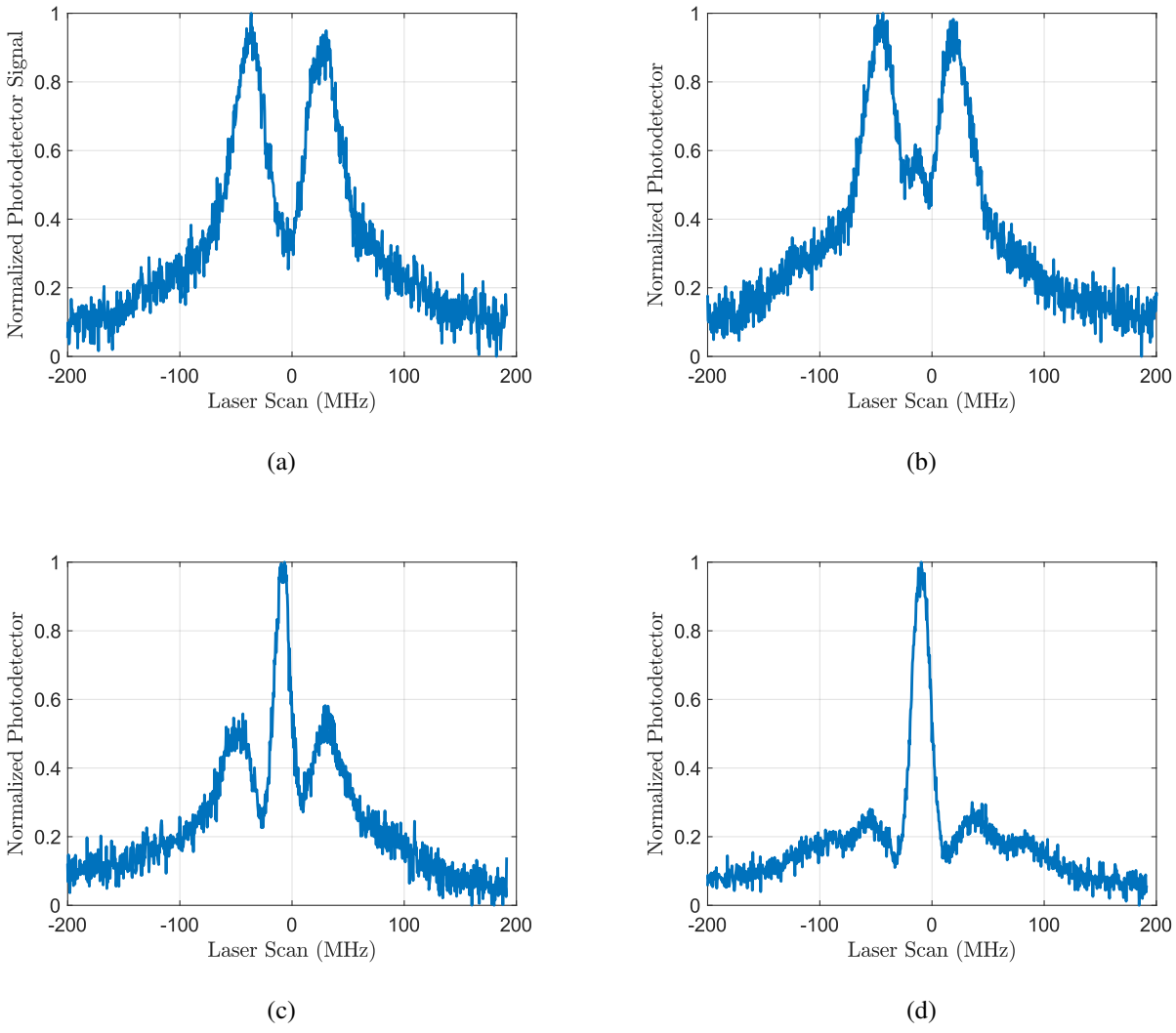


Figure 5.7: AT splitting for the low-frequency energy transition as a function of the power from the 2.28 GHz source. This progression of powers shows the low frequency energy level splitting from an AT splitting peak generated by the V-band source. Then, with more power, this becomes the dominant peak. The progression in power is (a) at -2 dBm or 0.69 V/m, (b) at 3 dBm or 1.22 V/m, (c) at 12 dBm or 3.46 V/m, and (d) at 17 dBm or 6.16 V/m.

The beam diameters are approximately 1.5 mm. The overlap region defines the active sensing volume where electromagnetically induced transparency (EIT) occurs. Vertical polarization for both lasers is set using polarizing beam splitters and half-wave plates prior to entering the vapor cell. The beams are co-polarized

to maximize coupling strength for the selected Rydberg transitions. The vapor cell is a ThorLabs 8 cm long and 2.5 cm diameter cell made of quartz glass and filled with natural abundance rubidium. The output of the red laser is read from a photodetector, and the output is recorded using a digital oscilloscope and processed in MATLAB for analysis. All measurements are conducted at room temperature. A signal generator (Keysight E8257D) provides the 61 GHz microwave field used as the intermediate splitting state. This is transmitted to the vapor cell using a V-band horn antenna 40 cm away from the cell, with WR15 feed and a measured gain of 23 dBi. The path from the signal generator to the horn includes 6 dB of loss from cables and adaptors. Separately, a broadband horn antenna (CAES H-1734) with gain 10 dBi in the low-frequency regime, transmits the 2.28 GHz frequency about 50 cm away. Both RF sources are linearly polarized and aligned such that their electric fields are co-polarized with the lasers. The antennas are placed sufficiently far from the vapor cell to approximate far-field plane-wave excitation.

First, we demonstrated the viability of exciting the atoms to a low-frequency transition via an intermediate, high-frequency state provided by RF excitation. Other literature sources have used similar techniques to reach lower frequencies [12] [1], though our specific excitation has not been targeted before. Initially, with just lasers and the V-band source transmitting at about 10 dBm, we observe high-frequency AT splitting. Then, the secondary, S-band source is turned on, initially at -2 dBm at the source. The output on the photodetector is shown in Fig. 5.7a, where the presence of the low-frequency field perturbs the Autler–Townes splitting produced by the V-band excitation, resulting in broadening of the higher-frequency peak. As power is increased to 3 dBm, corresponding to a field value of 1.22 V/m, the small, low-frequency peak distinguishes from the high-frequency separation, seen in Fig. 5.7b. With additional power, on the order of 6.16 V/m, resolution of the low-frequency peak improves as its field strength is greater than that of the existing split. As the S-band field strength increases, the coupling between the $33F_{7/2}$ and $33G_{9/2}$ states increases, producing an additional splitting that eventually dominates the spectral response.

Finally, at 17 dBm or a field of 6.16 V/m, the low-frequency peak has become the dominant value, in Fig 5.7d. Note that in this configuration, it is no longer possible to recover field information from AT splitting; even though this low-frequency transition is on-resonant, once the low-frequency coupling becomes comparable to or larger than the V-band induced splitting, the spectral features no longer correspond

uniquely to a single electric-field amplitude. As a result, the AT peak spacing cannot be directly used to extract the field strength of either signal. Nevertheless, the electrometer-measured waveform is useful for identifying interference and distortion, and can be combined with a local oscillator to make a low-frequency receiver.

5.4 Isolation from Interferors - Electrometer

The instantaneous bandwidth of Rydberg receivers is limited to a maximum of 10 MHz due to atomic population dynamics [44]. Strong long-range interactions mean the excitation of one atom can prevent the excitation of nearby atoms, referred to as the "Rydberg blockade". Though this bandwidth limitation restricts the usage of Rydberg-atom receivers for communications purposes, this also confers the benefit of acting as a high-Q filter for the receiver, therefore improving its selectivity. With a V-band intermediate electric field of 21 V/m, the low-frequency splitting state field of approximately 1 V/m, and no local oscillator, the electrometer measurement with and without an interferer is shown in Fig. 5.8. For these measurements, the interferer is a signal that is offset from the frequency of choice by 100 kHz, at a power of 20 dBm (6.91 V/m), and its source is adjacent to the transmitting signal in space, as shown in Fig. 5.6. Though a definitive field measurement cannot be extracted from this data, it is evident that the resolution of the main tone is highly degraded in the presence of an interferer, to the order of the much weaker V-band energy state.

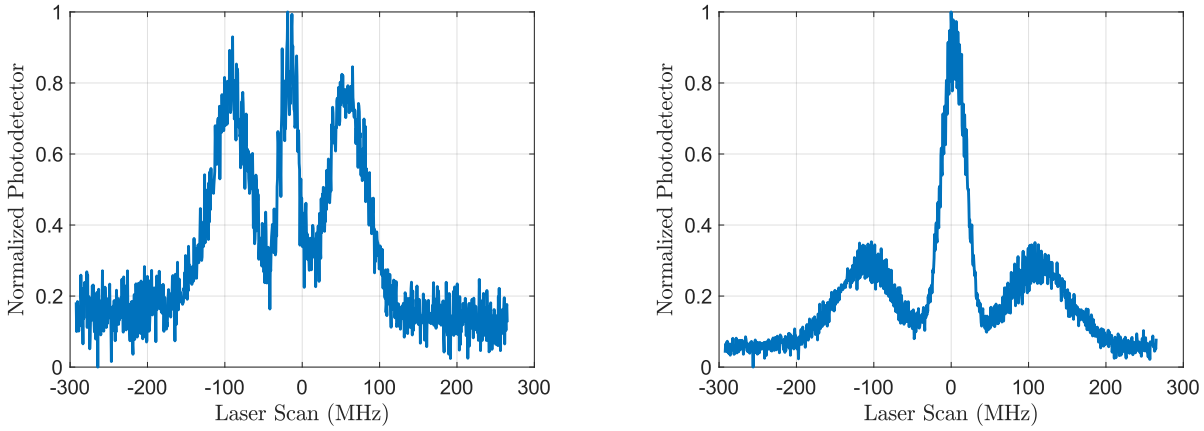


Figure 5.8: Electrometer measurement of the low-frequency receiver, with (left) and without (right) the presence of an interferor at 8.70 V/m, 100 kHz offset from the low-frequency tone of choice.

5.5 Isolation from Interferors - Receiver

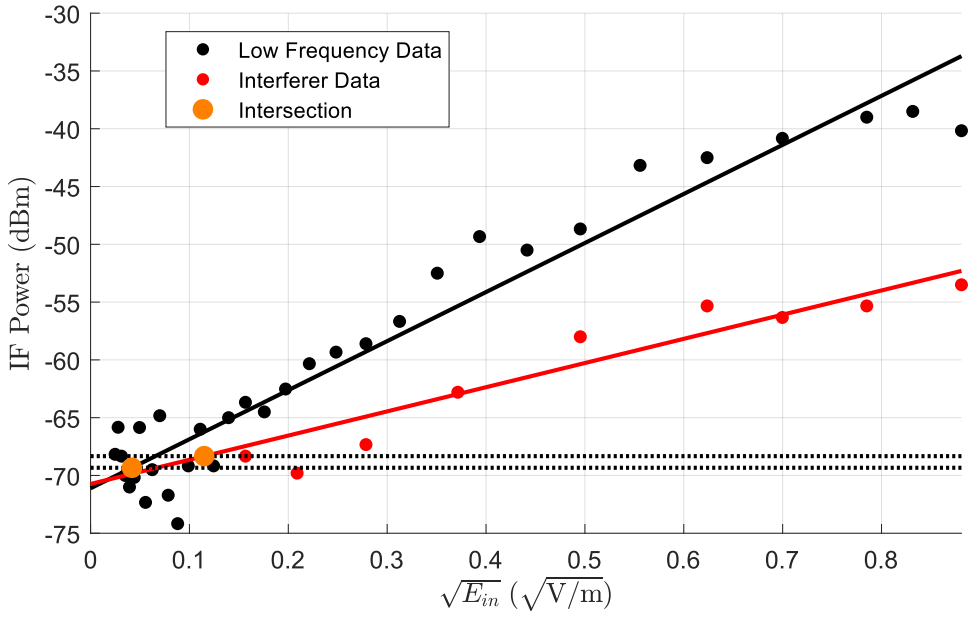


Figure 5.9: Sensitivity of receiver in free space versus with an interfering signal 100 kHz from the main signal, at a power of 20 dBm, approximately co-located with the source.

To operate the system as a receiver, a local oscillator (LO) field is introduced at a frequency offset of 100 kHz from the transmitted signal. The LO is transmitted at approximately the same power level as the signal field. Due to limited table space, precluding the use of another horn antenna, the local oscillator field is transmitted through the same horn antenna as the low-frequency electric-field intended for sensing, using a combiner. In this configuration, the Rydberg atoms act as a nonlinear mixing element. The signal electric field E_{RF} and local oscillator field E_{LO} simultaneously couple the $33F_{7/2} \rightarrow 33G_{9/2}$ transition, producing a beat signal at the difference frequency between the two RF tones. This heterodyne mixing process transfers the RF frequency difference to the optical domain, where it modulates the probe transmission detected by the photodetector. The resulting optical signal oscillates at the intermediate frequency (IF) of 100 kHz and can be directly measured on a spectrum analyzer.

To characterize the sensitivity of the receiver, the input power of the low-frequency electric field is gradually reduced while maintaining a fixed local oscillator amplitude. The photodetector output is recorded on a spectrum analyzer, and the amplitude of the 100 kHz beat note is measured as a function of the transmitted signal power. Sensitivity is defined here as the minimum detectable signal power that produces a spectral peak distinguishable above the system noise floor. The measured sensitivity of the low-frequency Rydberg-atom receiver, both with and without the presence of an interfering signal, is shown in Fig. 5.9. The black points and trace correspond to the receiver operating in free space without interference. Under these conditions, the receiver can resolve an electric field on the order of 0.001 V/m at the location of the vapor cell. This limit is determined primarily by a combination of photon shot noise, photodetector noise, and fluctuations in the EIT resonance.

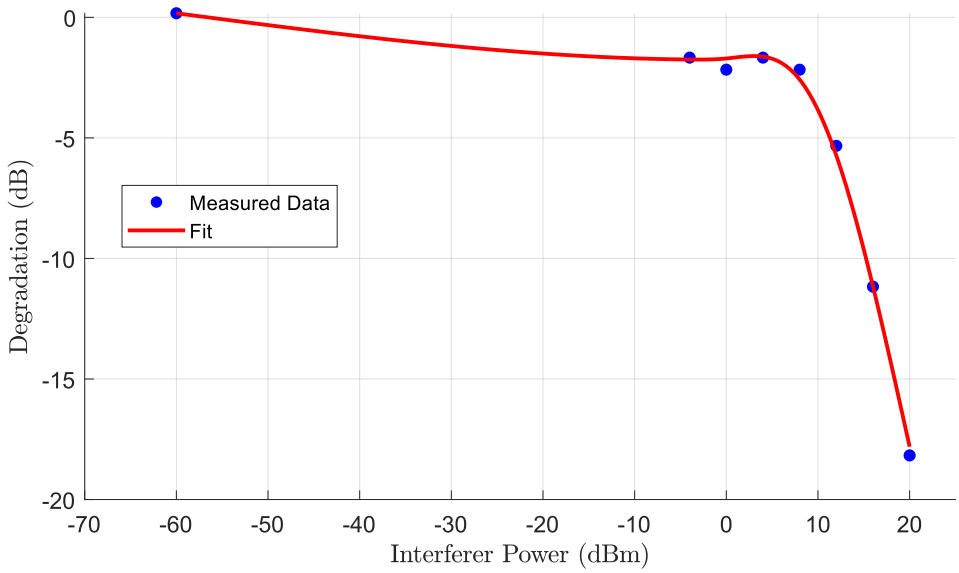


Figure 5.10: Degradation in receiver sensitivity as a function of interferer signal power.

When an interfering signal is introduced, the receiver sensitivity is degraded. In this topology, the interferer transmits at 20 dBm (6.91 V/m) and is offset by 100 kHz from the signal frequency while being approximately co-located with the signal source. The presence of this additional field raises the effective noise floor of the receiver to approximately -55 dBm. This degradation occurs because the interferer also mixes with the local oscillator field within the atomic medium, generating additional beat components that broaden the detected spectral response and increase the background noise level at the intermediate frequency. Importantly, the reduction in sensitivity does not scale linearly with the power of the interfering signal. Instead, the effect depends on both the interferer amplitude and its frequency separation from the signal of interest. Because the Rydberg-atom receiver behaves as a narrowband detector, fields that fall within the effective atomic bandwidth can strongly perturb the EIT resonance and the associated mixing process. As a result, interferers close in frequency to the desired signal produce a significantly larger degradation in sensitivity than those located further from the center frequency. This dependence on interferer proximity is examined further in Fig. 5.10 and Fig. 5.11.

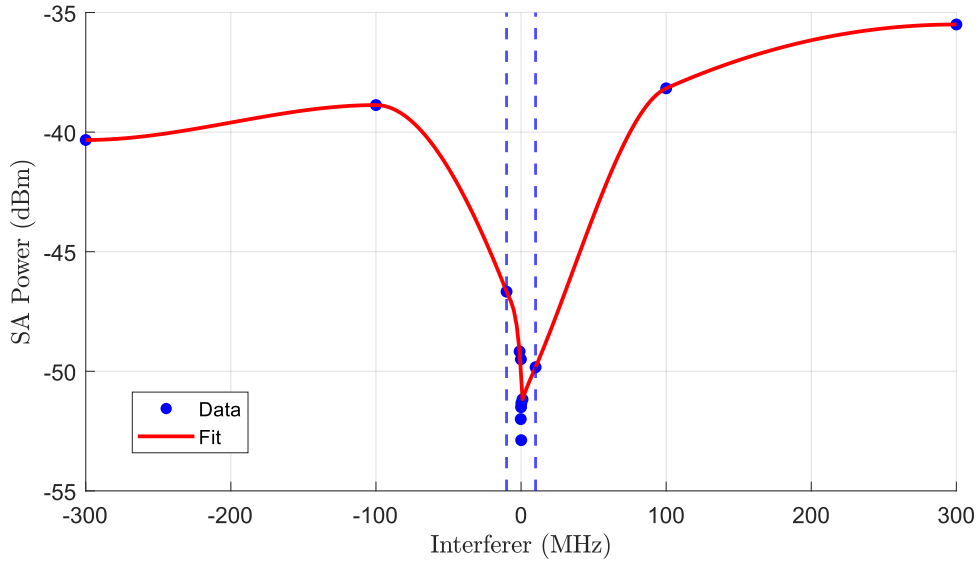


Figure 5.11: Sensitivity of the receiver in the presence of an interfering signal transmitted at 20 dBm while the interferer frequency is swept relative to the desired field. Clear degradation in sensitivity as a function of interferer frequency is observed.

In Fig. 5.10, it is evident that an interferer with a stronger electric field produces a greater reduction in receiver sensitivity. As the interferer amplitude increases, the undesirable electric field interacting with the Rydberg transition perturbs the combined RF-LO fields that form the beatnote. However, it is noteworthy that this degradation, while still measurable, becomes significantly less pronounced once the amplitude of the interferer approaches that of the local oscillator field.

The dependence of receiver sensitivity on interferer frequency is shown in Fig. 5.11. In this measurement, the interfering signal (20 dBm) is transmitted while its frequency is swept across the signal band. The resulting sensitivity is plotted as a function of frequency offset of the interferer from the desired signal. Because the selectivity of the Rydberg-atom receiver is governed by atomic response time, the effective detection bandwidth is limited to approximately 10 MHz. Extraneous electric fields that fall within this atomic bandwidth strongly perturb the EIT resonance and therefore are expected to produce noticeable degradation in receiver sensitivity.

The vertical markers in Fig. 5.11 indicate a conservative 20 MHz interference region centered on

the low-frequency electric field. Within this region, interfering signals are expected to significantly perturb the Rydberg receiver because they fall well within the effective atomic detection bandwidth. However, the measurements reveal that noticeable degradation persists even at much larger frequency offsets, extending to greater than 100 MHz. This behavior indicates that the receiver remains sensitive to strong out-of-band fields, even when they exist outside the nominal atomic bandwidth. An additional feature of Fig. 5.11 is the asymmetry between positive and negative interferer frequency offsets. This asymmetry arises from the relative frequencies of the RF signal and the local oscillator used for heterodyne detection. In the experiment, the desired RF signal E_{RF} is set to 2.2871,GHz while the local oscillator field E_{LO} is set to 2.2872,GHz, producing the intended intermediate frequency of 100 kHz. The interferer frequency is swept relative to the local oscillator frequency, meaning that an interferer offset of 0 MHz corresponds to transmission at 2.2872 GHz, coincident with the LO.

Because the interferer frequency is referenced to the LO, small negative offsets shift the interferer toward the desired RF signal frequency. For example, an interferer offset of -100 kHz places the interferer at 2.2871 GHz, which is identical to the signal frequency. Under these conditions the interferer directly overlaps the transition driven by E_{RF} and strongly perturbs the atomic response, leading to a pronounced degradation in receiver sensitivity. Alternatively, small positive interferer offsets move the interfering signal further away from the desired RF frequency while remaining near the LO frequency. In this regime the strong local oscillator field continues to dominate the atomic mixing process and effectively stabilizes the heterodyne detection pathway. As a result, the LO field partially mitigates the impact of the interferer on the detected beat signal. This difference in how the interferer couples to the RF–LO mixing process leads to the observed asymmetric degradation in sensitivity between positive and negative frequency offsets.

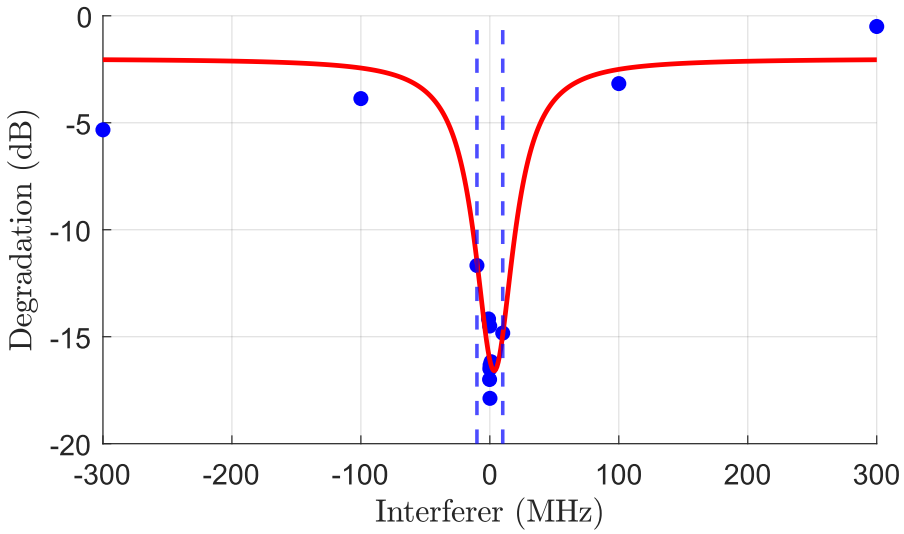


Figure 5.12: Sensitivity of the receiver in the presence of an interfering signal transmitted at 20 dBm while the interferer frequency is swept relative to the desired field. Clear degradation in sensitivity as a function of interferer frequency is observed.

Using a Lorentzian fitting function with the data collected in Fig. 5.11, we can compare the performance of the Rydberg-atoms to a standard microwave filter, as shown in Fig. 5.12. From fitting, we see that the atoms have a 36.5 MHz response region using the full-width half maximum (FWHM). For a RF frequency of 2.2 GHz, this represents a fractional bandwidth of 1.66%, which is considered a typical bandwidth in comparison to conventional filter counterparts. [87]

5.6 Polarization Impact

Polarization measurements were conducted by rotating the signal horn antenna relative to the receiving antenna in order to create a polarization mismatch. In this configuration, the signal horn was the one rotated, while the horn supplying the LO was fixed. The E_{RF} was set to 2.2871 GHz with 1 dBm output power (0.98 V/m). The E_{LO} was set to 2.2872 GHz with 1 dBm output power (0.78 V/m). When the antennas were aligned with 0° polarization mismatch (co-polarized), the measured received power was -37.5 dBm. Rotating the transmitting antenna to 45° reduced the received power to -46.67 dBm, and further rotation to

90° resulted in a received power of -52.00 dBm. These results demonstrate the expected decrease in received signal strength as the polarization mismatch between the antennas increases. However, the measurement is not entirely lost, indicating that the receiver is tolerant of some degree of polarization mismatch between E_{RF} and E_{LO}.

In this chapter, we demonstrated two sensors: a millimeter-wave Rydberg electrometer operating at 61.32 GHz and a receiver operating at 2.2 GHz. In the V-band section, we systematically investigated the effects of RF power and polarization on sensor performance. The measured Autler-Townes splitting shows good agreement with theoretical field predictions at moderate power levels, while deviations at low and high fields are attributed to linewidth limitations and power broadening, respectively. Polarization mismatch was shown to degrade both field magnitude and resolution, highlighting the importance of precise field alignment in Rydberg-atom sensors. To the best of the authors' knowledge, this is the first demonstrated V-band room-temperature Rydberg atom sensor.

In the S-band section, we demonstrated an uncommon RF excitation scheme that enabled the receiver to operate at low frequencies, despite having a limitation on the optical power. Additionally, we demonstrated the impact of an interferer on the sensor, in both electrometer and receiver configurations. For the electrometer, the impact is qualitative; there is observed degradation in the readout, but the RF excitation technique limits the extraction of numerical data from this set-up.

Chapter 6

Conclusions and Future Work

6.0.1 Thesis Summary

In summary, this thesis investigates engineeering aspects of Rydberg-atom microwave electrometers and receivers in the frequency range from around 2 GHz to 60 GHz. Several X-band experiments show that the inferior sensitivity of Rydberg-atom receivers compared to standard LNA-based electronic receivers can be overcome with narrowband passive field-enhancing three-dimensional circuits. Further, a multi-frequency enhancing circuit is demonstrated for the first time with a direct detection scheme that addresses several Rubidium transitions in the 10-GHz frequency range. In a millimeter-wave sensor around 61 GHz, effects of microwave components are examined, including polarization sensitivity. The 61-GHz wave is then used to enable the Rydberg atoms to reach a lower-frequency transition around 2 GHz, where the effect of an interfering wave at a frequency close to the received signal frequency is examined.

6.1 Future Work

6.1.1 GaAs Microwave LO for Heterodyne Rydberg-Atom Receiver

In a microwave receiver, both phase and magnitude of an incident modulated electromagnetic field are recovered. As discussed earlier in the thesis, a Rydberg-atom sensor can be a heterodyne receiver with the addition of microwave LO field, or possibly with an optical LO [50]. In the microwave heterodyning case, the LO wave is radiated by an antenna, e.g. [21] [39]. While using a second horn antenna and a plane-wave source to test the heterodyne receiver properties is acceptable for investigations in the lab, in

practice the LO needs to be more integrated. Future work will involve integration of the LO within the sensitivity enhancement circuit.

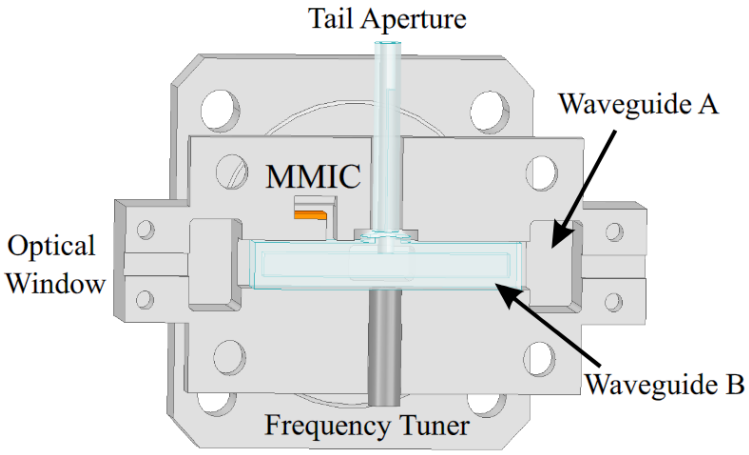


Figure 6.1: A cross-section of the resonant cavity holding the vapor cell full of Rubidium atoms. The tail of the fused silica vapor cell is much longer than the width of the waveguide cavity, so an aperture is cut within the cavity to accommodate the tail. The local oscillator (shown in orange) couples into the waveguide by capacitively loading the glass on a side wall of the vapor cell.

Fig. 6.1 shows a possible LO integration strategy, where a MMIC oscillator output is capacitively coupled through the glass wall of the vapor cell within a waveguide resonator field enhancing structure, such as the ones shown in previous Chapters. By coupling the RF output of the MMIC to the vapor cell, through a coupling structure, the LO signal interacts with the Rubidium atoms in the vapor cell, providing mixing with the input RF signal.

The resonator is approximately $40 \times 30 \times 20$ mm in size. On the backside of the resonator shown in Fig. 6.1, a WR-62 rectangular waveguide feed inputs the RF signal. The resonant cavity itself contains the fused silica vapor cell that is filled with Rubidium atoms. The resonant cavity is composed of three waveguide sub-sections, waveguide A that is $15.7988\,\text{mm} \times 7.8994\,\text{mm} \times = \lambda_g/4$. At this frequency, $\lambda_g \approx 4.6\,\text{mm}$. Between two sections of waveguide A is waveguide B, with dimensions $6.5\,\text{mm} \times 4.318\,\text{mm} \times 25$ mm. The purpose of waveguide B is to operate near cut-off frequency, and therefore appear electrically

short with high field uniformity. The resonator also has a aperture to fit the vapor cell tail. Optical windows are also inscribed on the left and right sides of the resonator to allow the laser beam to pass through and excite the Rubidium atoms.

Next, the design and measurements of an example GaAs MMIC local oscillators for such cavity-enhanced 11.369 and 15.095 GHz transitions of the Rb atom is shown. These transitions are achievable after excitation with a red laser at 780.24150 nm, and a blue laser with a wavelength of 479.87353656 nm (at 11.369 GHz) or 480.0426104 nm (at 15.095 GHz). A block diagram of the setup with a MMIC LO is shown in Fig. 6.2, where a MMIC LO is directly integrated with the Rydberg atom sensor. Since the Rydberg transitions have very high selectivity, some tunability is required, so the oscillators are designed to be voltage-tuned.

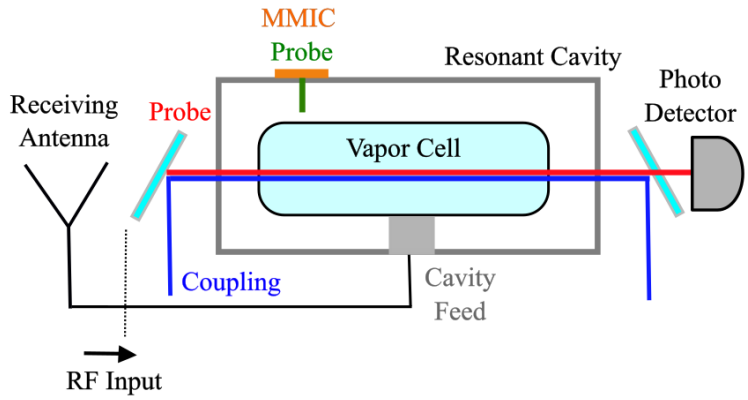


Figure 6.2: A Rydberg receiver, composed of a Rubidium vapor cell embedded in a resonant cavity, excited with two lasers. The oscillator is placed on the exterior of the resonant cavity, and coupled to the vapor cell using a probe. This paper focuses on the design of the LO in GaAs, specifically for a Rubidium receiver using metallic waveguide cavity enhancement for the 11.369 and 15.095 GHz transitions.

The specifications of the two oscillators are most importantly driven by the specific atomic transitions chosen for the Rydberg atom receiver. These oscillators target the $52D_{5/2}$ and $57D_{5/2}$ transitions, which sets the frequencies to 11.369 and 15.095 GHz respectively. The previous heterodyne demonstrations require a minimum output power of 0 dBm in the vapor cell. One of the key integration elements is ease of coupling to a waveguide cavity, discussed in the last section.

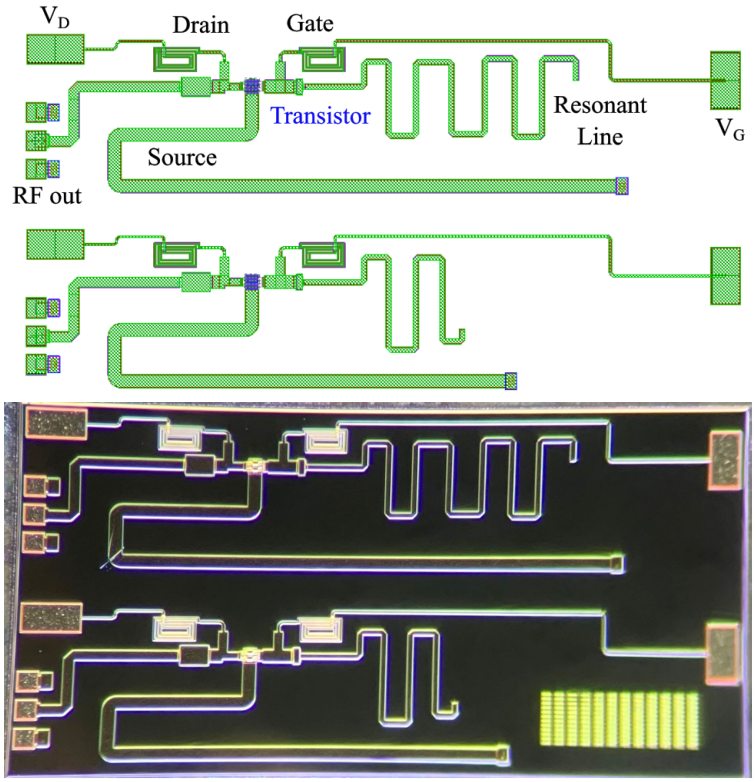


Figure 6.3: (a) MMIC layout using Cadence AWR Microwave Office that shows the two oscillators. The die size is 3.29 mm $\times$ 2 mm. The top circuit is the 11 GHz oscillator, indicated by the longer meandered line on the gate side of the transistor, while the bottom circuit is the 15 GHz oscillator. Both are single-port RF devices, measured using GSG pads on the drain side (left) of the circuit. (b) Photograph of the MMIC with two oscillators having layouts shown above. The RF output (resonant frequency) is measured on the three-pronged GSG probe on the left, while the DC bias is supplied by the DC probes on the left and right of the chip.

The oscillators are designed in the WIN Semiconductors PIH1-10 enhancement mode pHEMT process. This process has 3 metal layers, capacitors and resistors, as well as several pHEMT topologies, which require a single polarity bias. A co-planar waveguide (CPW) transistor layout is chosen since it does not have automatically grounded source terminals, allowing a three-port design where the oscillation condition can be easily controlled. Nonlinear models have been validated for three device sizes: 50 μm, 75 μm and 100 μm, and a 4×50 μm transistor has sufficient output power and is chosen for the design.

A simple topology similar to a Colpitts oscillator is used as a starting point [76]. VCOs have been

implemented in monolithic circuits from S-band to Ka-band with varying phase noise and bandwidth. At 2.4 GHz, other topologies in GaAs HEMT processes exhibit a phase noise of as low as -118.33 dBc/Hz at a 1 MHz offset [68]. In X-band and Ku-band, which are the targeted regions of the two oscillators in this work, typical phase noise values are approximately -110 dBc/Hz at 1 MHz offset [26] [69]. The circuit topology used in this work is a three-port oscillator shown in Fig. A.1(a), where the gate 69-Ω transmission-line open-circuited resonator is 130 electrical degrees long at the oscillation frequency, and determines to first order the oscillation frequency. The 51-Ω source resonator is short-circuited and allows additional smaller adjustments in the oscillation frequency. The simulated harmonic-balance response of the oscillators is shown in Fig. A.2 with the pHEMTs biased at $V_{DD} = 4$ V and $V_{GG} = 1$ V.

The atoms in the vapor cell have a very selective frequency response, on the order of 10 MHz around the transition frequency. Therefore, the oscillators are designed to have some necessary tunability. Lastly, because much of the interest Rydberg measurements concerns high-sensitivity measurements, this local oscillator design aims to minimize phase noise using the low-Q microstrip resonator. It is important to note that the phase noise will improve by coupling with the cavity.

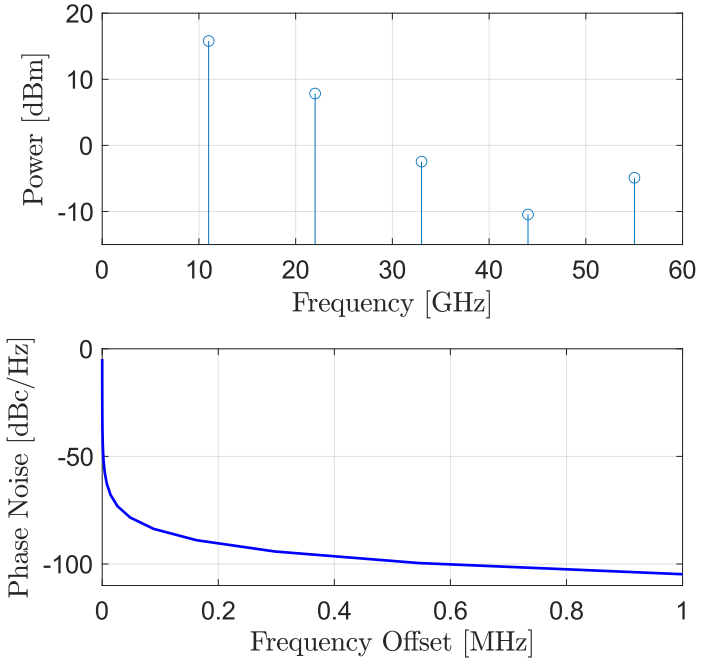


Figure 6.4: The simulated harmonic content and phase noise for the 11 GHz oscillator with bias conditions $V_{DD} = 4\,\text{V}$ and $V_{GG} = 1\,\text{V}$. The first harmonic has a power of 15.79 dBm, the second harmonic of 7.84 dBm, and third harmonic power of -2.45 dBm. The simulated phase noise is $-104.8\,\text{dBc/Hz}$.

The oscillators are measured on-wafer. To measure the output frequency and power, the output of the oscillator is transmitted to a power meter with a 20-dB coupler, with the coupled port monitoring the spectrum using a Rohde & Schwarz FSW43 spectrum analyzer. The resolution bandwidth (RBW) of the analyzer is set to 100 kHz for the measured spectra shown in Fig. A.4. To determine the phase noise, the following equation is used [29]:

$$N = N_0 - 10 \cdot \log(\text{RBW}), \tag{6.1}$$

where N_0 is the direct measurement of the phase noise at 1 MHz offset, and an adjustment factor is applied based on the resolution bandwidth. With biasing conditions $V_{DD} = 3.5\,\text{V}$ and $V_{GG} = 0.5\,\text{V}$, the 11-GHz oscillator had a phase noise of $-109\,\text{dBc/Hz}$ at 1 MHz offset frequency. In simulations, the LO had a phase noise of $-104.8\,\text{dBc/Hz}$, yielding a difference between expected and measurement of 4%. The second oscillator oscillates at $\approx 15.5\,\text{GHz}$ (with $V_{DD} = 4.5\,\text{V}$ and $V_{GG} = 1\,\text{V}$), and a measured phase noise of

-99 dBc/Hz at 1 MHz offset frequency. The simulated value at 15 GHz is -74.3 dBc/Hz, or an improvement of 24.9%. These values do not include a shape correction factor for the resolution bandwidth. The measured power spectrum used for phase noise calculations is shown in Fig. A.4.

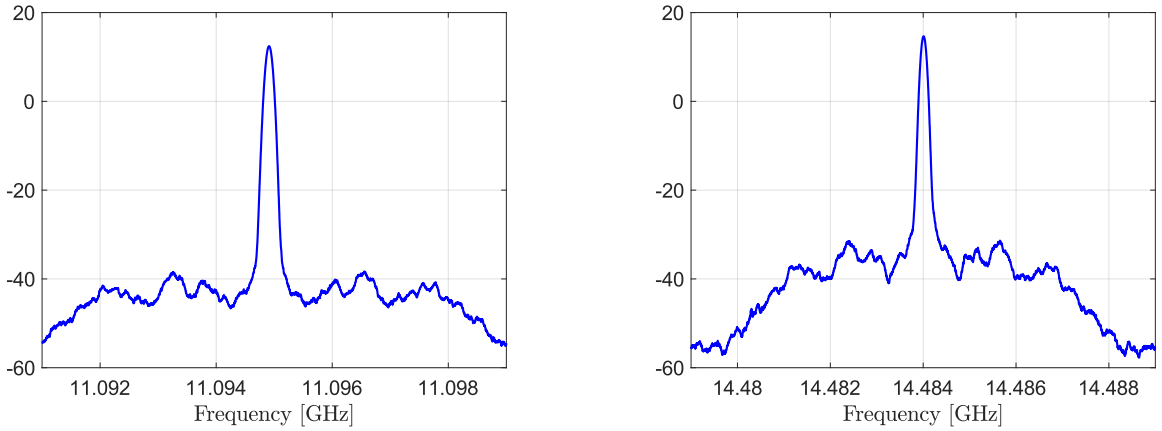


Figure 6.5: (a) Measured output power as a function of frequency for the 11 GHz oscillator, used to determine the phase noise, which was -109 dBc/Hz at 1 MHz offset. This was measured at 11.0949 GHz with bias $V_{DD} = 3.5$ V and $V_{GG} = 0.5$ V. (b) Output power for the 15 GHz oscillator, with a phase noise of -99 dBc/Hz at 1 MHz offset. This was measured at 14.484 GHz with bias $V_{DD} = 5$ V and $V_{GG} = 0.5$ V.

To determine the tuning bandwidth, the drain and gate voltages of each oscillator are swept. Predictably, varying the gate voltage has a larger impact on tuning the frequency than a change in drain voltage. Fig. 6.6 shows the measured tuning with bias voltages for the 11-GHz MMIC. A similar trend for the 15-GHz oscillator is plotted in Fig. 6.7. The gate voltage is 0 – 1 V, while the drain voltage is varied from 0 – 6 V, both in 0.1 V increments. Using the nominal biasing conditions ($V_{DD} = 4$ V, $V_{GG} = 0.5$ V), the lower-frequency circuit oscillates at 11.103 GHz with a 54-MHz tuning range from 11.084 – 11.138 GHz. The oscillator designed for 15 GHz oscillates at 14.813 GHz at $V_{GG} = 0.9$ V and $V_{DD} = 2$ V with a total tuning range of 14.476 – 14.822 GHz, or 346 MHz of tuning.

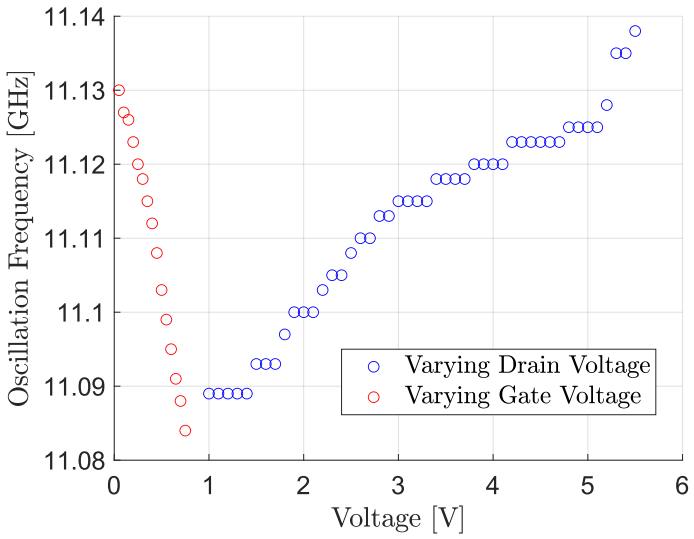


Figure 6.6: A plot of the oscillation frequency versus change in voltage at 11 GHz. Each point on the plot corresponds to a discrete measurement of a changing drain (blue) or gate (red) voltage. When the gate voltage was swept, the drain was fixed to 4 V. When the drain is swept, the gate is set to 0.2 V.

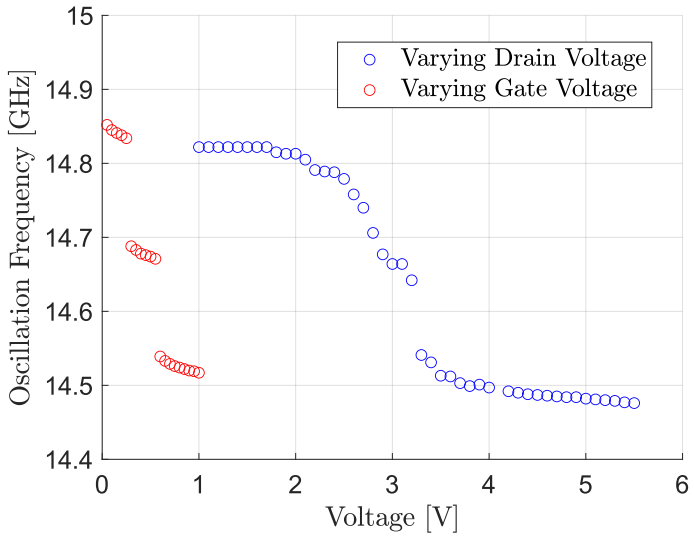


Figure 6.7: A plot of the oscillation frequency versus change in voltage at 15 GHz. When the gate voltage is swept, the drain is fixed to 4 V. When the drain is swept, the gate is set to 0.9 V.

In conclusion, this section presents the design and development of two voltage-controlled oscillators

(VCOs) that can be used in quantum receivers operating at 11 GHz and 15 GHz. The VCOs are implemented as monolithic microwave integrated circuits (MMICs) manufactured in the WIN Semiconductor GaAs HEMT process. The experimental measurements of the designed oscillators demonstrate their performance. The 11 GHz oscillator exhibits a measured phase noise of -109 dBc/Hz at 1 MHz offset and a tuning range of 54 MHz. The 15 GHz oscillator has a measured phase noise of -99 dBc/Hz at 1 MHz and a bandwidth of 346 MHz. The measurements are compared to simulation results, showing reasonable agreement with some deviations. Future work includes integration into a Rydberg optical set up and detailed design of the coupling structure. Although there is only a 3% difference in frequency from the simulation for the 11 GHz MMIC, the tuning is not sufficient to shift the frequency to the $52D_{5/2}$ transition. However, other close transitions exist for Rubidium, the $69P_{3/2}$ transition at 11.14 GHz. In the case of the 15-GHz design, the shift is more significant (about 10%), and this oscillator would be suitable for the $63P_{3/2}$ transition at 14.82 GHz.

6.1.2 High Frequency Enhancement

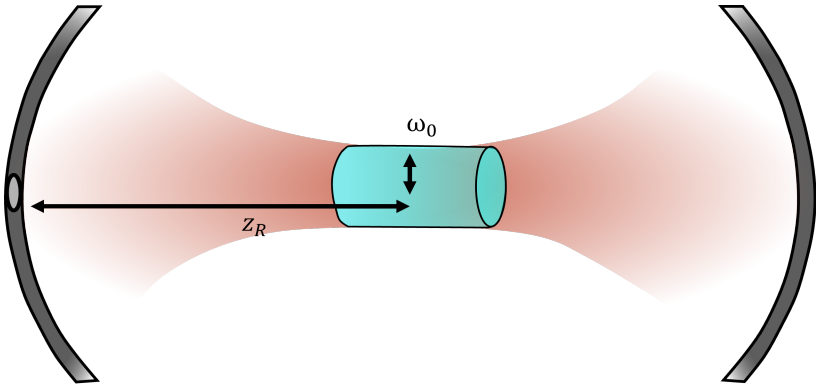


Figure 6.8: A Gaussian beam set-up, constructed from two concave parabolic mirrors. The resonator is fed through the center of one mirror, resulting in a beam of minimum beamwidth of ω_0 and a Rayleigh range of z_R. The vapor cell is placed in the center and determines the necessary size of the beam.

The previously discussed enhancement methods, such as parallel plates or metallic waveguide resonators, are not viable for Rydberg receivers at millimeter-wave frequencies. Lumped elements no longer perform

as modeled at high frequencies, and waveguide components decrease in size so that they cannot contain a vapor cell. Instead, we propose the use of a Gaussian beam for enhancing the field seen by the Rydberg atoms. A Gaussian beam is a concentrated beam of electromagnetic radiation, where the envelope of the beam is a function of the propagation distance off the resonator's surface. The resonant structure ensures that the same power occupies a smaller effective cross section, so the electric field becomes larger compared to the free-space case. A picture of a possible Gaussian beam resonator is shown in Fig. **??**.

To show the field-enhancing potential of the Gaussian beams, we can compare the amplitude of an electric field in the beam and in free space. In free space, the power density at distance r is:

$$S_{\text{free}} = \frac{P_{\text{ant}} G}{4\pi r^2} = \frac{E^2}{2\eta_0} \tag{6.2}$$

where P_{ant} is the available transmitted power, G is the transmitting antenna gain, and $\eta_0 \approx 377\ \Omega$ is the impedance of free space. Re-arranging to solve for the electric field:

$$E_{\text{free}} = \frac{\sqrt{60 P_{\text{ant}} G}}{r}. \tag{6.3}$$

where we can apply this to the parameters used in the set-up above, where $P_{ant} = 11$ dBm and $G = 23$ dBi, and $r = 0.92$ m. This yields a peak electric field of $E_{free} = 9.36$ V/m. We can compare this field to that of the one contained inside the beam.

The Rayleigh range is the distance along the propagation direction of a Gaussian beam from the point of generation, to the point where the envelope is minimized, called the beam-waist. The Rayleigh range z_R is:

$$z_R = \frac{\pi w_0^2}{\lambda} \tag{6.4}$$

where w_0 is the beam-waist radius and λ is the wavelength. The Rayleigh range identifies the distance that two concave mirrors must be placed from each other in order to form a Gaussian beam of waist w_0. The on-axis peak intensity in a beam, additionally re-arranged for total power, is:

$$I_0 = \frac{2P}{\pi w_0^2} \quad \text{and} \quad P = \frac{\pi w_0^2}{2} I_0 \tag{6.5}$$

Using the intensity relation written in terms of the electric field,

$$I = \frac{1}{2} c\varepsilon_0 E^2 \tag{6.6}$$

$$E_{\text{beam}} = \sqrt{\frac{4P_{\text{beam}}}{\pi w_0^2 c\varepsilon_0}}. \tag{6.7}$$

With the values from our V-band set-up utilized, including a beam waist of 4 cm corresponding to a vapor cell that is 7.62 cm long, the electric field is $E_{beam} = 74.84$ V/m.

Now both quantities are expressed as electric field amplitudes:

$$[E_{\text{beam}} \approx 74.84 \text{ V/m}, \qquad E_{\text{free}} \approx 9.36 \text{ V/m}.$$

]

The enhancement factor is therefore

$$\frac{E_{\text{beam}}}{E_{\text{free}}} \approx \frac{74.84}{9.36} \approx 7.99.$$

This shows that the peak electric field at the beam waist is about eight times larger than the peak electric field in free space at the same distance. This is because the resonant Gaussian mode confines the power to a much smaller effective cross-sectional area than free-space propagation. It should be noted that this enhancement factor is an upper bound on the system, and does not account for losses from the mirror surface, spillover from the mirror, and ideal coupling of all radiated power into the Gaussian mode.

In order to achieve enhancement through a Gaussian beam resonator, two concave aluminum mirrors should be placed with their reflective surfaces facing inward and separated by a distance of $2z_R$, where z_R is the Rayleigh range corresponding to the desired beam waist. This should match the interaction length of the cell. The resonator is excited by an antenna located at the vertex of one mirror, enabling coupling into the fundamental Gaussian mode. The mirror diameter impacts the the confinement of the beam, as an insufficient radius would lead to spillover of the beam and therefore reduced enhancement.

6.1.3 Thesis ContributionsConclusions

This work has demonstrated that sensitivity enhancement is a viable and effective approach for improving the performance of Rydberg-atom microwave receivers, enabling them to achieve sensitivities that approach those of their conventional counterparts. Through the development and implementation of resonant structures in Rydberg-atom receivers, this thesis shows sensitivity enhancement ranging from a factor of 1.5 to 14 depending on frequency and tunability of the resonator. A key contribution of this work is the first demonstration of a frequency-tunable waveguide cavity for on-resonant enhancement, enabling operation across multiple Rydberg transitions at X-band.

This thesis also shows the first demonstration of a Rydberg-atom electrometer in the V-band, expanding upon the frequency ranges currently documented in the literature. This shows the viability of Rydberg-atom sensors in the high-frequency, millimeter-wave regime, where conventional electronics face increasing challenges due to noise and design limitations. Through the V-band electrometer, we showed the importance of RF characterization in optimizing Rydberg receiver performance. Aspects such as the limitations of sensing at certain field strengths, as well as the impacts of polarization mismatch, are measured and characterized. Despite their inherently narrow-band and highly selective response, Rydberg-atom receivers are shown to be susceptible to interference near the carrier frequency. The analysis presented here provides new insight into the ability of Rydberg-atom receivers to reject external interferers.

Overall, this thesis advances the understanding of Rydberg-atom microwave electrometers and receivers by: (1) establishing microwave enhancement with resonant cavities as a practical method for sensitivity improvement, (2) demonstrating new frequency regimes of operation, (3) and providing RF characterization of these receivers.

Bibliography

[1] Gianluca Allinson, Matthew J. Jamieson, Andrew R. Mackellar, Lucy Downes, C. Stuart Adams, and Kevin J. Weatherill. Simultaneous multiband radio-frequency detection using high-orbital-angular-momentum states in a rydberg-atom receiver. Phys. Rev. Res., 6:023317, Jun 2024.

[2] G. Alzetta, A. Gozzini, L. Moi, and Gaspar Orriols. An experimental method for the observation of rf transitions and laser beat resonances in oriented na vapour. Il Nuovo Cimento B, 36:5–20, 11 1976.

[3] D. A. Anderson et al. A vapor-cell atomic sensor for radio-frequency field detection using a polarization-selective field enhancement resonator. Applied Physics Letters, 113(7):073501, 2018.

[4] D. A. Anderson, S. A. Miller, G. Raithel, J. A. Gordon, M. L. Butler, and C. L. Holloway. Optical measurements of strong microwave fields with rydberg atoms in a vapor cell. Physical Review Applied, 5(3), mar 2016.

[5] Darmindra Arumugam, Jun-Hee Park, Brook Feyissa, Jack Bush, and Srinivas Prasad Mysore Nagaraja. Remote sensing of soil moisture using rydberg atoms and satellite signals of opportunity. Scientific Reports, 14, 2024.

[6] S. H. Autler and C. H. Townes. Stark effect in rapidly varying fields. Phys. Rev., 100:703–722, Oct 1955.

[7] K. M. Backes, P. K. Elgee, K.-J. LeBlanc, C. T. Fancher, D. H. Meyer, P. D. Kunz, N. Malvania, K. L. Nicolich, J. C. Hill, B. L. Schmittberger Marlow, and K. C. Cox. Performance of antenna-based and rydberg quantum rf sensors in the electrically small regime. Applied Physics Letters, 125(14):144002, 09 2024.

[8] M G Bason, M Tanasittikosol, A Sargsyan, A K Mohapatra, D Sarkisyan, R M Potvliege, and C S Adams. Enhanced electric field sensitivity of rf-dressed rydberg dark states. New Journal of Physics, 12(6):065015, jun 2010.

[9] Leonid Belostotski and Sameep Jagtap. Down with noise: An introduction to a low-noise amplifier survey. IEEE Solid-State Circuits Magazine, 12(2):23–29, 2020.

[10] Florian Bergmann, Nicholas R. Jungwirth, Bryan T. Bosworth, Jerome Cheron, Christian J. Long, and Nathan D. Orloff. Measuring the permittivity of fused silica with planar on-wafer structures up to 325 ghz. Applied Physics Letters, 124(7):072902, 02 2024.

[11] Florian Bergmann, Nicholas R. Jungwirth, Bryan T. Bosworth, Jerome Cheron, Christian J. Long, and Nathan D. Orloff. Measuring the permittivity of fused silica with planar on-wafer structures up to 325 GHz. Applied Physics Letters, 124(7):072902, 02 2024.

[12] Samuel Berweger et al. Rydberg-state engineering: Investigations of tuning schemes for continuous frequency sensing. Physical Review Applied, 19(4):044049, 2023.

[13] Stephanie M. Bohaichuk, Donald Booth, Kent Nickerson, Harry Tai, and James P. Shaffer. Origins of rydberg-atom electrometer transient response and its impact on radio-frequency pulse sensing. Phys. Rev. Appl., 18:034030, Sep 2022.

[14] Stephanie M. Bohaichuk, Fabian Ripka, Vijin Venu, Florian Christaller, Chang Liu, Matthias Schmidt, Harald Kübler, and James P. Shaffer. Three-photon rydberg-atom-based radio-frequency sensing scheme with narrow linewidth. Phys. Rev. Appl., 20:L061004, Dec 2023.

[15] K.-J. Boller, A. Imamoğlu, and S. E. Harris. Observation of electromagnetically induced transparency. Phys. Rev. Lett., 66:2593–2596, May 1991.

[16] Sebastian Borówka et al. Continuous wideband microwave-to-optical converter based on room-temperature rydberg atoms. Nature Photonics, 18(1):32–38, October 2023.

[17] Sebastian Borówka, Uliana Pylypenko, Mateusz Mazelanik, and Michał Parniak. Continuous wideband microwave-to-optical converter based on room-temperature rydberg atoms, 2023.

[18] Alan S. Brannon. Design and implementation of microwave VCOs for chip-scale atomic clocks. PhD thesis, 2007.

[19] Roger C. Brown, Baran Kayim, Michael A. Viray, Abigail R. Perry, Brian C. Sawyer, and Robert Wyllie. Very-high- and ultrahigh-frequency electric-field detection using high angular momentum rydberg states. Physical Review A, 107(5), May 2023.

[20] Minghao Cai et al. Sensitivity improvement and determination of rydberg atom-based microwave sensor. Photonics, 9(4), 2022.

[21] Minghao Cai, Zishan Xu, Shuhang You, and Hongping Liu. Sensitivity improvement and determination of rydberg atom-based microwave sensor. Photonics, 9:250, 04 2022.

[22] Minghao Cai, Shuhang You, Shanshan Zhang, Zishan Xu, and Hongping Liu. Sensitivity extension of atom-based amplitude-modulation microwave electrometry via high rydberg states. Applied Physics Letters, 122(16):161103, 04 2023.

[23] Christopher Carr, Monsit Tanasittikosol, Armen Sargsyan, David Sarkisyan, Charles S. Adams, and Kevin J. Weatherill. Three-photon electromagnetically induced transparency using rydberg states. Opt. Lett., 37(18):3858–3860, Sep 2012.

[24] Hong-Yeh Chang, Chi-Hsien Lin, Yu-Cheng Liu, Wen-Ping Li, and Yu-Chi Wang. A 2.5 ghz high efficiency high power low phase noise monolithic microwave power oscillator. IEEE Microwave and Wireless Components Letters, 25(11):730–732, 2015.

[25] Peter S. Chen, Dae-Hyun Kim, Joshua Bergman, Jonathan Hacker, and Berinder Brar. Wideband low-noise-amplifier (lna) with lg = 50 nm ingaas phemt and wideband rf chokes. In 2011 IEEE MTT-S International Microwave Symposium, pages 1–5, 2011.

[26] Ying Chen, Koen Mouthaan, and Fujiang Lin. Design of x-band and ka-band colpitts oscillators using a parasitic cancellation technique. IEEE Transactions on Circuits and Systems I: Regular Papers, 57(8):1817–1828, 2010.

[27] Lan Jen Chu. Physical limitations of omni-directional antennas. Journal of Applied Physics, 19(12):1163–1175, 1948.

[28] Kevin C. Cox, David H. Meyer, Fredrik K. Fatemi, and Paul D. Kunz. Quantum-limited atomic receiver in the electrically small regime. Phys. Rev. Lett., 121:110502, Sep 2018.

[29] Paul Denisowski. White paper: Understanding phase noise measurement techniaues. Technical Report MSU-CSE-06-2, RohdeSchwarz, Munich, Germany, January 2022.

[30] Lucy A. Downes, Andrew R. MacKellar, Daniel J. Whiting, Cyril Bourgenot, Charles S. Adams, and Kevin J. Weatherill. Full-field terahertz imaging at kilohertz frame rates using atomic vapor. Phys. Rev. X, 10:011027, Feb 2020.

[31] Peter K. Elgee, Joshua C. Hill, Kermit-James E. LeBlanc, Gabriel D. Ko, Paul D. Kunz, David H. Meyer, and Kevin C. Cox. Satellite radio detection via dual-microwave rydberg spectroscopy. Applied Physics Letters, 123(8):084001, 08 2023.

[32] H. Q. Fan, S. Kumar, R. Daschner, H. Kübler, and J. P. Shaffer. Subwavelength microwave electric-field imaging using rydberg atoms inside atomic vapor cells. Optics Letters, 39(10):3030, May 2014.

[33] Haoquan Fan, Santosh Kumar, Jonathon Sedlacek, Harald Kübler, Shaya Karimkashi, and James P Shaffer. Atom based rf electric field sensing. Journal of Physics B: Atomic, Molecular and Optical Physics, 48(20):202001, sep 2015.

[34] Charles Fancher, David Scherer, Marc John, and Bonnie Schmittbergermarlow. Rydberg atom electric field sensors for communications and sensing. IEEE Transactions on Quantum Engineering, PP:1–1, 03 2021.

[35] H. Figger, G. Leuchs, R. Straubinger, and H. Walther. A photon detector for submillimetre wavelengths using rydberg atoms. Optics Communications, 33(1):37–41, 1980.

[36] Ran Finkelstein, Samir Bali, Ofer Firstenberg, and Irina Novikova. A practical guide to electromagnetically induced transparency in atomic vapor. New Journal of Physics, 25(3):035001, mar 2023.

[37] Corrado Florian, Sara D'Angelo, Davide Resca, and Francesco Scappaviva. A chip set of low phase noise mmic vcos at c, x and ku band in ingap-gaas hbt technology for satellite telecommunications. In 2017 IEEE MTT-S International Microwave Symposium (IMS), pages 1148–1151, 2017.

[38] Avital Giat, Kfir Levi, Ori Nefesh, and Liron Stern. Subwavelength micromachined vapor-cell based rydberg sensing. arXiv preprint arXiv:2504.09559, 2025.

[39] Joshua A. Gordon, Matthew T. Simons, Abdulaziz H. Haddab, and Christopher L. Holloway. Weak electric-field detection with sub-1 Hz resolution at radio frequencies using a Rydberg atom-based mixer. AIP Advances, 9(4):045030, 04 2019.

[40] Daniel Hammerland, Rajavardhan Talashila, Dixith Manchaiah, Nikunjkumar Prajapati, Noah Schlossberger, Erik McKee, Michael A. Highman, Matthew T. Simons, Samuel Berweger, Alexandra B. Artusio-Glimpse, and Christopher L. Holloway. Mhz to sub-khz field detection with an all-dielectric potassium rydberg-atom sensor. arXiv preprint arXiv:2603.06935, 2026.

[41] Roger F. Harrington. Effect of antenna size on gain, bandwidth, and efficiency. Journal of Research of the National Bureau of Standards, Section D: Radio Propagation, 64D(1):1–12, 1960.

[42] Benjamin Hatanpää and Austin J. Minnich. Hot electron diffusion, microwave noise, and piezoresistivity in si from first principles, 2023.

[43] Christopher Holloway, Mathew Simons, Abdulaziz H. Haddab, Joshua A Gordon, David A Anderson, Georg Raithel, and Steven Voran. A multiple-band rydberg atom-based receiver: Am/fm stereo reception. IEEE Antennas and Propagation Magazine, 63(3):63–76, 2021.

[44] Christopher L. Holloway, Joshua A. Gordon, Andrew Schwarzkopf, David A. Anderson, Stephanie A. Miller, Nithiwadee Thaicharoen, and Georg Raithel. Sub-wavelength imaging and field mapping via electromagnetically induced transparency and autler-townes splitting in rydberg atoms. Applied Physics Letters, 104(24), June 2014.

[45] Christopher L. Holloway, Nikunjkumar Prajapati, Alexandra B. Artusio-Glimpse, Samuel Berweger, Matthew T. Simons, Yoshiaki Kasahara, Andrea Alù , and Richard W. Ziolkowski. Rydberg atom-based field sensing enhancement using a split-ring resonator. Applied Physics Letters, 120(20):204001, May 2022.

[46] Christopher L. Holloway, Nikunjkumar Prajapati, Alexandra B. Artusio-Glimpse, Samuel Berweger, Matthew T. Simons, Yoshiaki Kasahara, Andrea Alù , and Richard W. Ziolkowski. Rydberg atom-based field sensing enhancement using a split-ring resonator. Applied Physics Letters, 120(20):204001, May 2022.

[47] Christopher L. Holloway, Nikunjkumar Prajapati, John Kitching, Jeffery A. Sherman, Carson Teale, Alain Rufenacht, Alexandra B. Artusio-Glimpse, Matthew T. Simons, Amy K. Robinson, and Eric B. Norrgard. Electromagnetically induced transparency based rydberg-atom sensor for quantum voltage measurements, 2021.

[48] Christopher L. Holloway, Matthew T. Simons, Abdulaziz H. Haddab, Carl J. Williams, and Maxwell W. Holloway. A "real-time" guitar recording using rydberg atoms and electromagnetically induced transparency: Quantum physics meets music. AIP Advances, 9(6), 2019.

[49] Christopher L. Holloway, Matthew T. Simons, Marcus D. Kautz, Abdulaziz H. Haddab, Joshua A. Gordon, and Thomas P. Crowley. A quantum-based power standard: Using rydberg atoms for a si-traceable radio-frequency power measurement technique in rectangular waveguides. Applied Physics Letters, 113(9):094101, 08 2018.

[50] J. F. Holmes and B. J. Rask. Optimum optical local-oscillator power levels for coherent detection with photodiodes., 1995.

[51] Jinlian Hu, Yuechun Jiao, Yunhui He, Hao Zhang, Linjie Zhang, Jianming Zhao, and Suotang Jia. Improvement of response bandwidth and sensitivity of rydberg receiver using multi-channel excitations. 2023. Preprint.

[52] Jinlian Hu, Huaqiang Li, Rong Song, Jingxu Bai, Yuechun Jiao, Jianming Zhao, and Suotang Jia. Continuously tunable radio frequency electrometry with rydberg atoms. Applied Physics Letters, 121(1), July 2022.

[53] Yuan-Yu Jau and Tony Carter. Vapor-cell-based atomic electrometry for detection frequencies below 1 khz. Phys. Rev. Appl., 13:054034, May 2020.

[54] Mingyong Jing, Ying Hu, Jie ma, Hao Zhang, Linjie Zhang, Liantuan Xiao, and Suotang Jia. Atomic superheterodyne receiver based on microwave-dressed rydberg spectroscopy. Nature Physics, 16:1–5, 09 2020.

[55] Marko Joler, Kresimir Grgić, and Zvonimir Šipuš. A subtlety of sizing the inset gap width of a microstrip antenna when built on an ultra-thin substrate in the s-band. Sensors, 22(24):9791, 2022.

[56] Samuel H. Knarr, Victor G. Bucklew, Jerrod Langston, Kevin C. Cox, Joshua C. Hill, David H. Meyer, and James A. Drakes. Spatiotemporal multiplexed rydberg receiver, 2023.

[57] A. Kramida, Yu. Ralchenko, J. Reader, and NIST ASD Team. NIST atomic spectra database (asd) (ver. 5.12). Online Database, 2024. Available: `https://physics.nist.gov/asd` [Accessed: 2026-03-02].

[58] Santosh Kumar, Haoquan Fan, Harald Kübler, Jiteng Sheng, and James P. Shaffer. Atom-based sensing of weak radio frequency electric fields using homodyne readout, 2016.

[59] Santosh Kumar, Haoquan Fan, Harald Kübler, Jiteng Sheng, and James P. Shaffer. Atom-based sensing of weak radio frequency electric fields using homodyne readout. Scientific Reports, 7:42981, 2017.

[60] Suleymanzade A. Stone M. et al. Kumar, A. Quantum-enabled millimetre wave to optical transduction using neutral atoms. Nature, 2023.

[61] Santosh Kumar (Gangwar), Haoquan Fan, Harald Kübler, Jiteng Sheng, and James Shaffer. Atom-based sensing of weak radio frequency electric fields using homodyne readout. Scientific Reports, 7, 10 2016.

[62] Jooeun Lee and Zoya Popović. A gaas mmic correlation-dicke radiometer with compact antenna for internal body thermometry. IEEE Journal of Electromagnetics, RF and Microwaves in Medicine and Biology, 9(2):103–109, 2025.

[63] Remy Legaie, Georg Raithel, and David Anderson. A millimeter-wave atomic receiver, 06 2023.

[64] Huaqiang Li, Jinlian Hu, Jingxu Bai, Meng Shi, Yuechun Jiao, Jianming Zhao, and Suotang Jia. Rydberg atom-based am receiver with a weak continuous frequency carrier. Opt. Express, 30(8):13522–13529, Apr 2022.

[65] W. Li, I. Mourachko, M. W. Noel, and T. F. Gallagher. Millimeter-wave spectroscopy of cold rb rydberg atoms. Physical Review A, 67(5):052502, 2003.

[66] Yuxiao Li, Yi Lin, Zhenke Ding, Kai Yang, Ruibing Ran, Zhiqian Wan, and Yunqi Fu. A compact tunable enhancement resonator for rydberg atomic receiver. IEEE Antennas and Wireless Propagation Letters, PP:1–5, 01 2024.

[67] Anhui Liang, Jiawen Sun, and Weifeng Zhu. Design of a 0.2 40 ghz ultra-wideband multi-channel receiver. In 2023 International Conference on Microwave and Millimeter Wave Technology (ICMMT), pages 1–3, 2023.

[68] Chi-Hsien Lin, Wen-Ping Li, and Hong-Yeh Chang. A fully integrated 2.4-ghz 0.5-w high efficiency class-e voltage controlled oscillator in 0.15-μm phemt process. In Asia-Pacific Microwave Conference 2011, pages 864–867, 2011.

[69] V. Manan and S.I. Long. A low power and low noise p-hemt ku band vco. IEEE Microwave and Wireless Components Letters, 16(3):131–133, 2006.

[70] Dixith Manchaiah, Stone Oliver, Samuel Berweger, Christopher L. Holloway, and Nikunjkumar Prajapati. Probing bandwidth and sensitivity in rydberg atom sensing via optical homodyne and rf heterodyne detection. Phys. Rev. A, 113:013729, Jan 2026.

[71] Mateusz Mazelanik, Sebastian Borówka, and Michal Parniak. Lo-free microwave receiver based on rydberg atoms and nonlinear interferometry. page JW2A.121, 01 2024.

[72] David H Meyer, Zachary A Castillo, Kevin C Cox, and Paul D Kunz. Assessment of rydberg atoms for wideband electric field sensing. Journal of Physics B: Atomic, Molecular and Optical Physics, 53(3):034001, jan 2020.

[73] David H Meyer, Zachary A Castillo, Kevin C Cox, and Paul D Kunz. Assessment of rydberg atoms for wideband electric field sensing. Journal of Physics B: Atomic, Molecular and Optical Physics, 53(3):034001, jan 2020.

[74] David H. Meyer, Paul D. Kunz, and Kevin C. Cox. Waveguide-coupled rydberg spectrum analyzer from 0 to 20 ghz. Phys. Rev. Appl., 15:014053, Jan 2021.

[75] David H. Meyer, Paul D. Kunz, and Kevin C. Cox. Waveguide-coupled rydberg spectrum analyzer from 0 to 20 ghz. Phys. Rev. Appl., 15:014053, Jan 2021.

[76] N. Nomura, Y. Aoyagi, Tsung lin Chou, and Y. Sekine. Colpitts-type oscillator for high frequency application. In Proceedings of the 2004 IEEE International Frequency Control Symposium and Exposition, 2004., pages 748–751, 2004.

[77] A. Osterwalder and F. Merkt. Using high rydberg states as electric field sensors. Phys. Rev. Lett., 82:1831–1834, Mar 1999.

[78] M. S. O'Sullivan and B. P. Stoicheff. Scalar polarizabilities and avoided crossings of high rydberg states in rb. Phys. Rev. A, 31:2718–2720, Apr 1985.

[79] Nina B. Popovic, Aaron M. Hagerstrom, Jasper A. Drisko, James C. Booth, Edward J. Garboczi, Christian J. Long, and Nathan D. Orloff. Materials characterization with multiple offset reflects at frequencies to 110 ghz. IEEE Transactions on Microwave Theory and Techniques, 68(1):184–195, 2020.

[80] Marian W. Pospieszalski. Extremely low-noise cryogenic amplifiers for radio astronomy: Past, present and future. In 2018 22nd International Microwave and Radar Conference (MIKON), pages 1–6. IEEE, 2018.

[81] David M Pozar. Microwave engineering. Wiley, Hoboken, NJ, 2005.

[82] Nikunjkumar Prajapati, Jakob W. Kunzler, Alexandra B. Artusio-Glimpse, Andrew P. Rotunno, Samuel Berweger, Matthew T. Simons, Christopher L. Holloway, Chad M. Gardner, Michael S. Mcbeth, and Robert A. Younts. High angular momentum coupling for enhanced rydberg-atom sensing in the very-high frequency band. Journal of Applied Physics, 135(7):074402, 02 2024.

[83] Nikunjkumar Prajapati, David A. Long, Alexandra B. Artusio-Glimpse, Sean M. Bresler, and Christopher L. Holloway. Multichannel, ultra-wideband rydberg electrometry with an optical frequency comb. Nature Communications, 16:11054, 2025.

[84] Nikunjkumar Prajapati, Amy K. Robinson, Samuel Berweger, Matthew T. Simons, Alexandra B. Artusio-Glimpse, and Christopher L. Holloway. Enhancement of electromagnetically induced transparency based rydberg-atom electrometry through population repumping. Applied Physics Letters, 119(21), nov 2021.

[85] A. E. Rodríguez-Soto et al. Monopole antenna array design for 3 t and 7 t magnetic resonance imaging. Magnetic Resonance in Medicine, 2019.

[86] Andrew P. Rotunno, Christopher L. Holloway, Nikunjkumar Prajapati, Samuel Berweger, Alexandra B. Artusio-Glimpse, Roger Brown, Matthew Simons, Amy K. Robinson, Baran N. Kayim, Michael A. Viray, Jasmine F. Jones, Brian C. Sawyer, Robert Wyllie, Thad Walker, Richard W. Ziolkowski, Steven R. Jefferts, Steven Geibel, Jonathan Wheeler, and Eric Imhof. Investigating electromagnetically induced transparency spectral lineshape distortion due to non-uniform fields in Rydberg-atom electrometry. Journal of Applied Physics, 134(8):084401, 08 2023.

[87] I. Rubinstein, R. L. Sleven, and A. Hinte. Narrow bandwidth elliptic-function filters. In 1969 IEEE GMTT International Microwave Symposium, pages 65–71. IEEE, 1969.

[88] I. I. Ryabtsev, I. I. Beterov, D. B. Tretyakov, V. M. Entin, and E. A. Yakshina. Doppler- and recoil-free laser excitation of Rydberg states via three-photon transitions. Phys. Rev. A, 84:053409, 2011.

[89] M. Saffman, T. G. Walker, and K. Mølmer. Quantum information with rydberg atoms. Rev. Mod. Phys., 82:2313–2363, Aug 2010.

[90] Georgia Sandidge, Gabriel Santamaria Botello, and Zoya Popovic. Improving sensitivity of rydberg-atom electrometers through resonant structures. In 2022 IEEE International Symposium on Antennas and Propagation and USNC-URSI Radio Science Meeting (AP-S/URSI), Denver, Colorado, USA, July 2022. Presented July 11, 2022, paper MO-UA.1P.2.

[91] Georgia Sandidge and Zoya Popovic. Microwave characterization of a v-band rydberg-atom electrometer. In Proceedings of the IEEE Wireless and Microwave Technology Conference (WAMICON), Clearwater, Florida, April 2026. IEEE.

[92] Georgia Sandidge, Gabriel Santamaria-Botello, Eric Bottomley, Haoquan Fan, and Zoya Popović. Resonant structures for sensitivity enhancement of rydberg-atom microwave receivers. IEEE Transactions on Microwave Theory and Techniques, 72(4):2057–2066, 2024.

[93] Georgia Sandidge, Gabriel Santamaria-Botello, and Zoya. Popovic. Field enhancement for sensitivity improvement of a room-temperature rydberg-atom receiver. June 2023.

[94] Gabriel Santamaria-Botello, Shane Verploegh, Eric Bottomley, and Zoya Popovic. Comparison of noise temperature of rydberg-atom and electronic microwave receivers, 2022.

[95] J. A. Sedlacek, A. Schwettmann, H. Kübler, and J. P. Shaffer. Atom-based vector microwave electrometry using rubidium rydberg atoms in a vapor cell. Phys. Rev. Lett., 111:063001, Aug 2013.

[96] Jonathon A. Sedlacek, Arne Schwettmann, Harald Kübler, Robert Löw, Tilman Pfau, and James P. Shaffer. Microwave electrometry with rydberg atoms in a vapour cell using bright atomic resonances. Nature Physics, 8(11):819–824, 2012.

[97] Toshihiro Shimura, Hiroshi Matsumura, Yoichi Kawano, Masaru Sato, Toshihide Suzuki, and Yoji Ohashi. Multi-channel low-noise receiver and transmitter for 76-81 ghz automotive radar systems in 65 nm cmos. In 2014 44th European Microwave Conference, pages 596–599, 2014.

[98] Dangka Shylla, Nikunjkumar Prajapati, Andrew P. Rotunno, Noah Schlossberger, Dixith Manchaiah, William J. Watterson, Alexandra Artusio-Glimpse, Samuel Berweger, Matthew T. Simons, and Christopher L. Holloway. Observation of asymmetric sideband generation in strongly driven rydberg atoms. Phys. Rev. A, 111:033115, Mar 2025.

[99] Daniel Sievenpiper, David Dawson, Minu Jacob, Tumay Kanar, Sanghoon Kim, Jiang Long, and Ryan Quarfoth. Experimental validation of performance limits and design guidelines for small antennas. Antennas and Propagation, IEEE Transactions on, 60:8 – 19, 02 2012.

[100] Matthew T. Simons, Alexandra B. Artusio-Glimpse, Amy K. Robinson, Nikunjkumar Prajapati, and Christopher L. Holloway. Rydberg atom-based sensors for radio-frequency electric field metrology, sensing, and communications. Measurement: Sensors, 18:100273, 2021.

[101] Matthew T. Simons, Marcus D. Kautz, Joshua A. Gordon, and Christopher L. Holloway. Uncertainties in rydberg atom-based rf e-field measurements. In 2018 International Symposium on Electromagnetic Compatibility (EMC EUROPE), pages 376–380, 2018.

[102] Benjamin D. Smith, Bahar Babaei, Andal Narayanan, and Lindsay J. LeBlanc. Microwave-to-optical conversion in a room-temperature 87rb vapor for frequency-division multiplexing control. Communications Physics, 6(1):338, 2023.

[103] Danni Song, Yuechun Jiao, Jinlian Hu, Yuwen Yin, Zhenhua Li, Yunhui He, Jingxu Bai, Jianming Zhao, and Suotang Jia. Continuous broadband rydberg receiver using ac stark shifts and floquet states. Applied Physics Letters, 125(19), November 2024.

[104] Zhenfei Song, Hongping Liu, Xiaochi Liu, Wanfeng Zhang, Haiyang Zou, Jie Zhang, and Jifeng Qu. Rydberg-atom-based digital communication using a continuously tunable radio-frequency carrier. Optics Express, 27(6):8848–8857, 2019.

[105] Daniel Steck. Rubidium 87 d line data. 01 2003.

[106] Daniel Steck. Rubidium 85 d line data. 2008.

[107] Stephen Sussman-Fort and Ronald Rudish. Non-foster impedance matching of electrically-small antennas. Antennas and Propagation, IEEE Transactions on, 57:2230 – 2241, 09 2009.

[108] A. Tretiakov, C. A. Potts, T. S. Lee, M. J. Thiessen, J. P. Davis, and L. J. LeBlanc. Atomic microwave-to-optical signal transduction via magnetic-field coupling in a resonant microwave cavity. Applied Physics Letters, 116(16):164101, 04 2020.

[109] Sander Weinreb and Jun Shi. Low noise amplifier with 7-k noise at 1.4 ghz and 25 °c. IEEE Transactions on Microwave Theory and Techniques, 69(4):2345–2351, 2021.

[110] H. A. Wheeler. Fundamental limitations of small antennas. Proceedings of the I.R.E., 35(12):1479–1484, 1947.

[111] R. M. Whitley and C. R. Stroud. Double optical resonance. Phys. Rev. A, 14:1498–1513, Oct 1976.

[112] Bo Wu, Dunwei Liao, Di Sang, Yi Liu, and Yunqi Fu. Enhancing sensitivity of atomic microwave receiver via a fabry–perot cavity. IEEE Transactions on Antennas and Propagation, PP:1–1, 01 2024.

[113] Xinlin Xia, Xu Cheng, Fengjun Chen, Xianhu Luo, and Xianjin Deng. An improved colpitts vco with low phase noise using a gaas bihemt process. IEEE Microwave and Wireless Components Letters, 30(1):70–73, 2020.

[114] Arthur Yaghjian and Steven Best. Impedance, bandwidth, and q of antennas. Antennas and Propagation, IEEE Transactions on, 53:1298 – 1324, 05 2005.

[115] Bowen Yang, Yuhan Yan, Xuejie Li, Ling Xiao, Xiaolin Li, L.Q. Chen, Jianliao Deng, and Huadong Cheng. Highly sensitive microwave electrometry with enhanced instantaneous bandwidth. Phys. Rev. Appl., 21:L031003, Mar 2024.

[116] Jianping Zhou et al. Broadband printed dipole antenna with integrated balun and tuning element for digital tv applications. International Journal of Antennas and Propagation, 2022. Fabricated broadband printed dipole antenna operating approximately 457–872 MHz with measured results and prototype photographs.

[117] Myron L. Zimmerman, Michael G. Littman, Michael M. Kash, and Daniel Kleppner. Stark structure of the rydberg states of alkali-metal atoms. Phys. Rev. A, 20:2251–2275, Dec 1979.

[118] N. Šibalić, J.D. Pritchard, C.S. Adams, and K.J. Weatherill. Arc: An open-source library for calculating properties of alkali rydberg atoms. Computer Physics Communications, 220:319–331, 2017.

Appendix A

Appendix A

A.0.1 A Study on Vapor Cell Heating

One resonator design has been omitted from the main text because it was ultimately unable to be used for measurement. This is due to insufficient performance from the vapor cell, which was manufactured outside the university. Nevertheless, the resonator's RF characterization is a useful study in the impact of a vapor cell on these types of resonant structures.

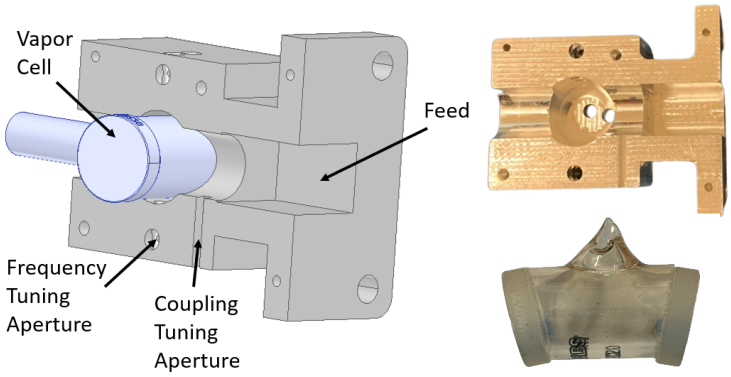


Figure A.1: Geometry of cross-section of the cavity with the vapor cell inserted (left) and photographs of the cavity and glass vapour cell (right).

The resonator targets the $59D_{5/2}$ state at 10.22 GHz, and contains a ThorLabs vapor cell that is 13.36 mm in diameter and 22.65 mm long. The final resonator is $41 \times 41 \times 45$ mm^3 in size and is manufactured as a split-block structure in Aluminum 6061 by CNC machining. The resonant cavity contains the vapor cell, with optical windows so that the lasers can interact with the Rubidium. The cavity is connected to

a WR90 waveguide feed via a coupling aperture, where a copper rod can be inserted through the aperture by a maximum of 9 mm to change the coupling between the cavity and feed. Access to all three coupling regimes (under-, critical, and over-coupling) is necessary to minimize thermal noise contributions from the resonator, where the optimal coupling is determined by the the free-space Rydberg receiver sensitivity [**?**]. A system of copper dowel rods is used on the top and bottom of the resonator to modify the volume of the cavity for frequency tuning.

In simulation, the resonator exhibits a resonance of $|S_{11}| = -23.22$ dB at 10.21 GHz. This corresponds to a loaded quality factor $Q_L = 982$, and under the assumption that the resonator is critically coupled, the unloaded $Q_u = 1964$. The resonator can be frequency tuned from 10.2127 GHz to 10.2638 GHz, for a total range of 50 MHz to account to fabrication detuning. At 10.22 GHz, the resonator has access to all three types of coupling, by inserting the copper rod 9.6 mm for under-, 7.2 mm for critical, and 4.8 mm for overcoupled resonance, corresponding to coupling factors of <1, unity and >1, respectively. The field uniformity is an important aspect of the resonator, as a greater uniformity will improve AT splitting resolution. Overall, the fields in this resonator vary from 20171 to 37543 V/m, as shown in Fig. A.2.

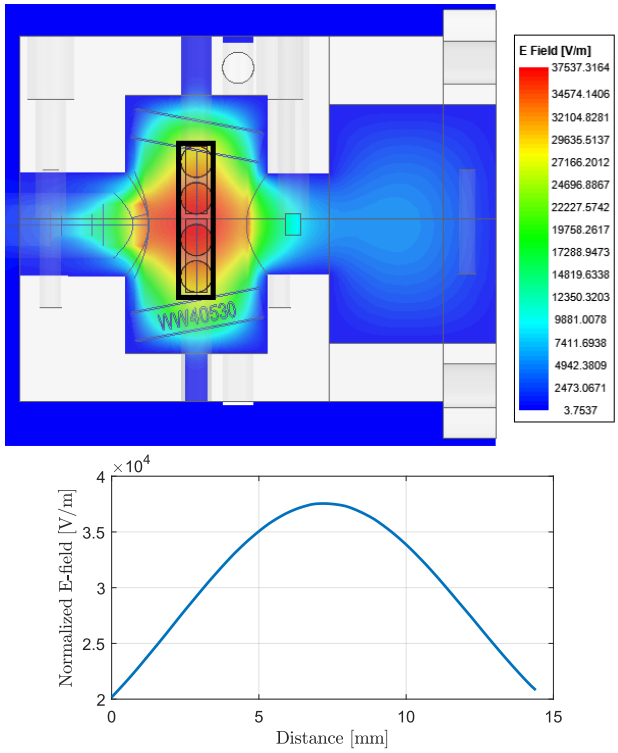


Figure A.2: Simulated co-polarized component of the electric field vector (out of the page) in the cavity (top), including the glass vapor cell filled with vacuum in the simulations. These full-wave simulations are performed with *Ansys HFSS*. The plot shows the normalized electric field vector component along the vapor cell major axis inserted in the cavity.

The RF properties of this cavity resonator are determined by calibrating a vector network analyzer (VNA) and connecting it to the resonator via a WR90 waveguide to SMA coaxial adapter. Initial measurements of the cavity with the vapor cell did not show any resonance, as seen in Fig. A.4. However, baking the cell in the oven at a temperature $>230\,^{\circ}\mathrm{C}$ can mitigate some of the performance degradation within the cell, and an optimal resonance of $-12.89\,\mathrm{dB}$ at $10.022\,\mathrm{GHz}$ was observed after 1.5 hours of baking. This corresponds to an unloaded $Q_u = 20$. The resonator can additionally be frequency tuned from $10.011\,\mathrm{GHz}$ to $10.36\,\mathrm{GHz}$, for a total range of $25\,\mathrm{MHz}$.

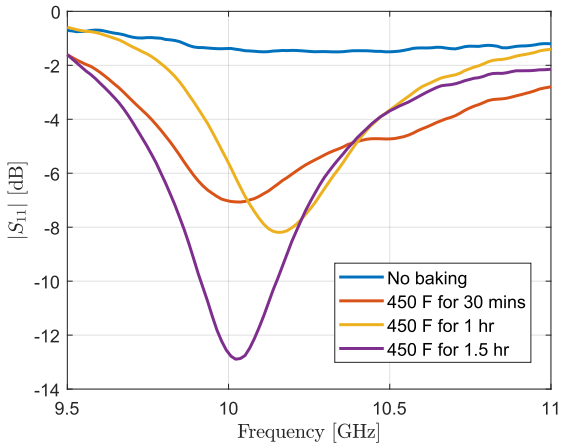


Figure A.3: Measured shift in resonant frequency as a function of baking time starting with a cell where the Rubidium condensed on the cell glass wall.

We found good agreement between the measured and simulated performance of the cavity without the vapor cell, resonating with $S_{11} = -6.60\,\mathrm{dB}$ at 12.41 GHz in simulation and $S_{11} = -11.40\,\mathrm{dB}$ at 12.27 GHz in measurement, for a 1.13% difference in resonant frequency between simulation and measurement. Small variations in the two measurements can likely be attributed to the small gap created in the resonator through the split-block machining process.

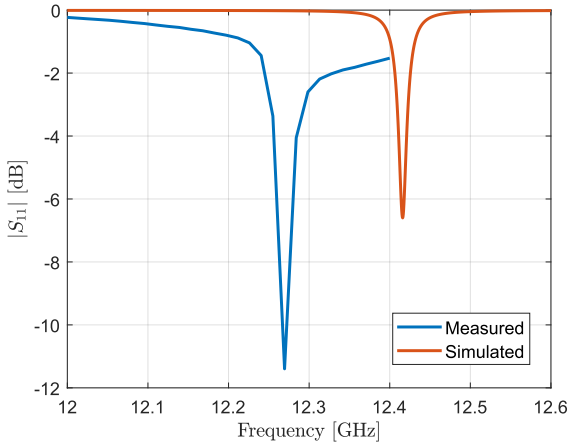


Figure A.4: Measured and simulated cavity resonance without the vapor cell, showing a 1.13% difference between the two.

These measurements show that the Rubidium-filled cell affects the performance of the cavity. The microwave properties of fused silica are well-defined [11], and accounted for in simulations, leading us to the conclusion that the Rubidium vapor is responsible the resonator performance deviation from simulations. Gaseous Rubidium should be lossless in the microwave regime [75], and therefore not impact the vapor cell nor the resonator. However, we found that after manufacturing, Rubidium had condensed to a solid state on the sides of the vapor cell, indicated by a shiny, silver residue. Initially, we heated the vapor cell at around 100°C to evaporate the Rubidium, but found that the Rubidium would quickly condense minutes after the heating was removed. Higher temperatures on the order of 230°C are effective at vaporizing the Rubidium, re-condensing after hours rather than minutes.

ProQuest Number: 32580228

INFORMATION TO ALL USERS
The quality and completeness of this reproduction is dependent on the quality
and completeness of the copy made available to ProQuest.



Distributed by
ProQuest LLC a part of Clarivate (2026).
Copyright of the Dissertation is held by the Author unless otherwise noted.

This work is protected against unauthorized copying under Title 17,
United States Code and other applicable copyright laws.

This work may be used in accordance with the terms of the Creative Commons license
or other rights statement, as indicated in the copyright statement or in the metadata
associated with this work. Unless otherwise specified in the copyright statement
or the metadata, all rights are reserved by the copyright holder.

ProQuest LLC
789 East Eisenhower Parkway
Ann Arbor, MI 48108 USA